Design of Nanostructured Ag Catalysts for Selective Heterogeneous Catalytic and Photocatalytic Oxidation Reactions

by

Phillip Neil Christopher

A dissertation submitted in partial fulfillment
of the requirements for the degree of
Doctor of Philosophy
(Chemical Engineering)
in The University of Michigan

Doctoral Committee:

Associate Professor Suljo Linic, Chair
Professor Phillip E. Savage
Professor Johannes W. Schwank
Assistant Professor Anton Van Der Ven

This dissertation is dedicated to my Parents, ALL of them.

Acknowledgments

First and foremost I would like to acknowledge Professor Suljo Linic for his help and guidance throughout my PhD. He continuously pushed the quality of my research, presentation and writing skills towards excellence. He was a great mentor and will continue to be a friend for many years. I would also like to thank my other committee members, Phil Savage, Johannes Schwank and Anton Van Der Ven for their help and guidance throughout my PhD.

Thanks to the entire Linic research group for their help and companionship throughout the last five years. Particularly, thanks to Neil Schweitzer, Hongiang Xin and David Ingram for collaborations. In addition, Marimuthu Andiappan, Preeta Maitra, Paul Hernley and Zhongnan Xu for the help with the syntheses of thousands of batches of nanocubes. Also to Adam Holewinksi for making long hours spent in the lab unique experiences.

Thanks to Tom Westrich for the many brainstorming sessions. Also, thanks to Ashish Agarwal for working on the initial attempts to synthesize Ag nanowires. Thanks to Andy Tadd for being an excellent engineer and his willingness to think through any situation.

Thanks to the Chemical Engineering department staff for all their assistance. Specifically, thanks to Claire, Shelly, Ruby, Sandy, Rhonda, Linda and of course Harald.

Now on a personal level, thanks to my parents for always being there for me. Each one of them has unique qualities that I have learned from and I am a better and stronger person because of how I was raised. Thanks to my little sister Alex for being awesome and for always being there when I needed to talk.

Thanks to Jaime Payne for just being incredible in every way I can think of. I absolutely would not have made it through my PhD without Jaime. I have and will continue to look to her for inspiration.

Thanks to Ramsey for being Ramsey.

Thanks to all my friends in the department, around Ann Arbor and throughout my entire life. The list is much to long to write out. You know who you are, thank you for everything.

Table of Contents

List of Figures

Abstract

In this dissertation we have utilized a multi-faceted approach, combining quantum chemical calculations, well-controlled synthesis techniques and an arsenal of characterization techniques to design catalysts for important catalytic and photocatalytic oxidation reactions. Specific focus was placed on exploiting unique shape and size dependent properties of Ag nanoparticles to design new catalytic materials and entirely new reacting systems (coupling thermal and photonic stimuli) for the industrially relevant ethylene epoxidation reaction. We demonstrated novel routes for enhancing the selectivity and activity of Ag based epoxidation catalysts.

The work presented in this dissertation provides two unique platforms for controlling and engineering the catalytic function of metallic nanoparticles. In the first example we utilize a combination of density functional theory calculations and shape and size controlled synthesis approaches to design highly selective (up to 85%) Ag catalysts for ethylene epoxidation. Our studies show that catalytic particles of controlled size and shape represent promising heterogeneous catalysts for selective production of chemicals and also act as a critical platform to study heterogeneous catalytic process and identify crucial factors that impact process selectivity.

In the second example, it was demonstrated that plasmonic Ag nanostructures could couple thermal and solar energy to efficiently drive selective oxidation reactions at up to 100 K lower temperature than a pure thermal process. The results are important for

a number of reasons: (i) This is the first observation of metallic nanoparticles performing steady-state photocatalytic reactions in the single and multi-excitation regimes under low intensity, continuous wave visible photon illumination, (ii) Plasmonic nanoparticles are unique in combing excellent thermocatalytic capabilities and strong interaction with UV and visible photons to effectively couple multiple energy stimuli to drive catalytic reactions and, (iii) The results suggest that since the reactions can be operated at lower temperatures, the long-term stability of catalysts and the product selectivity could be potentially enhanced. We provide a first-principles based model, which captures the effect of intensity and temperature on the process efficiency. These discoveries open the door to the design of new classes of (photo)catalytic materials, for energy efficient production of important chemicals and fuels.

Chapter 1

Introduction

1.1 Summary

This chapter provides an introduction to the field of heterogeneous catalysts and the critical challenges associated with the design of more effective catalytic materials. An approach towards the rational design of novel catalytic materials, using a combined experimental and theoretical method is outlined. We discuss the driving force for the development of new approaches for designing heterogeneous catalytic materials. In addition, we provide a brief background of the landscape changing advances in fields of chemistry and physics that allow the rational design of heterogeneous catalytic materials from atomic scale mechanistic insights. We discuss this approach in the context of utilizing a combination of theoretical chemistry and well-controlled synthesis techniques to produce Ag nanoparticles with geometric properties that are tailored for various catalytic and photo-catalytic processes. The chapter is concluded by outlining the topics discussed throughout the dissertation.

1.2 Importance of Heterogeneous Catalysis

The massive scale release of harmful greenhouse gases from the chemical industry, combined with dwindling fossil fuel resources, has sparked a renewed interest in developing highly efficient and environmentally friendly chemical conversion processes.[1,2] Heterogeneous catalytic reactions are of paramount importance in almost all large-scale chemical conversion, energy production and pollution mitigation processes and thus play a crucial role in the transformation of the chemical industry towards higher level of sustainability. The development of catalysts and processes that reduce thermal energy input requirements, exhibit high activity and approach 100% atom efficiency in conversion of natural resources to desired products is necessary to mitigate environmental and resource concerns.[3] In addition, the emergence of alternative feedstocks (e.g. solar fuels and biomass) will require the design of new catalytic materials that can perform complex chemistries with high efficiency.

Currently all major industrial chemical processes are driven by thermal energy. The effectiveness of a thermal driven catalytic process is dictated by the energy input required to achieve desired rates and the efficiency of converting the feedstock into desired products. Optimization of these two features drives the discovery of new catalytic materials. Efforts to lower thermal energy input requirements and increase selectivity, center around the design of special catalytic sites that more effectively activate chemical reactions.[4,5,6,7,8] This strategy has had limited success since the phase space of viable catalytic sites is restricted by their inherent lack of thermal stability. Also, catalytic sites that can thermally activate reactants at lower temperature almost always interact with adsorbates more strongly and are therefore more easily poisoned by the

adsorbates, and often suffer from reduced selectivity.[9] These limitations, coupled with the lack of molecular insights into catalytic process, has made it difficult to design highly efficient catalytic processes that require very little or no thermal energy input.

The massive thermal energy input required by the chemical industry is provided almost solely by combustion of fossil fuels (coal and natural gas). This issue has triggered an increased focus on developing chemical and energy conversion technologies that utilize solar energy to drive chemical reactions. The difficulty associated with the development of photocatalytic materials for various chemical reactions lies in the ability to create materials that can (a) efficiently absorb solar light, (b) channel this energy into chemical bonds, and (c) perform selective catalytic transformations.[10,11] Discovering versatile photocatalytic materials than can perform all three of the major functions has proven to be very difficult and as a result the number of industrial processes driven by solar energy is limited.

Classically, the development of (photo)catalytic materials (ie. metal, support, dopants and promoters) has been achieved through a trial and error approach, where the large phase space of possible materials, synthesis methods and reaction conditions are probed to optimize catalytic processes. Although this approach has resulted in the development of an economically successful chemical industry, most chemical processes are still characterized by necessity of large thermal inputs to drive reactions and less then 100% atomic efficiency in transforming reactants to products. The necessities for more efficient existing processes and the development of entirely new processes for utilization of emerging resources indicates that new approaches to the design of catalytic materials must be considered.[12,13,14] In this dissertation focus is placed on the rational design of

(photo)catalytic materials, through a combined experimental and theoretical approach, that result in more energy efficient and environmentally friendly chemical conversion processes.[7,8,10,15]

1.3 Fundamentals of Heterogeneous Catalysis

Heterogeneous catalysts facilitate chemical reactions by interacting with reactants, creating modified potential energy landscapes, that allow chemical reactions to occur more facilely than in the gas phase (See Figure 1.1(a)). The specific interaction between a given set of reactants and catalytic material will dictate the degree to which the potential energy is modified. Reactants are driven across the ground state potential energy surface through coupling with metal phonon modes (collective vibration of the

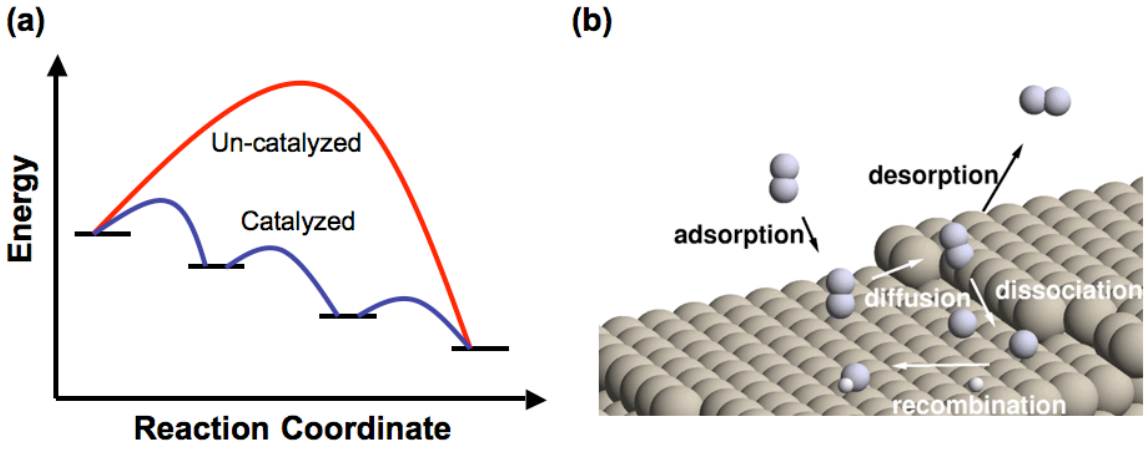

Figure 1.1 Heterogeneous catalytic reactions. (a) The figure shows the catalyzed (on surface) and un-catalyzed (gas phase) potential energy surfaces associated with a model reaction. This shows that the function of a catalyst is to provide an alternate reaction pathway with a significantly reduced activation barrier. (b) The figure shows a schematic of various processes that occur during a surface catalyzed reaction.[16]

metal lattice).[17] When a molecule gains sufficient vibrational energy along the potential energy surface to overcome the activation barrier, the reaction will occur. Increasing the system temperature results in population of higher energy vibrational states along the reaction potential energy surface, thereby increasing the reaction probability.[18] The dependence of reaction probability on temperature is typically exponential and captured by the Arrhenius relationship.

Heterogeneous catalytic reactions typically involve 3 important types of elementary chemical reactions: adsorption of reactants, surface reactions and product desorption. Figure 1.1(b) shows an example of some of the typical elementary chemical processes involved in surface catalyzed reactions, including reactant adsorption, surface diffusion, dissociation of adsorbed species, recombination or association of surface species and desorption.[16] The complex interplay associated with these various elementary chemical steps involved in the catalytic cycle dictate the effectiveness of a particular catalyst for a given reaction. The goal of developing new catalytic materials is the optimization of the interaction between the reactants and catalyst surface to minimize the energy required (E_a) to form the desired products.

A particularly versatile class of heterogeneous catalysts, widely used in the chemical industry, is characterized by small, nanometer scale, metal particles on high surface area, mechanically stable supporting materials.[19] Figure 1.2 shows a schematic of a typical supported metal catalyst, showing that the surface structure of the metal is highly variable, in terms of the geometric arrangements of atoms. Because of the complex nature of typical catalytic metal nanoparticles, there are a plethora of different "active" sites where elementary steps can take place.[20] Each different site is

characterized by different chemical and catalytic activity due to varying geometries and composition of the active site. The complex nature of supported metal catalysts makes it very difficult to understand surface catalyzed reaction mechanisms and where on a catalytic metal particle catalytic reactions take place most efficiently.

The two crucial descriptors of catalytic performance are activity and selectivity. Activity is defined as the rate that a catalytic reaction precedes at an active site. The activity of a catalytic site is controlled by the energetics associated with individual elementary steps that make up the catalytic cycle and the frequency with which the individual steps are attempted. The catalytic activity of an active site for a complete catalytic cycle is often dictated by 1 elementary step, known as the rate-limiting step (RLS). The RLS is defined as the "slowest" step. Figure 1.2 shows potential energy surfaces for a simple surface reaction, taking place on three different active site geometries. The Figure shows how the RLS can be any of the elementary steps leading to product evolution and is dependent on the active site geometry. The identification of the RLS in catalytic reactions has proven to be a difficult endeavor and often times limits our ability to design new catalytic materials based on fundamental insights. The ultimate goal in the design of highly active catalysts is the synthesis of materials that catalyze the conversion of reactants to desired products with very low, or no activation barriers, thereby eliminating the need for thermal energy input to achieve high reaction rates.

Increasing concerns with efficiently utilizing fossil fuel feedstocks has placed significant importance on designing catalytic processes that can achieve close to 100% selectivity towards the desired products.[1,3] Whereas the activity of a catalytic material can often be described by the rate of a single elementary step, RLS, describing the

selectivity of a catalytic reaction requires an understanding of competing pathways.[21] Figure 1.2 shows an example of how different active sites can affect selectivity towards the desired product. Developing insights into the steps that control selectivity for a particular process has proven to be even more challenging than understanding the RLS of a reaction. The key to developing catalysts that exhibit high selectivity is the ability to understand and rationally manipulate competing elementary steps by varying the catalytic active site.

The difficulty associated with designing optimized catalysts, lies not only in the understanding of which steps significantly control reaction rate and selectivity, but also in the ability to predict which active sites are optimal for a particular reaction and the synthesis of catalytic materials with high concentrations of active sites with targeted geometric and compositional structures. Typically, catalytic metal particles are synthesized by dispersing metal containing salts onto a supporting material. Metal particles are then formed by reducing the salt in a high temperature gas phase process, followed by the oxidation of residue compounds left behind during the salt decomposition. The geometric structure of the resulting metallic particles is dictated by the thermodynamics associated with the metallic surface structure, and the interaction between the metal and the supporting material. As a result of this thermodynamic control, metal catalytic particles are semi-spherical shapes terminated in the lowest energy surface facet of the metal (mostly (111) and (1000)) and have diameters ranging from 5-100 nm.[22] Because the synthesis procedures utilize thermodynamics to dictate the geometric and surface structure of the catalytic particles, it has remained very difficult to synthesize tailored catalytic particles with targeted sizes and shapes.

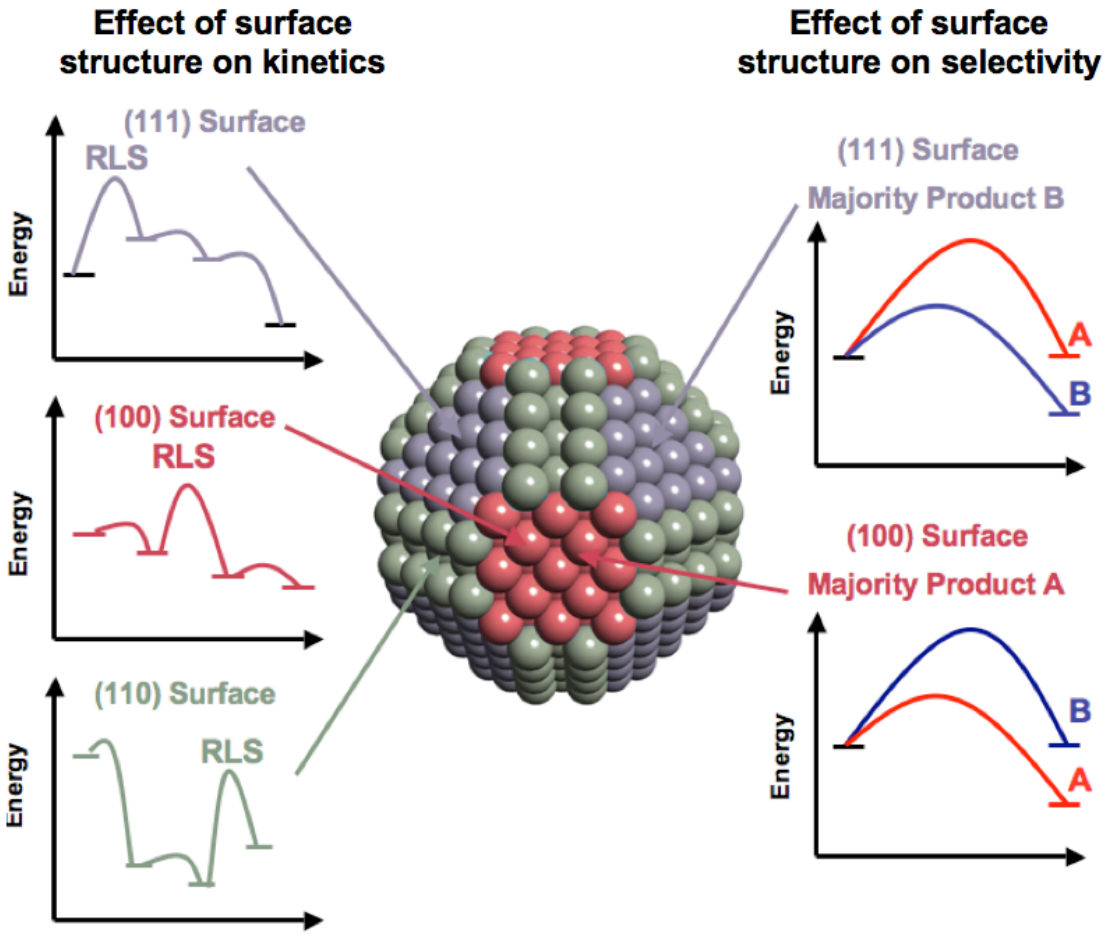

Figure 1.2 The effect of catalyst surface structure on kinetics and selectivity. The figure shows a schematic of a catalytically active metal nanoparticle. The gray atoms represent (110) surface sites, the red atoms represent (100) surface sites and the purple atoms represent (111) surface sites. The potential energy surfaces on the left of the particle show that the surface structure affects the energetics of each elementary step in a model catalytic reaction. The potential energy surfaces on the right side show that the surface structure can also dictate the selectivity of a catalytic reaction, by affecting the activation barriers associated with competing elementary steps.

1.4 Fundamentals of Heterogeneous Photocatalysis

Photocatalytic reactions involve all the typical elementary steps that take place in a thermally driven heteroegenous catalytic process, but in addition, one or more of the crucial elementary steps is driven by an energetic electron or hole. In these processes, an incoming flux of photons is absorbed by the photocatalytic material, and produces energetic charge carriers (electron/hole pairs). The energetic charge carriers must then migrate to the surface of the photocatalyst, where they can interact with adsorbed reactant molecules. The interaction of the energetic charge carriers with adsorbates, effectively deposits the energy of the photon flux into chemical bonds. The design of efficient photocatalytic materials for various chemical reactions has proven very difficult. An optimal photocatalytic material must contain all the characteristics of an optimal catalytic material that drives reactions with thermal energy, and must efficiently channel the energy of photons into chemical bonds.[10,15] Although there has been incremental increases in the efficiency of photocatalytic process for a few select reactions (H_2O splitting and organic molecule decomposition) the phase space of reactions that can be photocatalyzed is extremely limited. These limitations once again point to the importance of developing a "rational" approach, based on molecular insights, for the design of novel photocatalytic materials.

1.5 New Directions: Rational Design of Targeted Materials

When thinking about the optimal approach towards designing (photo)catalytic materials, we have identified four crucial components: (1) Identification of the elementary steps that control performance, (2) Access to predictive theories of adsorbate-

surface interactions to identify optimized catalytic materials, (3) Synthetic strategies for catalytic particles with targeted properties (4) Preservation of the active site under reactions conditions. Landscape changing advances in areas of physical chemistry, nanomaterials synthesis, computational chemistry and analytical characterization of catalytic materials have opened the door towards the rational design of highly tailored catalytic materials by enabling us to approach each of the above mentioned components. In this section the major advancements, allowing the rational design of tailored nanomaterials, are briefly discussed.

1.5.1 Surface Science

The development of surface science techniques in the 1970's and 1980's ushered in a new era of mechanistic understanding of surface catalyzed reactions.[23] In typical surface science experiments single crystal "model" catalytic materials are used, that display homogeneous distributions of active sites and allow for the mechanistic studies of single elementary steps on well-defined and characterized metal surfaces. In addition, experiments are typically performed under very well defined atmospheric conditions at very low pressures ($<10^{-8}$ torr), where only desired reactants are introduced into the reaction vessel allowing control over which elementary steps are probed. Countless experimental techniques were developed during this time allowing accurate measurements of geometric structure, electronic structure and vibrational fingerprints of both the catalyst surface as well as adsorbed molecules.[24,25] These "model" catalysts allowed researchers to build a fundamental understanding of how the geometry and

composition of an active site can affect its catalytic activity for a particular elementary step.

In this dissertation, insights gained from previous surface science experiments will be utilized to guide the design of new catalytic materials. The first example focuses on a series of surface science experiments, coupled with quantum chemical calculations that were used to identify the underlying mechanism controlling selectivity in the ethylene epoxidation reaction.[26,27] These studies highlight an example where mechanistic insights into fundamental molecular mechanisms of an important industrial process were obtained from surface science experiments. The general framework developed in these studies is used in this dissertation to predict and understand how systematic modification of catalytic properties affect ethylene epoxidation selectivity.[7,8] The second example is the use of femtosecond laser excitation of adsorbates on metal surfaces to understand the underlying physics associated with photocatalysis on metal surfaces. Ultra-fast lasers and detection systems are now commonly employed to study the dynamics of interactions of excited electrons at metal surfaces with adsorbed molecules.[28,29,] In this dissertation, insights into the underlying physics of metal photochemistry gained through these surface science studies are used to explain and corroborate an exciting new finding that metallic nanostructures can act as excellent photocatalytic materials for the production of useful commodity chemicals.[15]

1.5.2 Computational Chemistry

The advent of density functional theory and efficient parallel computing resources has allowed for accurate and rapid calculation of material properties and chemical

interactions using a first-principles approach. Density functional theory (DFT) involves the parameterization of the many-body problem associated with interacting electrons in a collection of atoms, in a 3 dimensional system, where an electron density is used to defined the position and energy of electrons.[30] By utilizing this theory it is possible to calculate the energy of large collections (up to a few hundred) of atoms and extend these insights into periodic systems that are excellent representations of catalytic surfaces.

DFT calculations have been shown to be particularly accurate for calculating the energetics associated with interactions of adsorbed molecules on metal surfaces.[31,32] DFT calculations can be utilized to predict the adsorption energies of molecules on surfaces, the stability of various surface structures and the activation barriers associated with elementary catalytic steps. By combining these different types of calculations, it is now possible to map out complete catalytic reactions and predict which steps may control the overall rate.[20,33] Even more importantly, these calculations allow the comparison of different surface structures and compositions for a given reaction, thereby providing a predictive tool for the design of novel catalytic materials.[7,12,13,34] One recent example is the use of DFT calculations to identify cheap, efficient catalytic materials for the selective hydrogenation of acetylene in an ethylene feed stream.[34] This is an important process for the production of high quality poly-ethylene based plastics, where the contamination of an ethylene stream with traces of acetylene is extremely detrimental to the process. This process classically utilized expensive Pd/Ag alloys. In this publication the authors use DFT calculations to identify NiZn alloys as potentially selective catalysts and experimentally verify that this is a significantly cheaper catalytic material that rivals the selectivity and activity of the traditional PdAg alloy catalyst. This is just one of many

recent examples highlighting how DFT calculations have been utilized to drive rational catalyst discovery. In this dissertation DFT is specifically used to predict how selective different surface facets of Ag are for the ethylene epoxidation reaction. The insights gained from these calculations are used to guide the synthesis of targeted catalytic materials.

1.5.3 Novel Synthesis Approaches

As opposed to traditional vapor phase approaches that have typically been used to synthesize catalytic materials, solution phase synthesis of catalytic metallic nanoparticles has emerged as a versatile approach.[35,36] Solution phase methods provide a number of strategies for manipulating the growth of metal nanostructures to achieve desired sizes and shapes that are not available in vapor phase synthesis methods. In solution based synthesis approaches there are four crucial steps that play a role in controlling the nanoparticle size and shape: reduction of the metal salt, nucleation of seeds, etching of seed particles and controlled nanocrystal growth.[37] By controlling each of these steps separately it has become possible to synthesize metallic nanoparticles with desired shapes, sizes and compositions in fairly large scale.

The first successful applications of this approach for the synthesis of metallic nanoparticles were reported by El-Sayed et al. in 1996 and Xia et al in 2002.[35,36] In both of these examples metals salts were added in parallel with a polymeric stabilizing agent to a solvent. The temperature of the solvent and the strength of the reductant controlled the rate of metal salt reaction and nanoparticle growth. By carefully controlling the conditions of nucleation and growth the researchers were able to manipulate the shape of

Pt, Ag and Au nanoparticles. In the context of designing new catalytic materials, the advent of these well-controlled synthesis techniques allows a systematic variation of crucial design parameters (mostly catalyst surface structure) to optimize a catalytic material and develop important mechanistic insights. In this dissertation we use shape and size controlled synthesis of Ag nanoparticles to rationally manipulate catalytic and optical properties for various (photo)catalytic reactions.

1.6 Oxidation Reactions on Ag

A particularly important class of industrial reactions involves the selective oxidation of hydrocarbons over heterogeneous Ag-based catalysts. In terms of scale and market value, the epoxidation of ethylene to form ethylene oxide is by far the most important industrial catalytic process performed on Ag catalysts, Equation 1.

$$C_2H_4 + \frac{1}{2}O_2 \leftrightarrow C_2H_4O \qquad (1)$$

World-wide production of ethylene oxide is valued at over $20 billion per year.[38] The reaction is carried out by passing gas phase ethylene and oxygen over a supported Ag catalyst at temperatures between 500-600 K. In terms of overall process efficiency the major limitations are (a) atomic efficiency in the conversion of ethylene to ethylene oxide, limited by process selectivity typically at 85 %, (b) energy efficiency, limited by the kinetics of the reaction which requires significant thermal input to achieve desired product yields and (c) limited catalyst lifetime as a result of the fairly high operating temperatures required.[39]

The limited selectivity of the ethylene epoxidation reaction over Ag based catalysts is a result of catalytic sites that produce ethylene oxide (desired product) and

complete combustion products (CO_2 + H_2O, undesired products).[40] Although a significant amount of research has analyzed the empirical effects of various promoters on the process selectivity, only very recently have molecular level insights into the effect of these promoters been developed.[21,26] In this dissertation a novel, combined theoretical and experimental, approach is used to develop an understanding of how Ag surface structure affects the process selectivity. These insights are used to rationally design a highly selective catalyst for the ethylene epoxidation reaction.

The high process temperature required to achieve reasonable product yields over Ag catalysts is a result of the slow kinetics associated with the rate limiting elementary step, the dissociation of O_2 on the Ag surface to form atomic oxygen.[33,41] It has proven very difficult to enhance the catalytic selectivity and activity of the same Ag based epoxidation catalysts. Because of this difficulty and the importance placed on enhancing the selectivity of this process, modification of catalytic materials to enhance activity and thus reduce the required operating temperatures, has received relatively little attention. This issue is addressed in this dissertation by introducing a new concept of driving catalytic reactions by coupling solar and thermal energy stimuli.[15] A class of catalytic materials is developed that combine the unique catalytic and optical properties of well-defined Ag nanoparticles. This efficient energy coupling allows a reduction in the thermal requirements for executing ethylene epoxidation, by utilizing the energy of a photon flux to assist in driving the reaction. This approach alleviates a number of the energy efficiency and catalyst lifetime issues associated with ethylene epoxidation and shows for the first time that metallic nanostructures can be highly efficient photocatalytic materials.

1.7 Dissertation Summary

The objective of this dissertation is to utilize molecular insights gained through experimental and theoretical studies to guide the synthesis of well-defined metallic nanostructures with targeted sizes and shapes. We focus on the design of photo(catalytic) materials that take advantage of the unique catalytic and optical properties of Ag nanoparticles. We show that the shape and size of Ag nanoparticles play a significant role in dictating the selectivity in the ethylene epoxidation reaction, and that these variables can be rationally tuned to design a highly selective catalyst. In addition, we demonstrate that nanostructured Ag catalysts are uniquely capable of coupling solar and thermal energy stimuli to drive oxidation reactions at significantly lower temperatures as compared to pure thermal processes.

In Chapter 2 the details of the experimental and theoretical methods used throughout the dissertation are described. Specific focus is placed on the fundamental mechanisms that control the synthesis of size and shape controlled Ag nanoparticles. The characterization instruments and reactor designs used to study (photo)catalytic properties are described, and the underlying principles governing their operation are discussed. In addition, the theoretical tools (Density functional theory and Finite-difference time-domain) used to guide the synthesis of targeted materials are explained in detail.

In Chapter 3 we discuss the shape and size dependent properties that are exploited in this dissertation to optimize (photo)catalytic materials. We show that the shape and size can be used to manipulate the dominant surface facet on Ag nanoparticles. In

addition, the interaction of Ag nanoparticles with UV and visible photons is shown to be highly dependent on the geometric characteristic of the nanostructures.

In Chapter 4 we utilized DFT calculations to examine the effect of Ag surface structure on process selectivity. Based on these calculations, we identified the Ag(100) surface facet as being inherently more selective than the Ag(111) surface facet, which dominates most industrial Ag catalysts synthesized using classical approaches. We utilized synthesis approaches recently developed in the nanotechnology community to synthesize Ag nanowires dominated by the Ag(100) facet. The results of the DFT calculations were supported by reactor studies that showed Ag nanowires, dominated by the (100) surface facet, were significantly more selective for ethylene epoxidation compared to an Ag catalyst dominated by the (111) facet. The results showed that recent advances in synthetic approaches, combined with DFT calculations, might provide a versatile platform for the design of highly selective catalysts.

In chapter 5 we examine the effect of Ag nanoparticle size and shape and external conditions on the selectivity of catalytic ethylene epoxidation. Shape and size controlled synthesis of Ag nanoparticles, through a solution-based approach, is used to show that silver nanocubes exhibit higher selectivity than nanowires and nanospheres. For a given shape we find that larger particles offer improved selectivity. The enhanced selectivity toward ethylene oxide is attributed to the nature of the exposed Ag surface facets; Ag nanocubes and nanowires are dominated by (100) surface facet and Ag nanospheres are dominated by (111). Furthermore we demonstrate that the concentration of undercoordinated surface sites is related to diminished selectivity to ethylene oxide. These mechanistic insights were used to design a highly selective catalyst for the

ethylene epoxidation reaction.

In Chapter 6 we show that composite materials composed of plasmonic Ag nanostructures and TiO_2 photocatalysts show enhanced photo-activity compared to the pure TiO2 in the decomposition of methylene blue. The enhanced photo-chemical activity is attributed to radiative transfer of energy, mediated by surface Plasmons, from Ag particles to the semiconductor leading to higher concentrations of charge carriers (e-/h+ pairs) in the semiconductor and therefore to higher photo-chemical activity. We show that by rationally changing size and shape of Ag nanostructures it is possible to maximize photo-catalytic activity of a semiconductor at a given excitation wavelength.

In Chapter 7 it is shown that Ag nanostructured catalysts can concurrently use low intensity visible light (on the order of solar intensity) and thermal energy to drive catalytic oxidation (ethylene epoxidation, CO oxidation and selective NH_3 oxidation) reactions at lower temperatures than their conventional counterparts that use only thermal stimulus. Based on kinetic isotope experiments and density functional calculations, we postulate that excited plasmons on the Ag surface act to populate O_2 anti-bonding orbitals, forming a transient negative ion state, thereby facilitating the rate-limiting O_2 dissociation reaction. The results open avenues towards the design of more energy efficient and robust catalytic processes.

In Chapter 8 we show that the excitation of surface plasmons on Ag nanostructures by relatively low intensity visible photon illumination (<300 mW/cm^2) results in a highly efficient multi-electron driven photo-catalytic process. This shows the first observation of a regime shift from linear to non-linear dependence of photo-rate on intensity, driven by a low intensity continuous wave source. In addition, the excellent

thermo-catalytic features of metallic nanoparticles allow for an effective coupling of thermal and photonic stimuli to produce a previously unreported exponential dependence of photocatalytic quantum efficiency on operating temperature. We provide a first-principles based model, which captures the effect of intensity and temperature on the process efficiency.

In Chapter 9 we highlight the major conclusions drawn from the work in this dissertation. We discuss the conclusions in the context of the fields of heterogeneous catalysts and photo-catalysts. The continuation and application of this work in new research directions is also discussed.

1.8 References

[1] G.A. Somorjai, R.M. Rioux, *Catal. Today*, **100**, 201, 2005.

[2] A.L. Linsebiger, G. Lu, J.T. Yates, *Chem. Rev.*, **95**, 735, 1995.

[3] H.-J. Freund, *Top. Catal.* **2008**, 48, 137.

[4] N. Tian, Z. Zhou, S. Sun, Y. Ding, Z.L. Wang, *Science,* **316** ,732, 2007.

[5] M. Chen, D. Kumar, C.W. Yi, D.W. Goodman, *Science,* **310**, 291, 2005.

[6] Y. Lei, *et al. Science*, **328**, 224, 2010.

[7] P. Christopher, S. Linic, *J. Am. Chem. Soc.,* **130**, 11264, 2008.

[8] P. Christopher, S. Linic, *ChemCatChem,* **2**, 78, 2010.

[9] T. Bligaard, J.K. Norskov, S. Dahl, J. Matthiesen, C.H. Christensen, J. Sehested, *J. Catal.,* **206**, 224, 2004.

[10] P. Christopher, D. B. Ingram, S. Linic, *J. Phys. Chem. C*, **114**, 9173, 2010.

[11] K. Maeda, *et. al. Angew. Chem.,* **122**, 4190, 2010.

[12] S. Linic, J. Jankowaik, M.A. Barteau, *J. Catal.*, **224**, 489, 2004.

[13] E. Nikolla, A. Holewinski, J. Schwank, S. Linic, *JACS*, **128**, 11354, 2006.

[14] F. Besenbacher, *et. al. Science*, **279**, 1913, 1998.

[15] P. Christopher, H. Xin, S. Linic, *Nature Chem.,* **3**, 467, 2011.

[16] C.H. Christensen, J.K. Norskov, *J. Chem. Phys.*, **128**, 182503, 2008.

[17] M. Bonn, *et al. Science*, **285**, 1042, 1999.

[18] C. Jedrzejek, K.F. Freed, S. Efrima, H. Metiu, *Chem. Phys. Lett.* **79**, 227, 1981.

[19] A.T. Bell, *Science*, **299**, 1688, 2003.

[20] K. Honkala, *et al.*, *Science*, **307**, 555, 2005.

[21] S. Linic, M. A. Barteau, *J. Am. Chem. Soc., **125***, 4034, 2003.

[22] S. Linic, P. Christopher, *ChemCatChem*, **2**, 1061, 2010.

[23] G. Ertl, *Angew. Chem. Int. Ed.,* **47**, 3524, 2008.

[24] D. W. Goodman, *Chem. Rev.*, **95**, 523, 1995.

[25] G. Ertl, H.-J. Freund, *Physics Today*, **January**, 32, 1999.

[26] S. Linic, M. A. Barteau, *J. Am. Chem. Soc.,* **124**, 310, 2002.

[27] S. Linic, M. A. Barteau, *Angew. Chem. Intl. Ed*., *43*, 2918, 2004.

[28] *Laser Spectroscopy and Photochemistry on Metal Surfaces;* Dai, H.-L., Ho, W., Eds.; World Scientific: Singapore, 1995.

[29] W. Ho, *J. Phys. Chem.,* **100**, 13050, 1996.

[30] P. Hohenberg, W. Kohn, *Phys. Rev.*, **136**, B864, 1964.

[31] B. Hammer, J.K. Nørskov, *Nature*, **376**, 238, 1995.

[32] B. Hammer, *Topics in Catal.,* **37**, 3, 2006.

[33] S. Linic, M. A. Barteau, *J. Catal.,* **214** , 200, 2003.

[34] F. Studt, F. Abild-Pedersen, T. Bligaard, R.Z. Sørensen, C.H. Christensen, J.K. Nørskov, *Science*, **320**, 1320, 2008.

[35] T.S. Ahmadi, Z.L.Wang, C.T. Green, A. Henglein, M.A. El-Sayed, *Science,* **272**, 1924, 1996.

[36] Y. Sun, Y. Xia, *Science*, **298**, 2176, 2002.

[37] Y. Xia, Y. Xiong, B. Lim, S.E. Skrabalak, *Angew. Chem. Int. Ed.*, **48**, 60, 2009.

[38] ICIS News, *Ethylene Oxide (EO) Uses and Market Data*, (ICIS Publication May 2008; http://www.icis.com/v2/chemicals/9075772/ethylene-oxide/uses.html). [The easiest access to this source is by Internet]

[39] S. Linic, M.A. Barteau, "Heteroegenous catalysis of alkene epoxidation", Chapter 14.11.6 in *Handbook of Heterogeneous Catalysis*, 2nd edition, Ertl, G., Knozinger, H., Schuth, F., Weitkamp, J. (eds.), Wiley-VCH, 2007.

[40] D.J. Sajkowski, M. Boudart, *Catal. Rev. Sci. Eng.,***325**, 29, 1987.

[41] C. Stegelmann, N. C. Schiødt, C.T. Campbell, P. Stolze, *J. Catal.*, **221**, 630, 2004.

Chapter 2

Experimental and Theoretical Methods

2.1 Summary

In this chapter the details of the experimental and theoretical methods used throughout the dissertation are described. Specific focus is placed on the fundamental mechanisms that govern the synthesis of size and shape controlled Ag nanoparticles. The characterization instruments and reactor designs used to study (photo)catalytic properties are described, and the underlying principles of their operation are discussed. In addition, the theoretical tools (Density functional theory and Finite-difference time-domain) used to guide the synthesis of targeted materials are explained in detail.

2.2 Introduction

This dissertation utilized a combined experimental and theoretical approach towards the design of catalytic and photo-catalytic materials for energy efficient chemical conversion processes. Significant emphasis is placed throughout the dissertation on the shape and sized dependent optical and catalytic properties of well-defined Ag nanoparticles. This chapter starts with a detailed description of the synthesis approach used to control the size and shape of Ag nanoparticles. Attention is given to the synthesis variables that control the resulting particle shape. The methods for producing catalytically active forms of the Ag nanoparticles for various applications are then described. The arsenal of techniques used to characterize the nanoscale catalytic materials are described with specific focus on the instrumental setup and uses. Three different reactor setups were used to test various catalytic and photo-catalytic functions of well-defined Ag nanoparticles and are thoroughly described in this chapter. In addition, density functional theory calculations and finite-difference time-domain simulations were used to guide the synthesis of Ag nanoparticles with desired sizes and shapes and are explained.

2.3 Shape and Size Controlled Synthesis of Ag Nanoparticles

In this section the general approach for the shape and size controlled synthesis of Ag nanoparticles is discussed and contrasted from the classical methods used to synthesize supported metal catalysts. The key parameters throughout the synthesis that control the resulting geometry of the Ag nanoparticles are described in terms of the underlying physical mechanisms.

Typically, catalytic particles are synthesized by dispersing a metal salt on a ceramic supporting material. The salt is exposed to a gas phase reductant at high temperature to reduce the metal cations into metallic species, followed by calcination (high temperature oxidation) to remove contaminants left over from the decomposed salt.[i,ii] Utilizing this approach, the resulting metal particle geometry is dictated through the thermodynamics of the metal surface facets and the thermodynamics of the interaction between the metal and supporting material.[iii] The main parameters that dictate the resulting metal particle size are the initial dispersion of the metal salt on the support and the temperature of the reduction and calcinations processes.[iv] The thermodynamic properties of the metal/support control the resulting shape of the particle, meaning that there is very little rational control over the exposed surface structure of the catalytic particle using vapor phase synthesis methods.

As opposed to vapor phase synthesis conditions, solution based synthesis of metallic nanoparticles provides a number of strategies for manipulating the growth of metal nanostructures to achieve desired sizes and shapes. In solution based synthesis approaches there are four crucial steps that play a role in controlling the nanoparticle size and shape: reduction of the metal salt, nucleation of seeds, etching of seed particles and controlled nanocrystal growth.[v] Figure 2.1 shows a schematic of the growth steps allowing shape control through a solution based synthesis process. In each step there are tunable variables that can be used to adjust the kinetics and thermodynamics associated with the physical processes, allowing excellent ability to control the final size and shape of metal nanoparticles. In this section, the general approach towards shape- and size-controlled synthesis of Ag nanoparticles using the polyol synthesis method will be

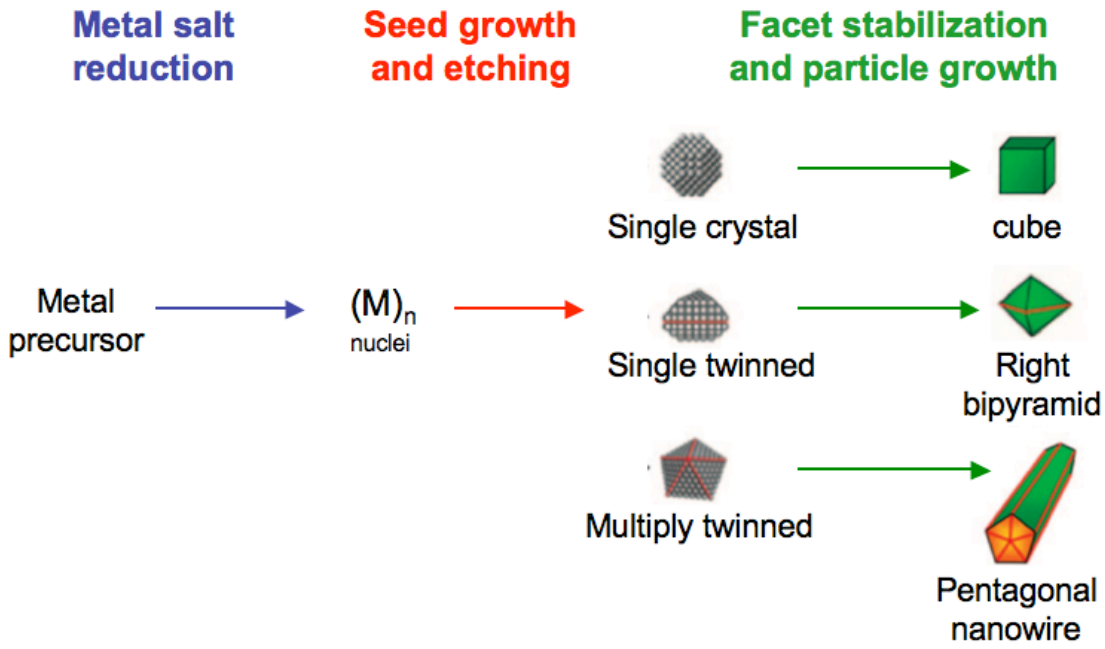

Figure 2.1 Shape controlled synthesis procedure. The figure shows a schematic of the approach used in this dissertation to control the shape of metallic nanoparticles, through the polyol synthesis method. The figure is adapted from Xia *et. al.*[v]

described. Focus will be placed on the synthesis of pentagonal cross-section Ag nanowires and Ag nanocubes. At the beginning of chapters 3 through 8, specific synthesis procedures are described for the different sizes and shapes of Ag nanoparticles used in the studies.

Figure 2.2 shows a schematic of the synthesis apparatus. Small scale synthesis is typically carried out in 20 mL glass vials, submerged in a heated bath consisting of silicone based heating oil. The heating oil is typically heated to 140-160^{o} C. The rate of introduction of reagents to the synthesis vessel is controlled using a syringe pump. The vessel is constantly stirred to ensure the solution is always well mixed with no-local concentration gradients, which could induce particle nucleation or growth. Oxygen is added or removed from the system simply by either leaving the vessel uncapped (introducing O_2), or by closing the air-tight seal to remove the flow of O_2.

In the polyol synthesis approach, heated ethylene glycol (EG) acts both as the solvent for the synthesis precursors and as the reductant for the metal salt. There is evidence that EG at elevated temperature (150^{o} C) in air, oxidizes to form glycolaldehyde (GA), which then acts as the primary reducing agent of the metal salt.[vi] Due to the importance of GA in the synthesis procedure, the initial solution of EG is heated in air for 1 hr prior to the addition of the synthesis precursors. It is important that the initial EG solution is heated for 1 hour, rather than more or less time, to keep the initial concentration of GA in the solution constant when the precursors are introduced. A small amount of HCl is added to the solution after the EG has been heated for approximately 1 hour. The HCl is used as an etchant to control the shape of the initial Ag seed; this is discussed in more detail below. Once the HCl is sufficiently mixed (about 10 minutes

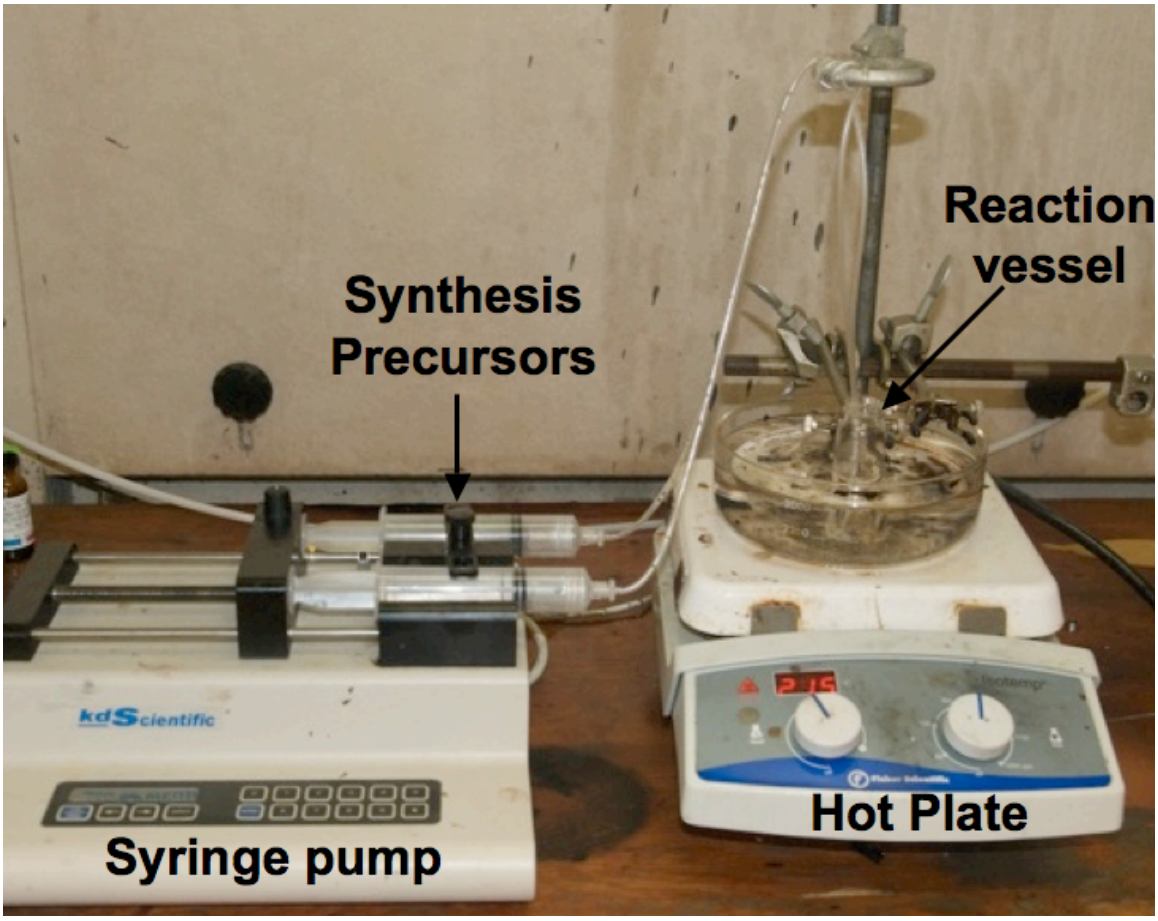

Figure 2.2 Solution based synthesis apparatus. The figure shows the apparatus used for shape and size controlled synthesis of Ag nanoparticles. The synthesis precursors are delivered from 30 mL syringes, using a 2-channel syringe pump. The 20 mL glass reaction vessel is submerged in a heated oil bath.

after injection) EG solutions containing the metal salt and the growth directing polymer are added drop-wise via syringe pump over the course of 5 minutes. The rate is chosen for 2 reasons, (i) to avoid high local concentrations of the precursors (reducing the possibility of seed nucleation) and (ii) to reduce the induced temperature change as the room temperature precursor solutions are added to the heated EG. Once the precursors are added to the heated EG, the solution is allowed to react, with the reaction vessel open to atmosphere to provide O_2, for a period of time between 4 and 24 hours to achieve the desired seed etching. Once the desired level of etching is achieved, the reaction vessel is closed off to the atmosphere causing particle growth to nucleate. During the growth process, the concentration of the growth-directing polymer (commonly polyvinylpyrrolidone) dictates the growth rate of various metal surface facets. Through this process, the shape and size can be controlled by varying the shape of the initial seeds (etchant), the growth rate along various surface planes (polymer concentration) and the overall particle growth rate (temperature and total metal concentration).[vii]

The initial step during the polyol synthesis method is the reduction of the metal salt to form metallic Ag^0 atoms. Although EG is the only solvent used in the synthesis procedure, it was shown recently that EG readily oxidizes in air, at temperatures between 140-160^o C (ie. the temperatures used herein), to form glycolaldehyde, a much stronger reductant.[viii,ix] The role of GA in the reduction of $AgNO_3$ to form Ag^0, in the polyol process, was shown directly through a series of titration experiments.[vi] These experiments clearly showed that the pre-treatment of EG in air (O_2) at elevated temperature is critical for the production of the primary reductant, GA, which allows quick and homogeneous reduction of the $AgNO_3$ to form Ag^0 in solution. In addition,

these studies highlight the importance of consistency in the pre-treatment procedure (temperature, duration and environment) of the initial EG. In all synthesis in this dissertation a common pretreatment of heating the EG to 145^{o} C, in air, for a period of 1 hour was used prior to the addition of synthesis precursors.

After the EG is pretreated for 1 hour, the synthesis precursors are added, starting with a small amount of HCl (yielding a final concentration of $2.7*10^{-4}$ M in the reaction vessel) followed by the addition of PVP and $AgNO_3$, typically in a 1.5:1 molar ratio (yielding final concentrations of $2.7*10^{-2}$ M and $4.1*10^{-2}$ of $AgNO_3$ and PVP respectively). Once the addition of the precursors is complete, the cap is loosely placed on the reaction vessel, to allow air flow in and out of the synthesis vessel, but also acting to reflux any evaporating EG. Following the addition of the synthesis precursors the solution turns a faint yellow color, indicating the formation of small Ag seeds. The faint yellow color is attributed to the excitation of surface plasmons on small, < 5nm diameter, Ag nanoparticles. High-resolution transmission electron microscopy (HR-TEM) experiments have shown previously that the initial seed particles formed in the polyol process are multiply twinned particles (MTP) of 1-10 nm diameter.[x] After a short period of time 0.5 - 3 hours, the solution slowly looses color and becomes clear. This indicate that the MTP seeds formed initially are dissolved and return to solution, either as Ag^0 species, or as very small clusters.[xi] If the HCl is not added to the solution, the initial multiply twinned Ag seeds will not dissolve back into solution, but will continue to grow into larger Ag particles with a mix of geometries. It is worth noting that clusters below about 2 nm in diameter do not exhibit a plasmon resonance, thus even if there were small seed clusters forming, there would be no associated coloration of the solution. The

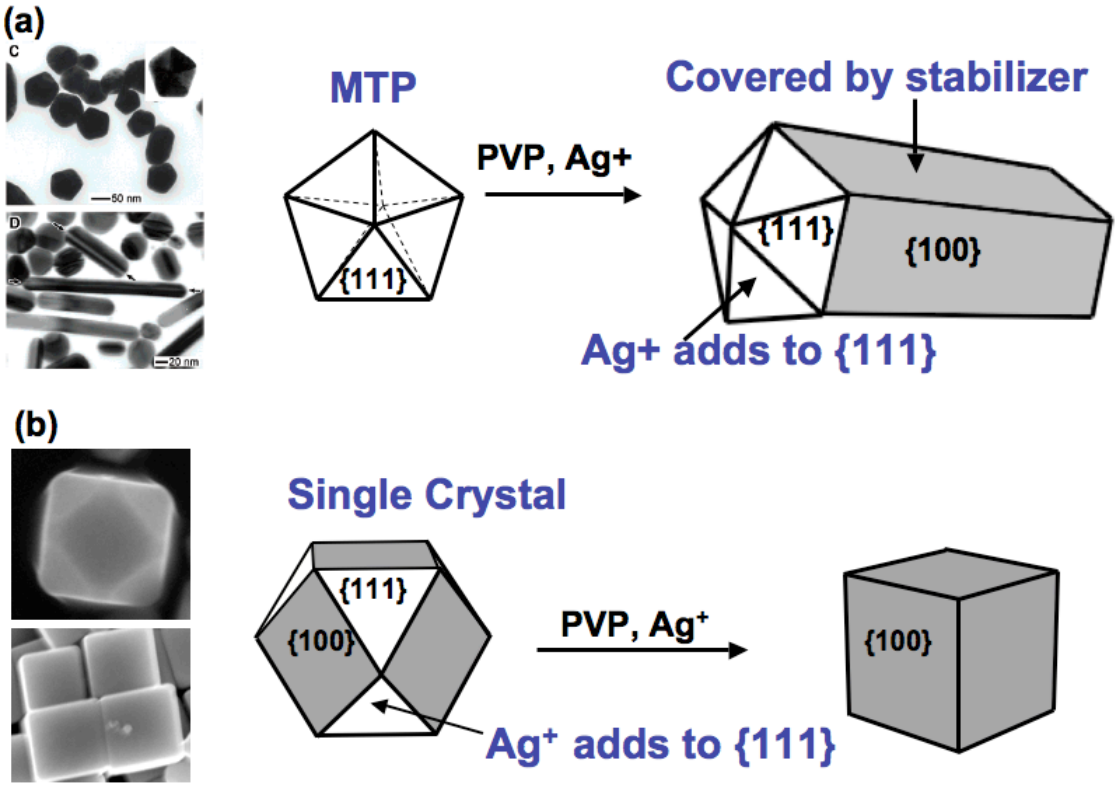

Figure 2.3 Growth mechanism for Ag nanowires and nanocubes. (a) The schematic shows the growth mechanism for Ag nanowires. Initially dodecahedron Ag nanoparticle seeds form (a TEM is shown on the left of the seed particles).[x] Ag^+ ions begin to add to the (111) facet, thereby elongating the Ag nanowire (a TEM image is shown to the left).[x] (b). The schematic shows the growth mechanism of Ag nanocubes. Single crystal seeds are initially formed (a SEM image of this is shown on the left). Ag^+ ions once again add to the (111) facet, but because of the initial seed shape, cubic Ag nanoparticles are produced.

size and shape dependent properties of Ag surface plasmons are discussed in detail in chapter 3.

After the dissolution of the initial seed particles, it has been proposed that very small seed clusters (< 2 nm diameter) form and are continuously etched by a combination of O_2 and Cl^- ions.[xii] At this point the resulting Ag nanoparticle geometry is controlled by the incubation, or etching time, used to shape the seed geometry as well as the initial concentration of PVP added to the solution. If the cap on the reaction vessel is closed within 4 to 6 hours of the start of the synthesis, the majority resulting product is pentagonal Ag nanowires. The growth mechanism of pentagonal Ag nanowire formation is shown in Figure 2.3. The initial seed particle geometry must be a dodecahedron MTP Ag seed. When growth is nucleated (by removing O_2 flow), the PVP stabilizer is selectively bound to the (100) facets that are located along the perimeter of the intersection of the two pentagonal ends. The stronger binding of the PVP molecules to the (100) facet compared to the (111) facet dictates that Ag^0 species that are in solution will selectively attach to the (111) facets during the growth process. This results in anisotropic growth of the nanoparticles, producing long pentagonal cross section nanowires that are terminated in (100) facets around the circumference and (111) facets at the tips, Figure 2.3. Scanning electron micrograph images of the resulting nanowires are shown in Figure 2.4, showing the expected pentagonal geometries and high uniformity in terms of size and shape.

The growth process for forming Ag nanocubes is very similar to pentagonal nanowires. The major difference is the time allowed for the seed etching process. If the solution is allowed 15-24 hours of incubation time, prior to removing the O_2 supply, the

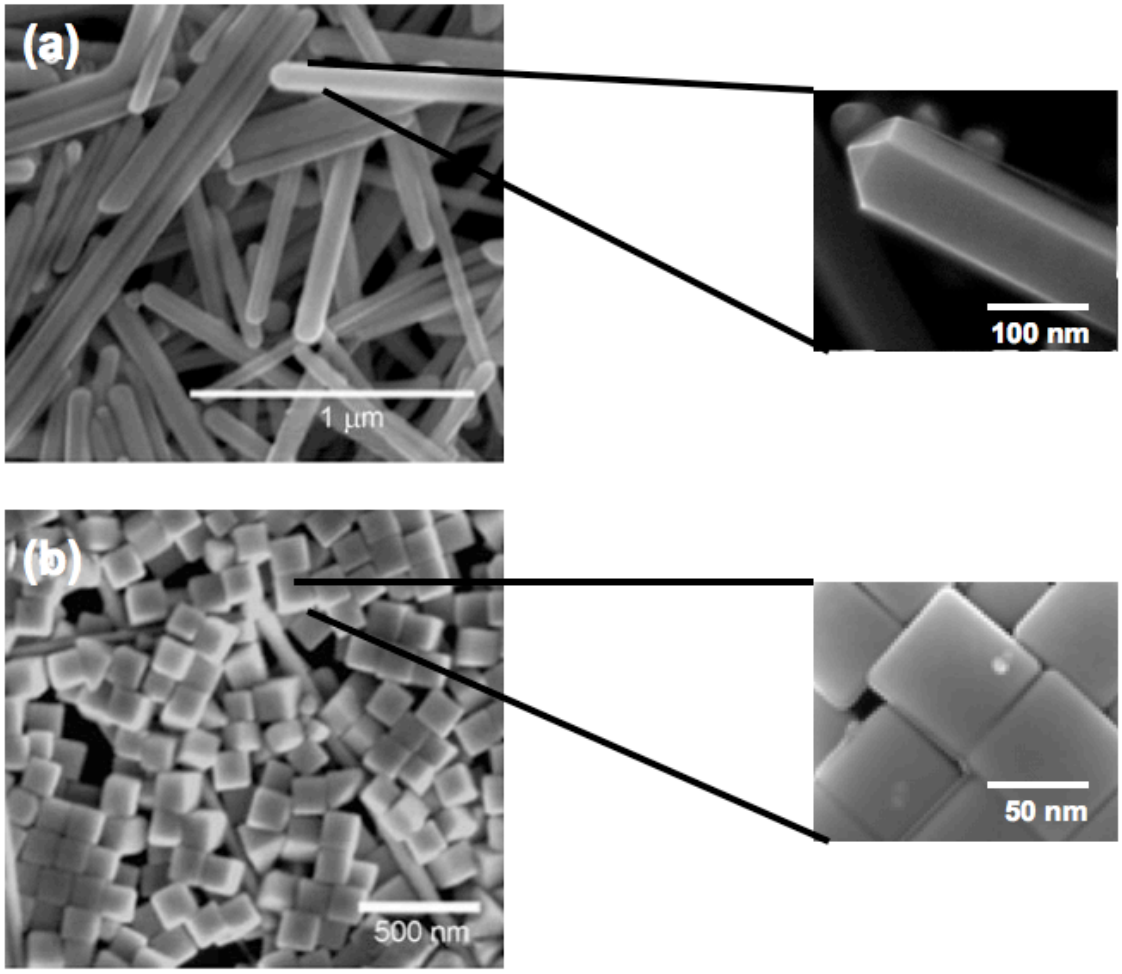

Figure 2.4 SEM images of Ag nanocubes and nanowires. (a) The large SEM shows a zoomed out micrograph of representative, 110 nm diameter nanowires synthesized through the polyol approach. The close up SEM image clearly shows the pentagonal shape of the Ag nanowires. (b) The large SEM shows a highly uniform (both size and shape) Ag nanocube sample, with average edge length of 90 nm. The close up SEM shows that the nanocubes have very sharp edges and well-defined shapes.

seed particles etch from multiply-twinned particles to cubeoctahedral single crystal particles. When growth is initiated from the single crystal seeds, the PVP selectively binds to the (100) facet once again, allowing growth perpindicular to the (111) plane. As shown in Figure 2.3, this growth process results in the formation of Ag nanocubes as the final geometry. Figure 2.4 shows SEM images of typical resulting Ag nanocubes synthesized using the polyol process with a long etching/incubation time.

2.4 Synthesis of Catalytically Active Materials

In this section the pre-treatment and deposition of the solution-synthesized Ag nanoparticles onto various supports is described. The major variation in the supporting materials described in dissertation is the surface area and geometry. Three different reactor geometries are described in this dissertation, and for each configuration a different supporting material was utilized.

2.4.1 Monolith Supported Ag Nanoparticle Catalysts

The nanostructured catalysts were prepared by first separating the Ag nanoparticles from ethylene glycol (the synthesis medium) and any remaining un-reacted pre-cursors ($AgNO_3$ or PVP) from the synthesis.[vii,xiii] This is achieved through centrifugation. Typically the as synthesized Ag nanoparticle solution in ethylene glycol was diluted 5-fold with acetone and centrifuged at 6000 RPM for 20 minutes. This process deposited the Ag nanoparticles in a pellet at the bottom of the centrifuge tube and allowed removal of the solvents. The pellet was re-dispersed in 5 mL of ethanol and diluted 10-fold with acetone and centrifuged again. This process was repeated 5 times prior to deposition onto the monolith support.

The α-Al_2O_3 monolith was purchased from an industrial supplied (99.5%, Vesuvius Hi-Tech Ceramics) and is characterized by a very low surface area, ~0.3 m^2/g. The monoliths were 15 mm in diameter and ~5 mm in length. The size was chosen such that each monolith weighed 1.0 g. Prior to use, the monoliths were boiled in de-ionized water for 1 hour. The Ag nanoparticles were dispersed in 3-5 mL of high purity ethanol (99.9 % Alfa Aesar) for impregnation onto the monolith support. The solution was drop coated onto the monolith and allowed to dry at 70 °C in air. The weight loadings were estimated, knowing the concentration of nanoparticles in solution and verified by weighing the support before and after impregnation. The weight loadings were varied to ensure similar active (Ag) surface areas on all catalysts tested, regardless of particle size and shape. Typically the surface coverage on the monolith supports was about 10%. The surface coverage is defined as the portion of the Al_2O_3 surface that is covered by Ag.

2.4.2 Powdered Al_2O_3 Supported Ag Nanoparticle Catalysts

The preparation procedure for the Ag nanoparticles used on powedered Al_2O_3 supported catalyst is identical to the procedure outlined above.[xiv] The centrifuged Ag nanoparticles, in an ethanol/Ag nanoparticle solution was added to 100 mg of alpha-Al_2O_3 (Alfa Aesar # 42571) in a 20 mL vial and sonicated for 1 hr. The powered Al_2O_3 had a surface area of 5-6 m^2/g, which is an order of magnitude higher than the surface area of the molithic support. The solution was dried at 70 ^{0}C in air, allowing for almost all Ag nanoparticles to adsorb to the Al_2O_3 surface. The powdered Al_2O_3 supported Ag nanoparticle catalysts were ~20% weight loading, with a typical surface coverage of 10-15%.

2.4.3 Thin Film Ag/TiO_2 Nanoparticle Composite Films

This synthesis procedure aimed to produce composite films, consisting of a sub-monolayer coverage of Ag nanoparticles, coated by 2-3 layers of TiO_2 nanoparticles on an SiO_2 support.[xv] The synthesis procedure was optimized to allow for homogeneous film properties (geometric and optical) across the substrate. The as synthesized Ag nanoparticles were washed only once with acetone via centrifugation and re-dispersed in 200 proof ethanol. This procedure removed non-reacted precursors from the solution but did not remove PVP from the surface of the Ag nanoparticles. $1cm^2$ SiO_2 substrates were pre cleaned using a 2 minute etch in HF followed by sonication in ultra-pure water prior to use. The particles were drop coated onto pre-cleaned $1cm^2$ SiO_2 substrates and allowed to dry in a stagnant atmosphere. The Ag nanoparticle geometry (size and shape) and concentration in solution (estimated from the amount of Ag added in the synthesis) were used to estimate the required drop coating volume needed to achieve a desired surface coverage. The highly pure ethanol was found to be crucial, as any contaminants in the solvent would cause for uneven or incomplete drying of the metal nanoparticle solution, producing non-homogeneous films. A solution of 2.3 mg of P25 TiO_2 particles in 2 mL of 200 proof ethanol was prepared and sonicated for 2 hours, prior to deposition onto the Ag nanoparticle films. 20 uL of this solution was deposited on the Ag nanoparticle covered or clean SiO_2 substrates and allowed to dry in a stagnant atmosphere. This procedure produced well-dispersed films with fairly uniform optical properties across the entire surface.

2.5 Nanostructure Characterization Methods

2.5.1 Scanning Electron Microscopy

Scanning electron microscopy (SEM) utilizes a high-energy electron beam to image conductive materials with a resolution of a few nanometers. The high-energy electron beam interacts with the sample, causing the ejection of electrons from surface atoms of the sample. The image is collected by creating a topographical map of electrons that were ejected from the sample by the high-energy beam. In this dissertation SEM was used to characterize the size and shape of metallic nanoparticles. In addition, this technique was used to analyze the effect of pre-treatment or reactive environments on the size and shape of metallic nanoparticles. Typically a series of 5 to 10 images were collected from each sample. Based on analysis of these images, the geometric features of the nanostructures were calculated. SEM was carried out using an FEI Nova 200 Nanolab. The accelerating voltage was varied between 5-25 kV depending on the sample characteristics and desired magnification.

2.5.2 Transmission Electron Microscopy (TEM) and Selected Area Electron Diffraction (SAED)

Transmission electron microscopy (TEM) is utilized to obtain high (atomic) resolution images of materials.[xvi] TEM transmits a focused, high-energy electron beam through a sample. The electrons scatter off the nuclei of atoms in the sample and are projected onto a fluorescent screen. Through this process, atomic scale images can be collected. In addition, a selected area electron diffraction (SAED) pattern can be obtained from single nanostructures, to analyze the orientation of crystallographic planes.

By combining the information gained from atomic scale imaging and diffraction patterns, the surface crystallographic planes of a material can be identified.[xvii,xviii] In this dissertation, a combination of TEM and SAED were used to index the crystallographic planes of Ag nanocubes and nanowires, and allow the identification of the exposed catalytically active surface structure. TEM images were collected utilizing a JOEL 3011 high resolution TEM.

2.5.3 X-ray Diffraction (XRD)

X-Ray Diffraction (XRD) is a technique that characterizes the crystal structure of materials. X-rays interact with the sample through elastic scattering from incident angles, which are characteristic of various crystallographic planes. XRD was used in this dissertation to analyze the crystal structure and orientation of various Ag nanoparticle shapes. XRD spectra were collected using a Cu-Kα on a Philips XRG5000 3kW X-ray generator with a Rigaku camera and a crystal alignment stage. Peaks were identified using Jade v.7 software.

2.5.4 UV-Visible Absorbance Spectroscopy

UV-visible absorbance spectroscopy analyzes the wavelength dependent interaction of photons with a material. Typically this technique is used to probe electronic transitions (excitation of electrons) in materials. A broadband visible source is passed through, or reflected from a sample, and the intensity of transmitted or reflected photons is analyzed as a function of wavelength. This provides a quantitative measure of the wavelength dependent absorption or scattering, resulting from light-matter

interactions. In this dissertation, UV-vis spectroscopy is used to analyze the wavelength dependent interaction of photons with metal and semiconductor nanoparticles. As discussed in detail in chapter 3, the intensity and spectral shape of the interaction of light with metallic nanoparticles provides information about the shape, size and external environment associated with nanostructures in a sample. Three different experimental configurations are used in this dissertation. The experimental setup and advantages of each approach is described in this section.

Transmission UV-vis absorbance spectroscopy is carried out by passing a broadband illumination source through a sample and analyzing the wavelength dependent extinction of photons, due to interaction with the sample (Figure 2.5(a)). Transmission UV-vis spectroscopy is typically used when the sample (either liquid or solid state) is sufficiently transparent to allow a significant fraction of photons to pass through the sample. The measured light extinction is compared to a "blank sample", which is typically the solvent or transparent support, to quantify the interaction of the probed material with photons. In addition, samples analyzed in transmission mode are generally nano-scale or solution phase species whose length scales do not approach the wavelength of the broadband light. As materials begin to scatter light, based on physical dimensions matching the photon wavelengths, additional features are seen in collected spectra that are not related to electronic excitations in the probed material. In this dissertation transmission UV-vis spectroscopy was used to analyze the size and shape of metallic nanoparticles in solution and in thin films supported on transparent SiO_2 surfaces. This provided a quick and simple tool that allows accurate estimation of metal nanoparticle size and shape, due to the geometry dependent plasmon resonance excitation (Chapter 3).

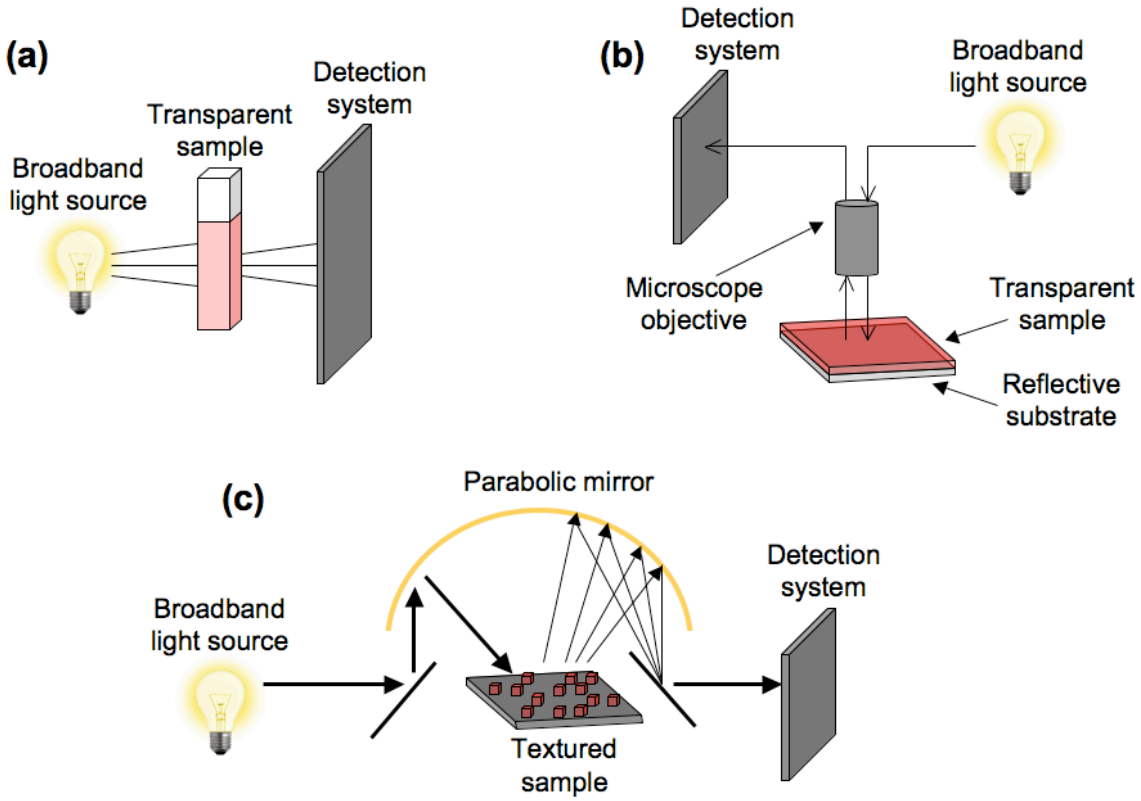

Figure 2.5 Experimental UV-Visible spectrometry setup. (a) A schematic of a transmission UV-vis measurement is shown. A broadband source is passed through a transparent sample (this can be a 2-d surface or a solution in a cuvette) and the remaining light that is not absorbed or scattered is analyzed by the detection system. (b) A reflection absorption UV-vis system is shown. The light source is focused on the sample through a microscope objective. Light that is not absorbed or scattered bounces off the reflective substrate and is routed to the detector. (c) A schematic of a diffuse reflectance UV-vis measurement is shown. The broadband source is focused on the sample, and a parabolic mirror is used to collect all diffusely scattered light, which is then focused on the detection system.

In this dissertation transmission UV-vis spectra were obtained using two different spectrophotometers: 8453 UV-vis Chem Station spectrophotometer (Agilent Technologies) and Evolution 300 Spectrophotometer (Thermo-Fisher).

Reflection absorbance UV-Vis spectroscopy is performed by bouncing a broadband source off of a sample and measuring the wavelength dependent intensity of photons that return due to direct specular reflection. The experiments are typically used to analyze the absorbance of a sample that is deposited onto a reflective surface. To quantify the interaction, a "blank" spectrum is collected that measures the wavelength dependent intensity of photons that are specularly reflected off a clean reflective surface. Materials are then deposited on the reflective surface, and the spectrum is collected. Once again, this technique is best suited for samples whose nanoscale features do not have characteristic dimensions that approach the wavelength of light produced by the broadband source. In this dissertation, reflection absorption UV-vis spectroscopy measurements were utilized to quantify the rate of photo-catalytic decomposition of methylene blue that was deposited on TiO_2 and Ag/TiO_2 composite photocatalysts. Measurements were recorded using an AvaSpec 2048 spectrometer and an AvaLight DHc compact deuterium halogen light source (Avantes). The light source passes through a beam splitter and is passed through an optical objective. The light is bounced off the sample, re-enters the objective and passes through a beam-splitter, en-route to the charge-coupled device (AvaSpec 2048 spectrometer), Figure 2.5(b).

Diffuse reflection UV-vis extinction spectra are collected by bouncing a collimated broadband photon source off of a textured surface or powdered sample. Diffusely reflected photons are collected by a spherical mirror and focused into a

detector, Figure 2.5(c). The diffuse reflectance experimental setup allows the measurement of light matter interactions, in systems that cannot be analyzed using the other two methods, due either to (i) the samples not being transparent (ie. absorbance is 100% across the entire wavelength region) and/or (ii) the characteristic lengths of the sample produce significant scattering effects. In this dissertation, diffuse reflectance UV-vis spectroscopy was used to analyze the optical properties of catalytically active metallic nanoparticles supported on Al_2O_3. Diffuse reflectance UV-vis spectra were recorded using a ThermoScientific Evolution 300 and the Harris Praying Mantis diffuse reflectance accessory.

2.5.5 Raman Spectroscopy

Raman spectroscopy utilizes a monochromatic laser source, to polarize electrons in molecular bonds. The polarization process can result in a loss of energy (Raman effect) that is characteristic of the energy of a probed molecular bond. The technique is complimentary to IR spectroscopy, because only molecular vibrations that are polarizable producing Raman shifted photons. The experimental setup involves a monochromatic laser that is focused on a sample using an optical objective. Reflected photons pass back through the objective, through a beam splitter and into the CCD detector. The setup is identical to the reflection absorption UV-visible spectroscopy experiments, only with different light source and CCD. Raman spectroscopy was used in this dissertation to analyze the chemical state of catalytic Ag surfaces under reaction conditions. Raman spectra were recorded using a Lambda Solutions Dimension-P1, with a 532 nm laser.

2.5.6 Photoluminescence Spectroscopy (PL)

Photoluminescence (PL) spectroscopy involves the photo-excitation of a material with a monochromatic source and monitors the intensity and wavelength dependence of the resulting inelastic photon emission from the sample. By modulating the excitation photon wavelength, the material dependent interaction with photons of various energies can be analyzed. In addition, for a given excitation wavelength PL measurements can provide quantitative information about material dependent efficiency of light absorption or emission. In this dissertation, PL measurements are used to quantitatively measure the effect of plasmonic metal nanoparticles on the light absorption in nearby TiO_2 semiconductor nanoparticles. PL measurements were made using Fluoromax-3 spectrofluorometer (Jobin Yvon/Spex Horiba, NJ) and custom designed sample holders.

2.5.7 X-Ray Photoelectron Spectroscopy (XPS)

X-ray photoelectron spectroscopy (XPS) utilizes a monochromatic X-ray source to excite electrons from core levels of the atoms in a sample into vacuum. The energy and intensity of the ejected electrons are then measured. The relative energy of the ejected electrons (calibrated with respect to a standard) provides quantitative information about the composition and chemical state of the sample. The technique is extremely surface sensitive, as X-rays typically only penetrate ~10 nm into a sample, allowing detection of trace contaminant species on catalytic surfaces. In this dissertation XPS was used to analyze the elemental makeup of as prepared and used catalysts, focusing specifically on looking for trace level amount of potential contaminants that could affect the catalytic properties (mostly Cl and Cs). In addition, XPS was used to analyze the chemical state of

the Ag catalysts used in a number of studies, specifically to show that the surface of the Ag catalysts was in a metallic state. XPS were collected using a Kratos Axis Ultra XPS with 150W Al X-Ray gun. Measurements were taken in a vacuum chamber with a base pressure of 10^{-9} Torr. The peak positions were calibrated with respect to the C1s peak.

2.6 Catalytic Reactor Experiments

2.6.1 Thermal Catalytic Ethylene Epoxidation

All thermal catalytic reactor studies were performed in a horizontally oriented tube reactor operated isothermally between 210-240 ^{0}C at atmospheric pressure. The setup utilized gas mass flow controllers to deliver reactants. All reactions were performed in 17 mm diameter quartz tubes, where monolithic catalysts (see section 2.4.1) were secured using quartz wool. The temperature was controlled based on thermocouple measurements in the reactor tube at the back end of the catalyst bed. Total inlet flow rate was kept constant at 100 standard cm^3 per minute (sccm); all gases used were the highest

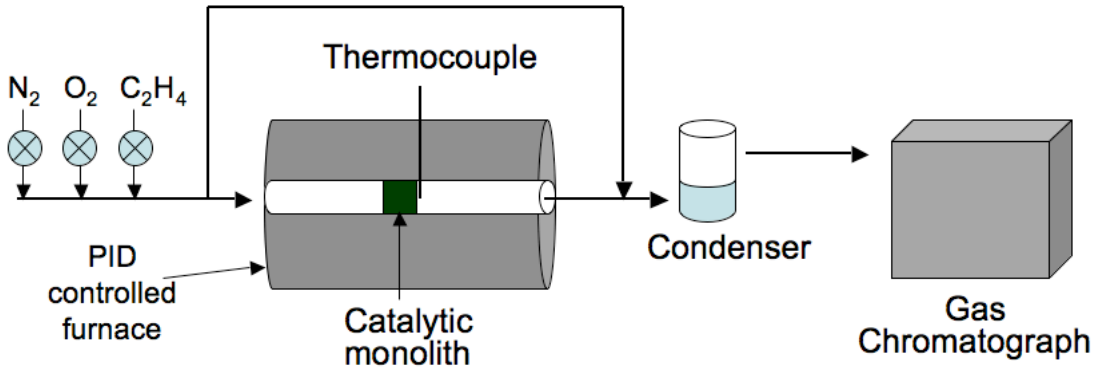

Figure 2.6 The figure shows a schematic flow chart of the horizontal reactor used in the pure thermal catalytic experiments. The gases are provided delivered using mass flow controllers. The temperature of the bed is controlled with a PID controller, utilizing a thermocouple placed at the back-side of the catalyst bed. A condenser was used to remove water prior to the GC.

purity available. All catalysts were pretreated in a mixture of 30 sccm O_2 and 70 sccm N_2 for 3 hours at 230 ^{0}C, prior to initiating the reaction. Once the pretreatment was complete all catalysts were allowed to run at 220 C in 10 sccm O_2 a nd C_2H_4 and 80 sccm N_2 until they reached steady state. To analyze the effect of external conditions, the O_2/C_2H_4 ratio was varied by increasing the O_2 flowrate, decreasing the N_2 carrier gas flowrate and holding the C_2H_4 flowrate constant. Product gases were analyzed in line with a Varian gas chromatograph (Varian CP 3800) equipped with thermal conductivity and flame ionization detectors (TCD and FID). All reactions were performed in the differential regime (conversion of ethylene < 5%) to ensure minimal rate of backward reactions. A schematic of the reactor setup is depicted in Figure 2.6.

2.6.2 Photocatalytic Methylene Blue Decomposition

Methylene blue (MB) decomposition was used as a test reaction to benchmark photocatalytic activity of composite materials. MB was deposited on the substrates by submerging the thin-film substrates in a 0.65 mM MB in ethanol solution for 2 hours, followed by rinsing with ethanol. The films were allowed to dry for 2 hours, in the dark, prior to photocatalytic testing. The photocatalytic experiments were performed using a 100W source with an emission wavelength of 365 nm and a FWHM of 4 nm, about 10 mW/cm^2 at the sample. The degradation of MB was monitored using reflection UV-vis spectroscopy every 1 minute for the course of the experiment. MB concentration was monitored by following the magnitude of the 650 mn absorption peak.

2.6.3 Photothermal Catalytic Reactions

Phototherrmal reactions (allowing control of catalyst temperature and illumination) were carried out in a vertically oriented temperature-controlled packed bed flow reactor with a 1 cm^2 SiO_2 window to allow visible light illumination. The catalyst bed was 3 mm deep consisting of a 2.5 mm layer of inert SiO_2 particles with an additional 0.5 mm layer of catalyst deposited on top of the SiO_2. The catalyst was pretreated in 20 sccm O_2 and 60 sccm N_2 for 2 hours at 220 ^oC prior to starting any of the reactions.

After the pre-treatment period, for ethylene epoxidation, 20 sccm of C_2H_4, 20 sccm O_2 and 60 sccm N_2 were introduced to the reactor and allowed to 24 hours at 220 ^0C to reach steady state. CO and NH_3 oxidation reactions were also performed with 20 sccm of the reductant. After this line-out period the temperature was varied to examine the

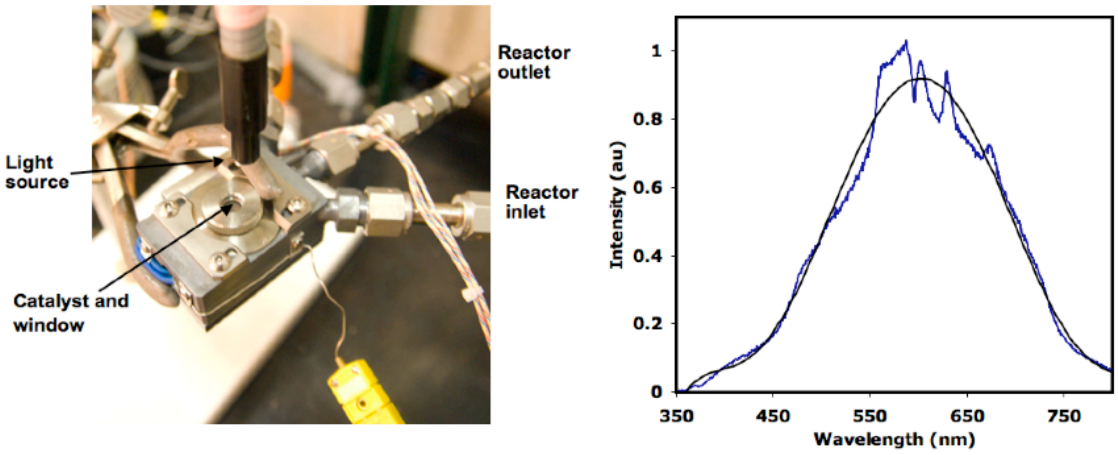

Figure 2.7 Photothermal reactor setup. On the left is a photograph of the Harrick reactor used for photothermal experiments. The light is provided via a fibre optic probe, and the inlet and outlet of the reactor are labeled. The figure on the right shows the spectra of the light source used throughout the dissertation. As well as the polynomial fit, used in the data analysis.

temperature dependent thermal and photothermal rate. At a given temperature the catalyst was allowed 15 minutes to reach steady state under dark conditions, followed by 15 minutes of visible light illumination, followed by 15 minutes in the dark to assure that the rate returned back to the initial value obtained in the dark. All catalytic tests were performed at less than 10% conversion to ensure the rate of backward reaction was minimal. All products were quantified online using quadrupole mass spectrometry (MS) and gas chromatography (GC). Both analyses produced consistent results for activity and selectivity for all reactions. The GC used is a Varian CP 3800 equipped with 2 TCD's and an FID. The MS is an Extorr XT200 operating at 10^{-6} Torr. We used a visible light source (Dolan-Jenner Fiber-Lite 180 halogen light) with a total maximum intensity of ~ 920 mW/cm^2 (2-3 times solar intensity) at the entrance of the catalyst bed and maximum spectral intensity at ~2.1 eV (590 nm). The reactor setup is depicted in Figure 2.7.

2.7 Density Functional Theory Calculations

Density functional theory is employed in this dissertation to calculate the energies and geometries associated with molecular species on surfaces. The calculations allow the comparison of adsorption energies of molecules on different catalytic surfaces, and the comparison of activation barriers associated with elementary surface chemical steps on different surfaces.[xix,xx,xxi] Density functional theory (DFT) relies on an effective electron density to describe a system of interacting electrons. Through this parameterization, the many body problem associated with N interacting electrons (which has 3N variables), is reduced to a problem with only the 3 spatial variables.[xxii,xxiii] Through this parameterization it is feasible to calculate the energy of large collections (up to a few

hundred) atoms. In addition, by applying periodic boundary conditions, energies associated with semi-infinite surfaces can be calculated that are excellent representations of real catalytic systems.

2.7.1 DFT Methodology

DFT calculations used in chapters 4 and 5 were performed using the Dacapo total energy plane wave code [https://wiki.fysik.dtu.dk/dacapo]. The Ag(100) and Ag(111) surfaces were modeled as a $2\sqrt{2}$ x $2\sqrt{2}$ supercell and a 3x3 supercell with 4 layers and 3x3x1 Monkhorst-Pack k-point sampling. The theoretical Ag lattice constant of 4.14 Å was used in all calculations. The slabs were separated in the z-direction with 6 layers of vacuum. The top 2 layers of the slab and the adsorbates were allowed to completely relax, in order to optimize geometries. The forces were minimized to 0.1 eV/Å. The GGA-PW91 functional was used to describe the exchange correlation energy and potential.[xxiv] The PW91 density was calculated self-consistently by iterative diagonalization of the Kohn-Sham Hamiltonian and Pulay mixing of the electronic density.[xxv] An electronic temperature (k_bT) of 0.1 was used during calculations and all energies were extrapolated to 0 K. The plane wave basis, used to describe the Kohn-Sham one-electron states was cut off at 350 eV. Vanderbilt pseudo-potentials were utilized to describe the core electrons.[xxvi] Calculation parameters were chosen to ensure consistency with respect to surface coverage and k-point sampling between calculations on the Ag(111) and Ag(100) surfaces. These calculation parameters yielded adsorption energies of atomic oxygen and oxametallacycle consistent with those reported previously.[xxvii]

The minimum energy pathways for the transformation of the oxametallacycle (OMC) to ethylene oxide (EO) and acetaldehyde (AC) were obtained using the climbing image nudged elastic band (CI-NEB) algorithm.[xxviii] The inputs in these calculations are the initial state (OMC) and final state (EO and AC) geometries in their lowest respective energy configurations. Forces along the reaction pathway were minimized to 0.1 eV/Å .

2.7.2 Linear-Expansion Delta Self-Consistent Field DFT (ΔSCF-DFT)

In Chapters 7 and 8 DFT calculations are used to map out the potential energy surface associated with O_2 dissociation on Ag(100) for a neutral O_2 molecule and an O_2 molecule with an extra electron removed from the Ag Fermi Level and localized in the O_2 $2\pi^*$ state. [xxix] DFT calculations were performed using the GPAW code, a real-space grid-based DFT implementation with the projector-augmented wave method.[xxx] The exchange-correlation interaction was approximated using the revised Perdew-Burke-Ernzerhof (RPBE) functional.[xxxi] The Ag(100) surface was modeled by a 2×2×3 slab with 10 Å of vacuum space. Oxygen molecule was adsorbed parallel to the Ag-Ag bridge, which was found to be most stable adsorption configuration of the O_2/Ag(100) system. The O_2 adsorbate and top two layers of the slab were allowed to relax until the force on all atoms was converged to less than .05 eV/Å.

The ground state and the excited state potential energy surface of O_2 has been mapped out in terms of the internal stretch of O-O bond using 18 irreducible k-points and a grid spacing of 0.2 Å. The linear-expansion Delta Self-Consistent Field (ΔSCF-DFT) method implemented in GPAW has been used to calculate the energetic of the electron excitation from the Fermi level to the O_2 $2\pi^*$.[xxix] The ΔSCF-DFT is executed in a very

similar fashion as standard DFT, with the major difference being, 1 or more electrons are placed in higher energy Kohn-Sham states, rather than all electrons being in the lowest possible energy states. Excited electrons are allowed to populate orbitals that are linear combinations of Kohn-Sham orbitals. This method has been shown to accurately capture resonance energy states predicted by time-dependent DFT and measured by inverse-photoemission spectroscopy.

2.8 Finite Difference Time Domain Simulations

Finite-difference time-domain simulations allow the elucidation of the light-matter interactions, under steady state illumination and dynamical conditions.[xxxii] The simulations provide a route to understand the effect of the shape, size, composition and environmental surroundings of nanoscale materials on their interaction with an incoming photon flux. In this dissertation, FDTD simulations were used specifically to explore the effect of geometry and environmental conditions of metallic nanoparticles on their plasmonic properties. These interactions are discussed in detail in chapter 3.

The interaction of light with the Ag nano-particles was simulated using FDTD method. FDTD is a computational electro-dynamics modelling technique, which solves discretized Maxwell equations in space and time subject the input geometry, material properties, and boundary conditions.[xxxiii] The optical properties of Ag are represented using a Drude-Lorentz model[xxxiv] with empirical optical constants[xxxv], which has been shown to give accurate results for Ag nano-structures.[xxxvi] Extinction, scattering, and absorbance cross-sections were calculated using the total-field/scattered-field (TFSF) formalism.[xxxiii]

2.9 References

[i] C.N. Satterfield, *Heteroegenous Catalysis in Industrial Practice, 2nd Ed.* McGraw Hill Book Co., New York, NY, 1991.

[ii] M. Campanati, G. Fornasari, A. Vaccari, *Catal. Today*, **77**, 299, 2003.

[iii] P.L. Hansen, *et. al., Science*, **295**, 2053, 2002.

[iv] J.A. Farmer, C.T. Campbell, *Science*, **329**, 933, 2010.

[v] Y. Xia, Y. Xiong, B. Lim, S.E. Skrabalak, *Angew. Chem. Int. Ed.*, **48**, 60, 2009.

[vi] S.E. Skrabalak, B.J. Wiley, M. Kim, E.V. Formo, Y. Xia, *Nano Lett*, **8**, 2077, 2008.

[vii] P. Christopher, S. Linic, *ChemCatChem,* **2**, 78, 2010.

[viii] R.A. Basson, T.A. Du Plessis, *Analyst,* **92**, 463, 1967.

[ix] Y. Xiong, I. Washio, J. Chen, H. Cai, Z.-Y. Li, Y. Xia, *Langmuir*, **22**, 8563, 2006.

[x] Y. Sun, B. Mayers, T. Herricks, Y. Xia, *NanoLett*, **9**, 955, 2003.

[xi] S.H. Im, Y.T. Lee, B. Wiley, Y. Xia, *Angew. Chem. Int. Ed.,* **117**, 2192, 2005.

[xii] B. Wiley, T. Herricks, Y. Sun, Y. Xia, *Nano Lett.*, **4**, 1733, 2004.

[xiii] P. Christopher, S. Linic, *J. Am. Chem. Soc.,* **130**, 11264, 2008.

[xiv] P. Christopher, H. Xin, S. Linic, *Nature Chem.,* **3**, 467, 2011.

[xv] P. Christopher, D. B. Ingram, S. Linic, *J. Phys. Chem. C*, **114**, 9173, 2010.

[xvi] D.S. Su, *ChemCatChem*, **3**, 919, 2011.

[xvii] J. Reyes-Gasga, J.L. Elechiguerra, C. Lui, A. Camacho-Bragado,J.M. Montejano-Carrizales, M.J. Yacaman, *J. Cryst. Growth,* **286**, 162, 2006.

[xviii] D.S. Su, T. Jacob, T.W. Hansen, D. Wang, R. Schlogl, B. Freitag, S. Kujawa, *Angew. Chem., Int. Ed.,* **47**, 1, 2008.

[xix] J.K. Nosrkov, T. Bligaard, J. Rossmeisl, C.H. Christensen, *Nature Chem.*, **1**, 37, 2009.

[xx] S. Linic, J. Jankowiak, M.A. Barteau, *J. Catal.*, **224**, 489, 2004.

[xxi] F. Abild-Pedersen, *et. al., Phys. Rev. Lett.*, **99**, 016105, 2007.

[xxii] P. Hohenberg, W. Kohn, *Phys. Rev.,* **136**, B864, 1964

[xxiii] W. Kohn, L.J. Sham, *Phys. Rev.,* **140**, A1133, 1965.

[xxiv] J.P. Perdew, J.A. Chevary, S.H.Vosko, K.A. Jackson, M.R. Pederson, D.J. Singh, C. Fiolhais, *Phys. Rev. B,* **46**, 6671, 1992.

[xxv] G. Kresse, J. Furthmuller, *Comput. Mater. Sci.,* **6**, 15, 1996.

[xxvi] D. Vanderbilt, *Phys. Rev. B***, 41**, 7892, 1990.

[xxvii] S. Linic, M.A. Barteau, *J. Catal.*, **214**, 200, 2003.

[xxviii] G. Hankelman, B.P. Uberuaga, H. Jonsson, *J. Chem. Phys.,* **113**, 9901, 2000.

[xxix] J. Gavnholt, T. Olsen, M. Engelund, J. Shiøtz, *Phys. Rev. B*, **78**, 075441, 2008.

[xxx] J.J. Mortensen, L.B. Hansen, K.W. Jacobsen, *Phys. Rev. B,* **71**, 035109, 2005.

[xxxi] B. Hammer, L.B. Hansen, J.K. Nosrkov, *Phys. Rev. B,* **59**, 7413, 1999.

[xxxii] E. Ozbay, *Science,* **311**, 189, 2006.

[xxxiii] A. Taflove, S.C. Hagness, *Computational Electrodynamics: The Finite-Difference Time-Domain Method*, 3rd. ed.; Artech House, Inc.: Norwood, MA, 2005.

[xxxiv] W. Ashcroft, N.D. Mermin, *Solid State Physics*, Brooks Cole, 1976.

[xxxv] E.D. Palik, ed., *Handbook of Optical Constants of Solids*, Academic Press: San Diego, 1985.

[xxxvi] J.M. McMahon, *et. al., J. Phys. Chem. C,* **113**, 2731, 2009.

Chapter 3

Shape and Size Dependent Properties of Metallic Nanoparticles

3.1 Summary

In this chapter the shape and size dependent properties of metallic nanoparticles, that are exploited throughout this dissertation, are discussed. It is shown that by controlling the size and shape of Ag nanoparticles, the concentration of various surface facets can be rationally manipulated. Focus is placed on the ability to vary the concentration of (111), (100) and highly undercoordinated surface atoms. In addition the size and shape dependent interaction of Ag nanoparticle with photons in the UV and visible region is discussed. The interaction of Ag particles with UV and visible photons is manifested through the excitation of surface plasmons. It is shown that the wavelength dependence and strength of the interaction between photons and Ag nanoparticles can be controlled by synthesizing targeted geometric structures.

3.2 Introduction

With the advent of effective synthesis methods for well-defined metallic nanoparticles, there has been a significant increase research focused on understanding the physical and chemical properties that can be manipulated by controlling the nanoparticle size and shape. As the nanoparticle diameter increases from a few angstroms (small clusters) to 5 nm, the bulk electronic structure of the particle becomes fully developed and the particle displays fully metallic characteristics.[1,2] Beyond this initial regime, where the metallic electronic structure is developing, metal nanoparticles display various shape and size dependent properties including surface structure geometry and optical properties.[3,4,5]

A major focus of this dissertation is to use shape and size controlled synthesis of metallic nanoparticles to control catalytic and photocatalytic properties.[6,7,8,9,10] This chapter introduces the shape and size dependent properties of Ag nanoparticles that are exploited throughout the dissertation. It is well known that variations in the geometric structure of metallic surfaces can play a major role in dictating its catalytic function.[11,12,13] In this chapter the shape and size dependent surface structure of Ag nanoparticles will be described. In addition, noble metal nanoparticles (Ag, Au and Cu in specific) are known to exhibit strong interactions UV and visible photons through the excitation of surface plasmons.[14,15] The second half of this chapter introduces the fundamental physics of surface plasmons and discusses the size and shape dependent plasmonic properties of Ag nanoparticles.

3.3 Size and Shape Dependent Surface Structure

The effect of the geometric characteristics of metal surface structure on catalytic function has typically been explored using either: various single crystal surfaces in a high pressure catalytic environment[16], or by employing supported catalytic particles with sizes varying between 2 and 20 nm diameter.[7,11] Through these studies it has been discovered that the nature of the metal surface structure, most commonly characterized by the coordination number (number of nearest neighbors) of surface atoms, can play an enormous role in dictating the activity or selectivity of a metal for a particular reaction. For example, in ammonia synthesis over Fe or Ru nanoparticles it was found there is 3 orders of magnitude difference in the reaction rate when comparing highly coordinated (n = 9) and under-coordinated (n = 5) surface sites.[17] Due to this huge difference, syntheses strategies for Ru and Fe based catalysts with very small particle sizes, which maximize the concentration of under-coordinated sites, is crucial for the design of more active ammonia synthesis catalysts.

A model catalytic metal particle is shown in Figure 3.1(a). The schematic shows the distribution of surface atoms with different coordination numbers. It is easily seen, that typical catalytic metal particles display a wide variety of active sites. The most stable surface configurations, or surface facets, are those that contain higher coordination numbers. For example, in face-centered-cubic metallic structures, surface atoms in the (111) miller index facet, characterized by a hexagonally closed packed structure, have a coordination number of 9 and are the most thermodynamically stable surface configuration. Based on the large differences in reactivity and selectivity of active sites with different geometric arrangements it is obvious that typical metal catalytic particles are not fully optimized with regards to homogeneous distribution of desired active sites.

The ability to control the shape and size of metallic nanoparticles allows the manipulation of the concentration of various configurations of atoms at the surface of nanoparticles and thus is a highly desirable approach for optimizing catalytic function of metallic nanoparticles.

In vapor phase synthesis approaches where the thermodynamics of various surface configurations control the final shape of the nanoparticle, the (111) facet dominates the nanoparticle surface even at small diameters (d > 7 nm).[18] As a result of thermodynamics, nanoparticles synthesized using these approaches are characterized by a semispherical shape, see Figure 3.1(a). Figure 3.1(b) shows how the concentration of atoms on an Ag nanoparticle surface, with various coordination numbers, change as the diameter is varied. This analysis assumes a cube-octahedral particle shape, where the surface energies of various facets dictate their concentration on large particles. This analysis approach has been shown to accurately capture the experimentally determined shape of Ag nanoparticles. The figure shows that at large diameters (d > 50 nm), Ag particles are dominated by (111) and (100) surface facets, with a ratio of $SA_{(111)}/SA_{(100)} \sim 1.33$. As the particle size is reduced below 50 nm diameter the concentration of under-coordinated sites increases significantly. It is important to understand that when using classical synthesis approaches, size is the only variable that allows one to tune the surface structure of metallic nanoparticles. Due to this constraint there have been very few examples of the direct comparison of the catalytic activity or selectivity of different surface sites on high surface area nanoparticle catalysts. This constraint has motivated the development of synthesis approaches that allow much finer control of the concentration of various atomistic configurations at nanoparticle surfaces.

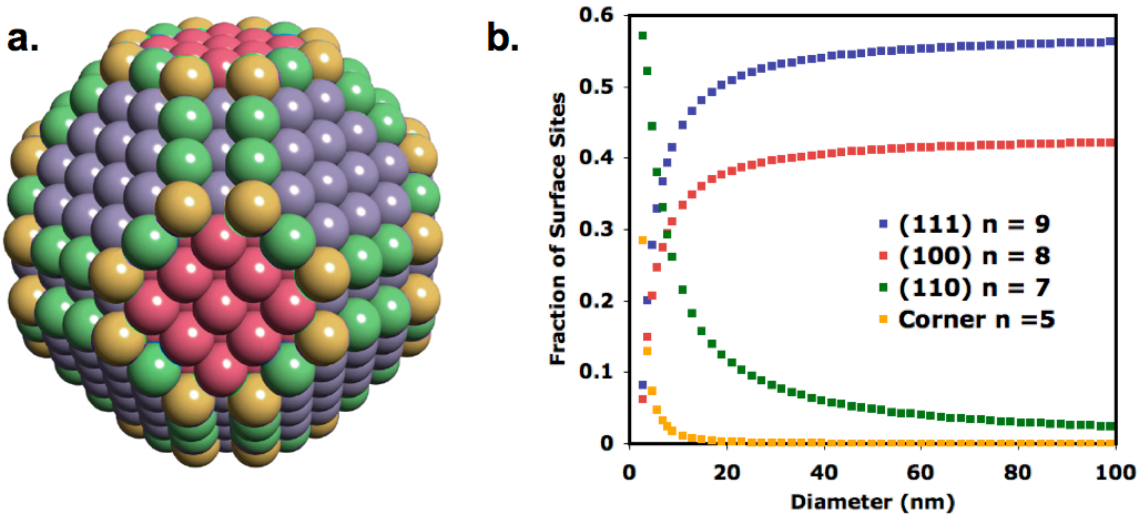

Figure 3.1 Nanoparticle surface structure. (a) The figure shows a schematic of a typical cubeoctahedral nanoparticle that is representative of many catalytically active metal nanoparticles. The atoms in blue have a coordination number, n, of 9; the atoms in red are n = 8; the atoms in green are n = 7 and the atoms in orange are n = 5. (b) The figure shows how the relative concentration of the various sites depicted in Figure 3.1(a) change as a function of the nanoparticle diameter.

As discussed in the previous two chapters, recent developments in the field of solution-based nano-synthesis have allowed the controlled synthesis of metallic nanoparticles with targeted sizes and shapes.[19,20] A major consequence of these advancements is the ability to synthesize nanostructures of different shapes that are characterized by different concentrations of various surface facets. Figure 3.2 shows 6 examples of different Ag nanoparticle shapes that were synthesized using the polyol approach method and the corresponding geometric structures that depict the various surface facets on each nanoparticle shape.[9] The figure shows that shape controlled synthesis approaches allow the relative concentration of the (111) and (100) surface facets to be tuned with respect to each other. This is not possible using a classical vapor phase synthesis approach.

The ability to control the size of different shaped nanoparticles also allows a direct comparison of the effect that different surface terminations have on catalytic function of metallic nanoparticles. For example, Figure 3.2 shows that the ratio of the surface area of the (111) and (100) facets is significantly different on various shapes of Ag nanoparticles. This shows that while keeping size constant, the nanoparticle shape can be systematically varied to analyze the effect of the (111)/(100) ratio on surface processes. In addition, due to the well-defined nature of particles synthesized through solution-based approaches, the effect of under-coordinated (edges and corners) sites on processes can be analyzed. Classic vapor phase syntheses methods have been previously utilized to vary the size of catalytic nanoparticles. But because of sometimes strong interactions between the nanoparticle and the support, the overall shape of the nanoparticle can vary as a function of size. On the other hand, with solution based

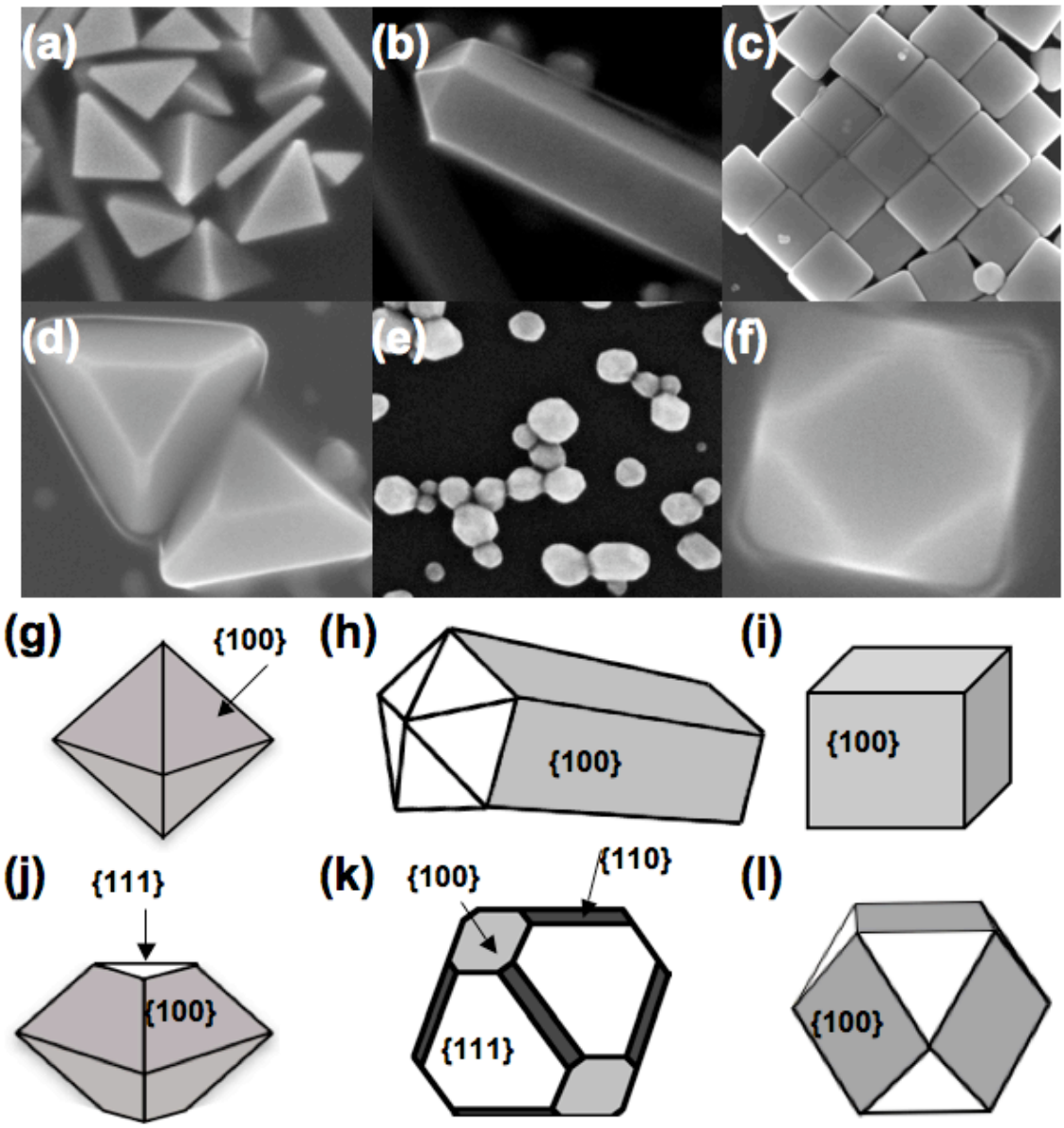

Figure 3.2 SEM images of various shapes and size of Ag nanoparticles synthesized using the polyol approach. (a)-(f) The SEM images show: right-bipyramids, pentagonal nanowires, nanocubes, truncated right-bipyramids, nanospheres and truncated cubes. The corresponding structural models are shown in (g)-(l).

synthesis approaches, complete control is allowed over the size and shape of the nanoparticles, prior to deposition on support. By utilizing these methods very careful studies of the size dependent catalytic properties of metallic nanoparticles can now be executed with confidence. These advantages of solution based approaches provide an excellent route for carrying out mechanistic studies on the effect of surface structure on catalytic function and optimizing particle geometry for both activity and selectivity in a surface catalyzed process.

3.4 Shape and Size Dependent Interaction of Ag Nanoparticles with Photons

3.4.1 Surface Plasmon Resonance Wavelength and Intensity

Nanoparticles composed of coinage metals exhibit strong interactions with photons in the UV and visible regime, through the excitation of surface plasmon resonance (SPR). SPR can be described as the resonant photon induced collective oscillation of valence electrons, established when the frequency of photons matches the natural frequency of surface electrons oscillating against the restoring force of positive nuclei.[1,2,4,8,10,14,15] The result of this interaction is the build up of strong, spatially non-homogeneous electric fields (photon intensity), at the surface of the plasmonic nanoparticle. Basically the strong interaction between resonant photons and the surface electrons, confines incoming photons to the surface of the nanostructure. By confining photons to the surface of the nanoparticles, the field intensity is significantly enhanced compared to the incoming field intensity. Figure 3.3 shows the field intensity, at the resonant wavelength, for an Ag nanosphere and nanocube with 50 nm characteristic lengths. The figure shows enhancements in the incoming field strength up to ~10^3 at

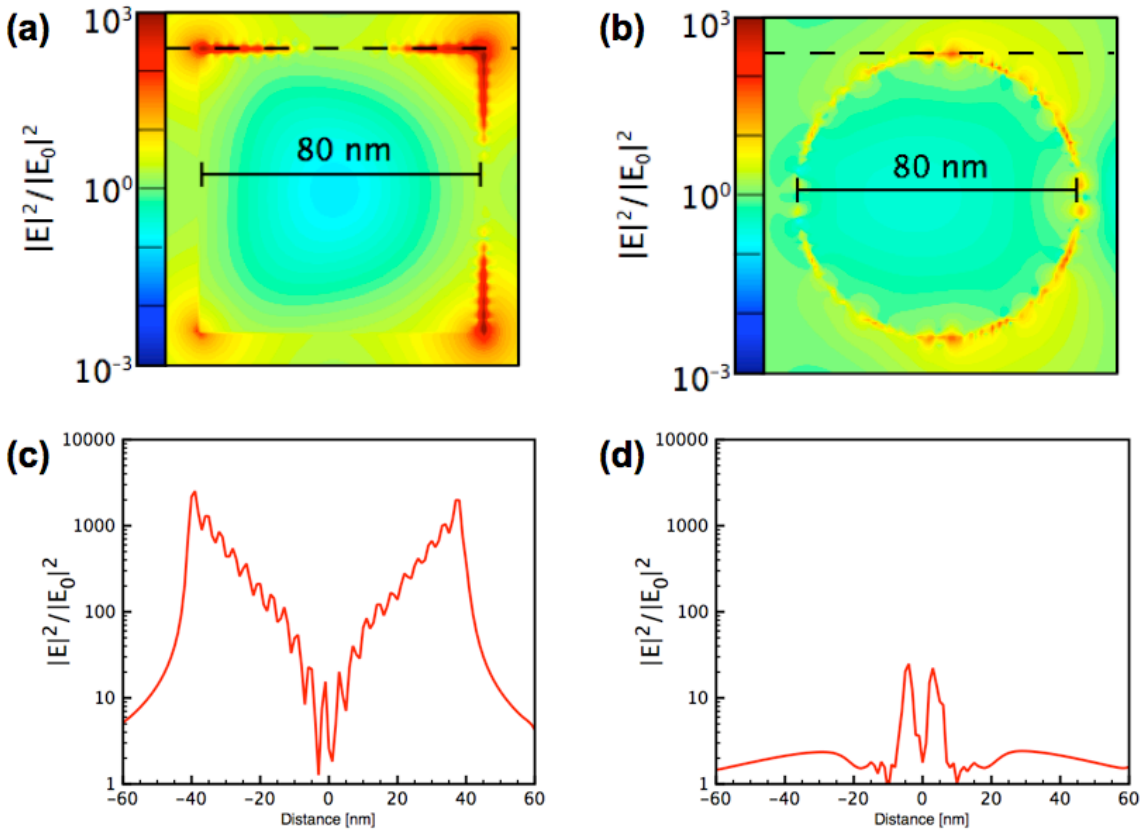

Figure 3.3 Light concentration at Ag nanoparticle surfaces. (a) The figure shows the electric field distribution around an 80 nm Ag nanocube when excited with photons at its resonant wavelength. The simulations were performed using FDTD approach. (b) The field intensity at the resonant wavelength for an 80 nm diameter Ag nanosphere. (c) This figure shows the electric field strength, 1nm above the top edge of the nanoparticle (the dotted line in Figure 3.3 (a)). (d) This figure shows the field intensity on a tangent line, 1 nm away from the sphere surface.

certain locations on the nanocube. The nanocube clearly exhibits stronger enhancements in the field intensity as compared to the nanosphere.

The shape dependent properties of plasmonic nanoparticles arise due to the fundamental property that surface plasmons are ***coherent*** oscillations of surface electrons across an entire nanostructure.[4] The energy and strength of the light matter interaction is defined by the nature of the surface electrons (material and environment dependent) and the size and shape of the nanoparticle. The shape and size basically dictate the extent to which electrons can coherently oscillate across the entire nanostructure. For example, the ability of electrons to coherently oscillate across the edge of a cubic shape particle will be completely different than the coherent oscillation around the circumference of a spherical particle. The shape and size dependence is analogous to controlling the resonant wavelength of a guitar string, ie. confining the resonant oscillation to shorter or longer

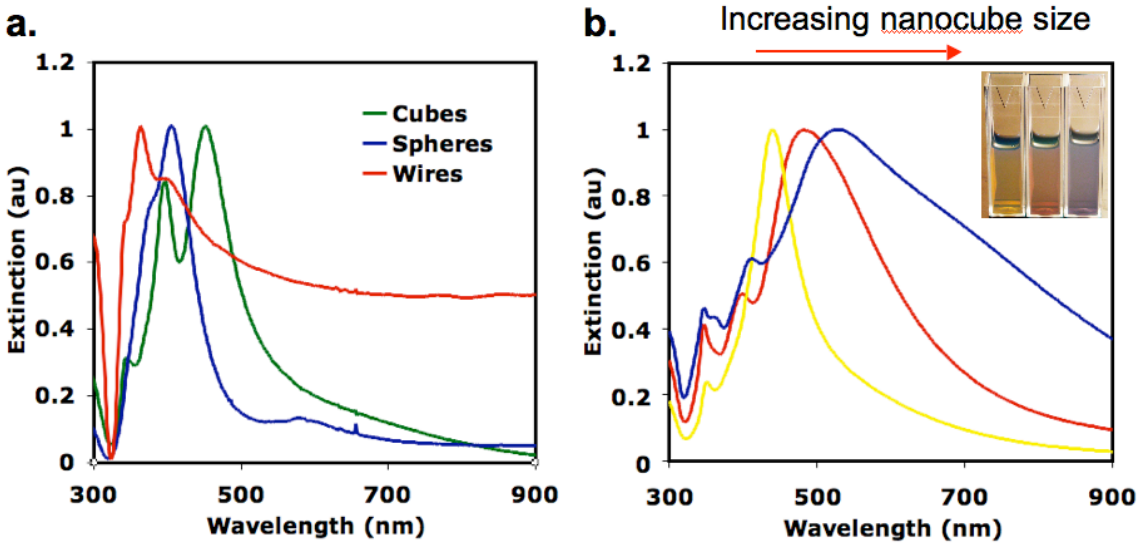

Figure 3.4 Shape and size dependent surface plasmon resonance. (a) The figure shows experimentally measured UV-vis spectra for films of Ag nanocubes, wires and spheres on SiO_2. (b). The figure shows experimentally measured UV-vis spectra for Ag nanocubes of increasing size. The inset shows the colors of these solutions.

distance will change the wavelength of the sound emitted. Excited plasmons have a similar quality, in that by manipulating the size and shape of the nanoparticle, the wavelength of the oscillation can be controlled.

Figure 3.4(a) shows that different shapes (nanospheres, pentagonal nanowires and nanocubes) of Ag nanoparticles, that are similar size, exhibit plasmon excitation wavelengths (the peak of the extinction spectra) that vary almost 200 nm. In addition, Figure 3.4(b) shows the extinction spectra measured from increasing sizes of Ag nanocubes in an ethanol solution. The figure shows that the peak wavelength shifts from 420 nm to 560 nm for Ag nanocubes ranging from 50 to 110 nm edge length. Further increase in the size will continue to shift the resonant wavelength to lower energies. Figure 3.4(a) and (b) show that by controlling the size and shape of Ag nanoparticles, the resonant wavelength for surface plasmon excitation can be shifted throughout the visible regime.

In addition to the shape and size of the particle, interactions between neighboring plasmonic particles can play a major role in dictating the resonance wavelength and field strength generated due to photon excitation. As plasmonic nanoparticles are brought close enough for their electric fields to interact there are three major consequences: a new resonance develops at an energy lower than that of the dipole peak of non-interacting particles (this is analogous to the creation of bonding and antibonding orbitals in molecular bonding theory), the plasmon lifetime is increased and the two resonating fields constructively interfere to significantly enhance the field strength.[21] Figure 3.5(a) shows how the extinction spectrum of a film of Ag nanoparticles changes as the density of Ag nanoparticles is increased. All spectra are from sub-monolayer covergae of Ag

nanocubes on a SiO_2 film. The formation of a new resonance state can be seen as the density of the nanoparticles increases to the point where there is significant interaction between the particles. Figures 3.5(b) and (c) show the field strength plotted for 80 nm Ag cubes that are separated by 1 nm. By comparing the field strength in Figure 3.5(b) to that of a single cube in Figure 3.3(a), it is obvious that the interaction between plasmonic particles significantly increases the field strength.

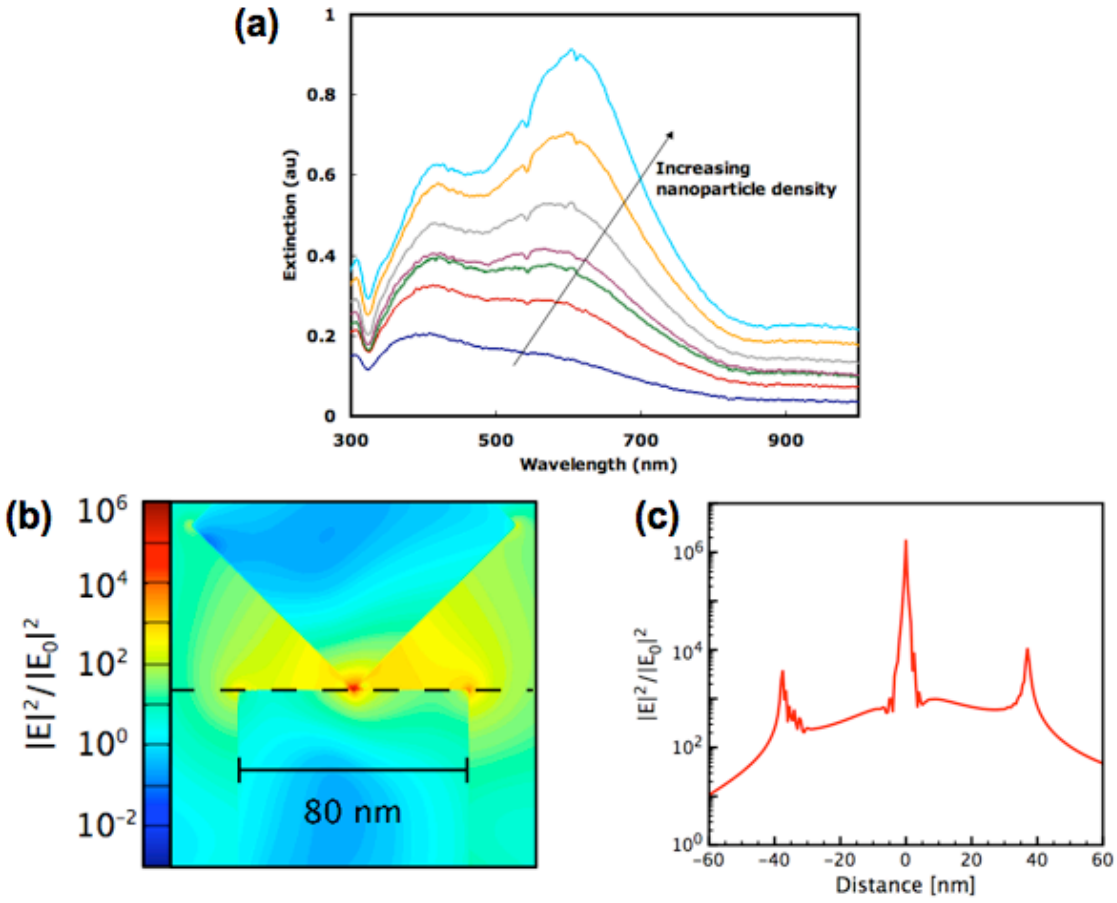

Figure 3.5 Effect of interparticle interactions on SPR. (a) The figure shows experimentally measured, reflection absorption UV-vis spectra of Ag nanocube films of increasing density. (b) The figure shows a contour plot of 2 interacting 80 nm Ag nanoparticles calculated from an FDTD simulation. The particles are separated by 1 nm. (c) The figure shows the electric field strength along the dotted line in Figure 3.5(b).

3.4.2 Surface Plasmon Decay Mechanisms

It has been shown that in an ***inert*** environment excited surface plasmons can decay through two mechanisms: (i) intense radiative scattering of resonant photons (ie. re-emission of stored photons), or (ii) the non-radiative formation of energetic charge carriers, basically electron hole (e^-/h^+), that subsequently decay, and heat the nanostructure. The fraction of plasmons that decay through each of these mechanisms is dependent on the size of the nanoparticle.[8,14,15] Figure 3.6(a) shows the fraction of plasmons that decay through each mechanism, as a function of edge length for cubic Ag nanoparticles. The figures shows that at small sizes ($d < 50$ nm), the majority of excited plasmon decay through the formation and subsequent decay of e^-/h^+ pairs. As the nanoparticles increase in size beyond 50 nm, the plasmons decay primarily through the radiative scattering mechanism, rendering them excellent "nano-antenna". Figure 3.6(b) and (c) show FDTD simulated extinction, scattering and e^-/h^+ production spectra, for 30 and 120 nm Ag nanocubes. The Figures show that at small sizes, e^-/h^+ production dominates the spectra, whereas at larger sizes scattering dominated the extinction spectra.

On the other hand, in reactive environments (i.e., environments where metallic particles can exchange energy with surroundings), the surface plasmons could also interact with adsorbates on the surface of the nanostructure by promoting the transfer of energetic electrons to unoccupied adsorbate states. This can occur either directly through the process of chemical interface damping or indirectly via the decay of plasmons into energetic electrons, followed by the scattering of these electrons off unpopulated adsorbate states.[2] In the plasmon interface damping mechanism it is

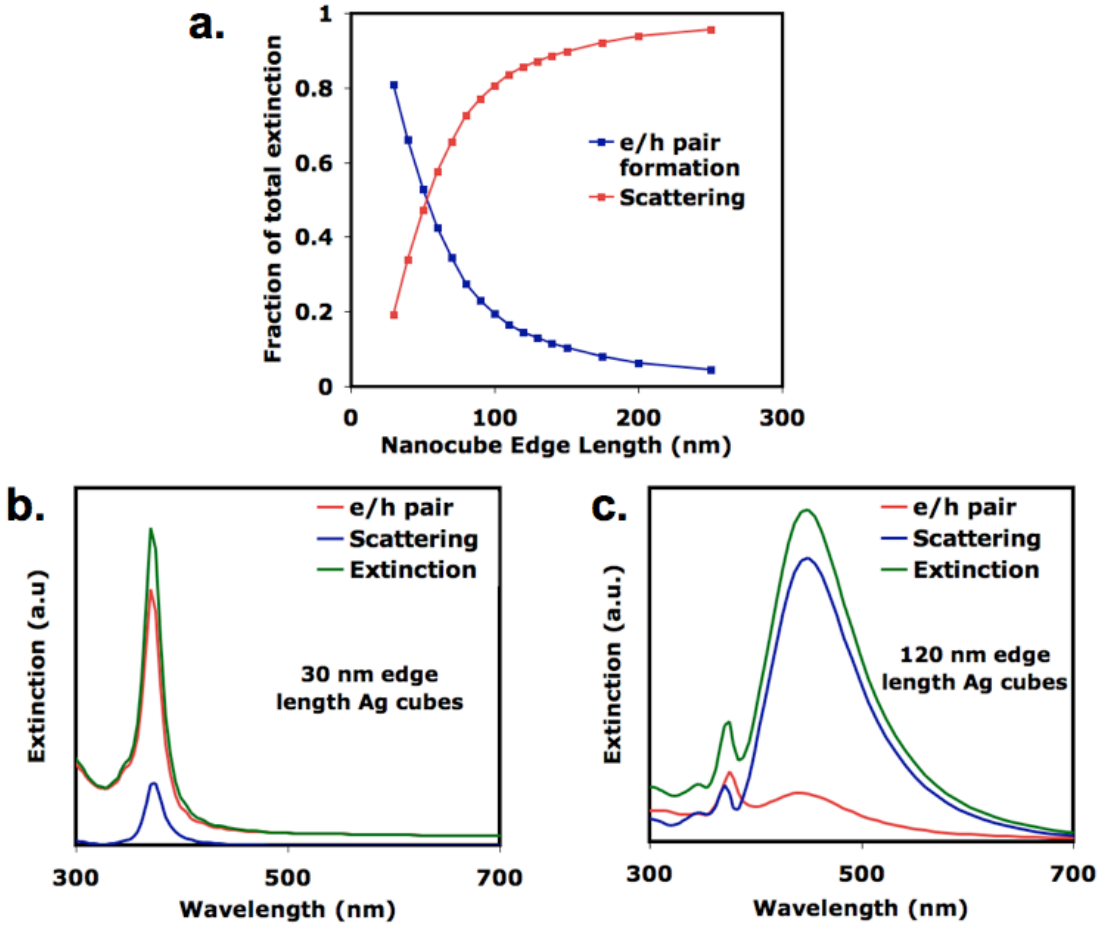

Figure 3.6 Size dependent decay properties of Ag nanoparticles. (a) The figure shows the fraction of plasmons that decay through either scatter or e^-/h^+ formation as a function of Ag nanocube edge length. The results were obtained from FDTD simulations. (b) The figure shows FDTD simulated extinction, scattering and e^-/h^+ pair formation curves from a 30 nm edge length nanocube. (c) The figure shows simulated extinction, scattering and e^-/h^+ pair formation curves from a 120 nm edge length nanocube.

proposed that the oscillating electron density inelastically interacts with adsorbate molecules prior to decaying through either of the above-mentioned mechanisms, thereby reducing the plasmon induced field intensity and reducing the average energy of the plasmons. Alternatively, excited plasmons could decay to produce e^-/h^+ pairs that subsequently are transferred to adsorbates at the nanoparticle surface. The 4 possible mechanism of plasmon decay in a reactive environment are depicted in Figure 3.7. A major focus throughout this dissertation is to explore and understand how excited plasmons can induce photocatalytic reactions. Specific attention is given to developing detailed mechanistic insights into these processes, which allow the design of optimal photocatalytic materials, based on plasmon resonating particles, for various applications.

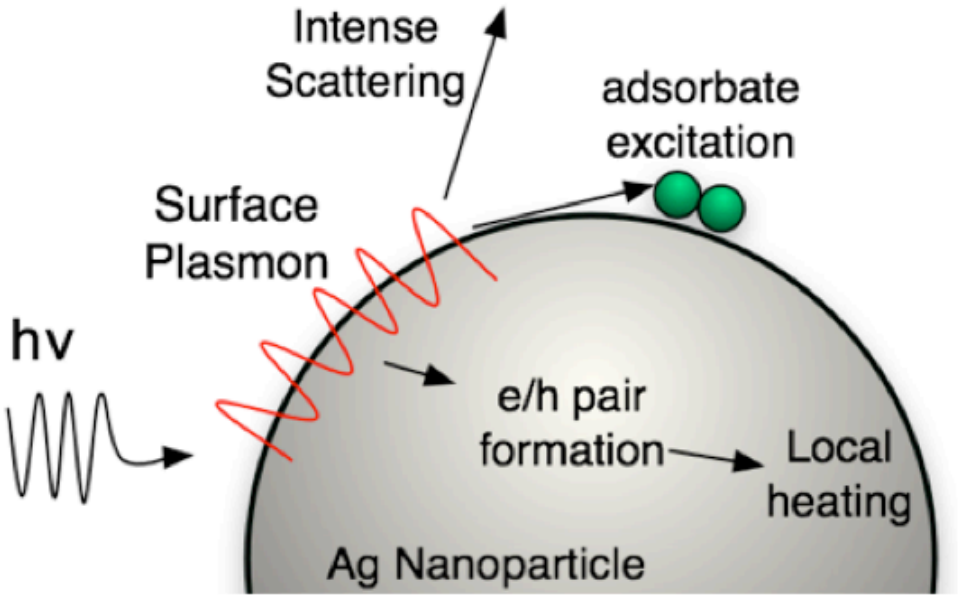

Figure 3.7 The figure shows a schematic of the possible decay routes of excited plasmons.

3.5 Conclusions and Outlook

The ability to control the size and shape of metallic nanoparticle through solution based synthesis approaches, allows for the effective tuning of many characteristics. Specifically, by controlling the size and shape of nanoparticles the concentration of various surface facets can be rationally manipulated. This feature is used in Chapters 4 and 5 to understand how surface structure effects selectivity in the industrially important ethylene epoxidation reaction over Ag nanoparticle catalysts. In addition, the shape and size dependent optical properties of Ag nanoparticles were discussed in this chapter. These materials exhibit unique shape and size dependent interactions with UV and visible photons through the excitation or resonant surface plasmons. It is shown in Chapters 6, 7, and 8 that through the manipulation of these properties it is possible to develop novel photocatalytic materials.

3.6 References

[1] M.A. El-Sayed, *Acc. Chem. Rev.*, **34**, 257, 2001.

[2] K. Watanabe, D. Menzel, N. Nilius, H.-J. Freund, *Chem. Rev.*, **106**, 4301, 2006.

[3] Y. Xia, Y. Xiong, B. Lim, S.E. Skrabalak, *Angew. Chem. Int. Ed.*, **48**, 60, 2009.

[4] K. L. Kelly, E. Coronado, L.L. Zhao, G.C. Schatz, *J. Phys. Chem. B*, **107**, 668, 2003.

[5] D. Uzio, G. Berhault, *Catal. Rev. Sci. Eng.*, **52**, 106, 2010.

[6] P. Christopher, S. Linic, *J. Am. Chem. Soc.,* **130**, 11264, 2008.

[7] P. Christopher, S. Linic, *ChemCatChem,* **2**, 78, 2010.

[8] P. Christopher, D. B. Ingram, S. Linic, *J. Phys. Chem. C*, **114**, 9173, 2010.

[9] S. Linic, P. Christopher, *ChemCatChem*, **2**, 1061, 2010.

[10] P. Christopher, H. Xin, S. Linic, *Nature Chem.,* **3**, 467, 2011.

[11] G.C. Bond, *Surf. Sci.,* **156**, 966, 1985.

[12] R.A. Van Santen, *Acc. Chem. Rev.*, **42**, 57, 2009.

[13] B. Hammer, O.H. Nielsen, J.K. Nosrkov, *Catal. Lett.*, **46**, 31, 1997.

[14] L. Brus, *Acc. Chem. Res.,* **41**, 1742, 2008.

[15] P.K. Jain, X. Huang, I.H. El-Sayed, M.A. El-Sayed, *Acc. Chem. Res.***, 41**, 1578, 2008.

[16] G. Ertl, H.-J. Freund, *Physics Today*, **January**, 32, 1999.

[17] K. Honkala, *et al.*, *Science*, **307**, 555, 2005.

[18] E. Ringe, R.P. Van Duyne, L.D. Marks, *NanoLett.*, DOI: nl2018146, 2011.

[19] T.S. Ahmadi, Z.L.Wang, C.T. Green, A. Henglein, M.A. El-Sayed, *Science,* **272**, 1924, 1996.

[20] Y. Sun, Y. Xia, *Science*, **298**, 2176, 2002.

[21] E. Prodan, C. Radloff, N.J. Halas, P. Nordlander, *Science*, **302**, 419, 2003.

Chapter 4

Ag Nanowires as Selective Ethylene Epoxidation Catalysts

4.1 Summary

The limited selectivity of Ag-based heterogeneous catalysts is one of the major problems associated with the industrially important selective oxidation of ethylene to form ethylene oxide. In this chapter we utilized DFT calculations to examine the effect of Ag surface structure on process selectivity. Based on these calculations, we identified the Ag(100) surface facet as being inherently more selective than the Ag(111) surface facet, which dominates most industrial Ag catalysts synthesized using classical approaches. We utilized synthesis approaches recently developed in the nanotechnology community to synthesize Ag nanowires dominated by the Ag(100) facet. The results of the DFT calculations were supported by reactor studies that showed Ag nanowires, dominated by the (100) surface facet, were significantly more selective for ethylene epoxidation compared to an Ag catalyst dominated by the (111) facet. The results showed that recent advances in synthetic approaches, combined with DFT calculations, might provide a versatile platform for the design of highly selective catalysts.

4.2 Introduction

Controlling selectivity in heterogeneous catalysis is critical for the design of environmentally friendly catalytic processes that minimize the production of undesired byproducts and operate with high-energy efficiency.[1,2] In this chapter we show an example where Density Functional Theory (DFT) calculations have been utilized along with recently developed solution-based synthetic chemistry approaches to design heterogeneous silver catalysts that are more selective in partial oxidation of ethylene to form ethylene oxide (EO) than conventional Ag catalysts. Our studies suggest that recent advances in synthetic chemistry, which have laid the groundwork for the controlled synthesis of uniform nano-structures with well defined surface facets,[3,4] might provide a critical platform for the design of highly selective heterogeneous catalytic materials.[5,6,7]

The partial oxidation of ethylene to form EO is the largest heterogeneous catalytic process where selectivity is the crucial descriptor of catalytic performance.[8] World production of EO was valued at ~$ 20 billion in 2008, and market analysis predicts continued 5% growth per year over the next decade.[9] Over 75% of EO produced is directly used to synthesize ethylene glycol, which is mainly used to make polyester and automotive antifreeze. In addition, EO is used to make many chemicals and products including ethanolamines, detergents, emulsifiers, among many others.[8,9]

Ethylene epoxidation is carried out by flowing ethylene and oxygen over a heterogeneous Ag-based catalyst at temperatures between 500-550 K.[10] Ethylene and oxygen partial pressures range from 3-20 % in the industrial processes.[11] The major by-products in the processes are CO_2 and H_2O, which result from complete combustion of ethylene. It has been found that Ag is the only heterogeneous metal catalyst that

demonstrates reasonable selectivity towards EO. Optimized pure Ag catalytsts for ethylene epoxidation are characterized by large spherical Ag particles (>100 nm diameter) supported on very low surface area (<5 m^2/g) alpha-alumina monolith supports and typically achieve selectivity towards EO of 40-50%.[12,13] Optimized Ag-based catalysts are promoted by small amounts of cesium, added to the catalyst during synthesis and chlorine, which is continuously added in the gas phase feed stream using ppm levels of compounds such as 1,2-dichloroethane.[14,15] The effects of these promoters on EO selectivity are generally additive and allow selectivity to EO of ~80%. Further empirical studies have found that Rhenium can act to further promote the selectivity to ~90%.[16]

Classically, the ethylene epoxidation process has been thought of in terms of the triangular reaction network shown in Figure 4.1(a).[12] In this picture, ethylene and oxygen react to form either EO or combustion products. In addition, EO, which is a highly unstable molecule, can further react to form combustion products. Although, this macroscopic picture proved useful for empirically relating experimental measured selectivity and catalyst compositions, it fails to provide a detailed molecule mechanism that allows rational manipulation of catalyst composition and process operation.

Recent DFT calculations, surface science experiments, and kinetic isotope measurements have suggested that the selectivity to EO on Ag is controlled by a reaction network of competing elementary pathways where a surface oxametallacycle (OMC) intermediate undergoes isomerization reactions on Ag to form the selective product, EO, or acetaldehyde (AC), which subsequently combusts on the surface.[17,18,19,20,21] The surface OMC is formed through the adsorption of ethylene to an adsorbed O atom on the Ag surface. It has been shown that on the Ag(111) surface the activation barriers for these

(a) Triangular reaction network

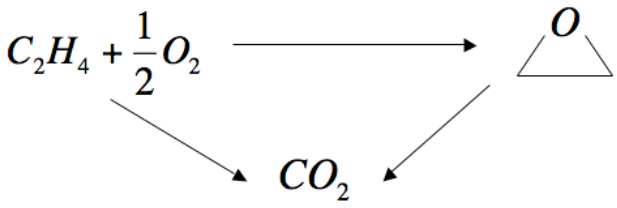

(b) Selectivity controlled by oxametallacycle intermediate

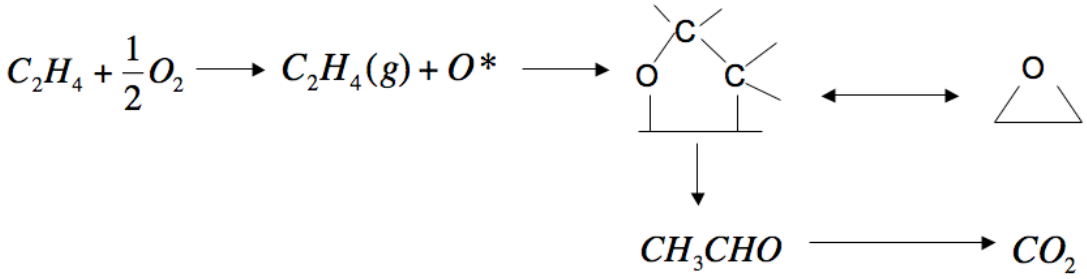

Figure 4.1 Proposed ethylene epoxidation mechanisms. (a) A classical view of selectivity control in ethylene epoxidation through a triangular reaction network. (b) A recently proposed mechanism for the control of ethylene epoxidation through a common oxametallacyle intermediate. The oxametallacycle is formed through to addition of gas phase ethylene to an adsorbed oxygen atom. The oxametallacycle then isomerizes on the surface to form either EO or AC. AC further reacts on the surface to form combustion products.

elementary steps are comparable to each other, ultimately limiting the selectivity to EO on this surface.[18] This mechanism is depicted in Figure 4.1(b).

In the pioneering work of Linic and Barteau, it was shown that the OMC intermediate could be synthesized on the Ag(111) surface under UHV conditions.[17] By exposing the Ag(111) single crystal to EO at 250 K, sufficient thermal energy is provided to drive the ring opening reaction, which forms the OMC. The exposure temperature is crucial, because enough thermal energy is provided to open the epoxide ring, but because the ring opening is exothermic, there is not sufficient energy to desorb the oxametallacycle. Heating of the OMC covered Ag(111) single crystal results in the ring closure of the OMC to re-form EO. The structure of the OMC was studied using DFT calculations to identify the vibrational and electronic fingerprint of the intermediate.[17,21] Comparison of the calculated vibrational and electronic properties to those measured by high resolution electron energy loss spectroscopy and high resolution x-ray photoelectron spectroscopy provide convincing evidence that the OMC was identified and that the geometry is very similar to that proposed by the calculations.

DFT calculations were further used to identify other possible isomerization reactions of the OMC on the Ag surface that have similar energetics to the formation of EO. The formation of AC, through the 1,2 hydrogen transfer reaction, was identified as energetically almost identical to EO formation.[18] Previous work has shown that AC readily oxidized on oxygen covered Ag surfaces.[20] This indicates that the formation of AC followed by complete combustion may provide and understanding of how the selectivity to EO on Ag surfaces is controlled. By comparing energetics of the EO and AC formation reactions from the OMC intermediates, selectivity to EO of about 50% is

estimated. This is in excellent agreement with selectivity measurements performed over Ag(111) single crystal surfaces.[22] The limited selectivity of the Ag(111) surface has practical implications since catalytic particles that are synthesized using standard impregnations strategies are dominated by the Ag(111) facet.[23] This framework provides and excellent understanding of why selectivity to EO is limited to 50% on monometallic spherical Ag catalysts with 100 nm diameter.

One of the most convincing pieces of evidence for the control of ethylene epoxidation selectivity through the OMC intermediate is the ability of the mechanism to quantitatively capture the change in selectivity that is experimentally observed due to isotopic labeling of ethylene.[24] It has been observed that when the reactant feed is switched from C_2H_4 to C_2D_4 the selectivity was increased by about 25%. The enhancement in EO selectivity can be explained by a primary kinetic isotope effect increasing the activation barrier associated with AC formation. The formation of AC requires a breaking of the C-H bond in the first hydrogen, followed by a hydrogen transfer from the first to the second carbon. On the other hand, the formation of EO from the OMC does not require any bond breaking or re-arrangements associated with hydrogen. The change in free energy due to isotopic labeling of ethylene can quantitatively account for the change activation barrier for AC formation required to explain the change in selectivity.[18] In concert with the agreement between measured and calculated vibrational and electron fingerprints of the OMC, this provides excellent evidence that selectivity in the ethylene epoxidation reaction over Ag is significantly controlled by the parallel OMC isomerization reactions.

In this chapter we utilize the general framework of the OMC mechanism to examine the affect of Ag surface structure on the selectivity of the ethylene epoxidation reaction. We identify an inherently more selective surface than Ag(111) and use this finiding to guide the synthesis of Ag nanoparticles with targeted surface structures. Our results show (a) an example where DFT calculations have guided the design of novel catalytic materials with superior selectivity, and (b) that the size and shape of catalytic nanoparticles may provide an excellent platform that can be used to control product selectivity.[5]

4.3 Theoretical Methods

DFT calculations were performed using the Dacapo total energy plane wave code [https://wiki.fysik.dtu.dk/dacapo]. Calculation parameters were chosen to ensure consistency with respect to surface coverage and k-point sampling between calculations on the Ag(111) and Ag(100) surfaces. These calculation parameters yielded adsorption energies of atomic oxygen and oxametallacycle consistent with those reported previously.[18,25,26]

The Ag(100) and Ag(111) surfaces were modeled as a $2\sqrt{2}$ x $2\sqrt{2}$ supercell and a 3x3 supercell with 4 layers and 3x3x1 Monkhorst-Pack k-point sampling. The theoretical Ag lattice constant of 4.14 Å was used in all calculations. The slabs were separated in z-direction with 6 layers of vacuum. The top 2 layers of the slab and the adsorbates were allowed to completely relax. The forces were minimized to 0.1 eV/Å. The GGA-PW91 functional was used to describe the exchange correlation energy and potential.[27] The PW91 density was calculated self-consistently by iterative diagonalization of the Kohn-

Sham Hamiltonian and Pulay mixing of the electronic density.[28] An electronic temperature (k_bT) of 0.1 was used during calculations and all energies were extrapolated to 0 K. The plane wave basis, used to describe the Kohn-Sham one-electron states was cut off at 350 eV. Vanderbilt pseudo-potentials were utilized to describe the core electrons.[29]

The minimum energy pathways for the transformation of the oxametallacycle (OMC) to ethylene oxide (EO) and acetaldehyde (AC) were obtained using the climbing image nudged elastic band (CI-NEB) algorithm.[30] The inputs in these calculations are the initial state (OMC) and final state (EO and AC) geometries in their lowest respective energy configurations. Forces along the reaction pathway were minimized to 0.1 eV/Å .

The bond decomposition calculations were performed removing a constituent group from the OMC (either OCH_3 or CH_3) and saturating the broken C-C bond with a hydrogen atom. The hydrogen atom was then allowed to fully relax while freezing all other atoms in the configurations consistent with the oxametallacycle geometry.

4.4 Experimental Methods

4.4.1 Ag Nanowire Synthesis

Silver nanowires were synthesized using the seedless polyol process[31] where $AgNO_3$ (99.99%, Sigma) is reduced in ethylene glycol (EG) (99.8% anhydrous, Sigma) heated to 160ºC in the presence of poly(vinyl pyrrolidone) (MW = 40,000; Sigma). In the synthesis of 75 nm wires, 5 mL EG was heated to 160ºC and refluxed for 1 hr in a three-neck round bottom flask equipped with a magnetic stir bar and condenser and submerged in an oil bath to allow homogeneous heating. A two-channel syringe pump

was used to simultaneously introduce 3 mL of $AgNO_3$ solution (0.1 M in EG) and 3 mL of PVP solution (0.6 M in EG) at a rate of 0.375 mL/min to the heated solution. Cleanliness of all reagents, glassware and syringes was crucial. Once the reagents had been introduced, the solution was allowed to reflux under vigorous stirring at 160ºC for 1 hr. To increase the diameter of the nanowires, the molar ratio between PVP and $AgNO_3$ was reduced to 1.5:1 and the addition rate was slowed to 0.2 mL/min. In both syntheses the solution turned yellow immediately after the first drops of $AgNO_3$ was introduced to the heated EG, followed by a reddish color at about 5-10 minutes then the solution gradually turned grey and opaque indicating the beginning of nanowire growth. The final solution was turbid and grey.

The nanowire solution was then diluted 10 fold in acetone and centrifuged at 2500 RPM for 20 minutes to separate the wires from the ethylene glycol. The wires were then separated from spherical particles by dispersing the concentrated solution in de-ionized water and centrifuging at 2000 RPM for 20 minutes, the supernatant (yellowish color) containing nanoparticles was then removed by pipette. This procedure was then repeated until the supernatant became colorless.

The nanowire catalysts were prepared using a concentrated solution of nanowires in ethanol as the impregnation solution. The α-Al_2O_3 foam monolith was then contacted with the impregnation solution and was allowed to dry at 70ºC in air. The weight loadings were estimated knowing the concentration of nanowires in solution and verified by weighing the support before and after impregnation.

4.4.2 Standard Catalyst Synthesis

A standard impregnation method was used to synthesize particles dominated by the Ag(111) surface.[32] A pre-cleaned monolith was contacted with a silver nitrate ($AgNO_3$) solution with a small excess of Ag compared to the desired loading, ~13 wt%. The monolith was then dried at 80 ^oC under air. The weight loading was also verified by weighing the monolith before impregnation and after the catalyst had been reduced to form Ag particles. The final weight loading was 12.5%. The catalysts were then reduced at 300 ^oC under H_2 atmosphere for three hours. The particles were spherical with sizes on the order of 1-2 μm as measured by SEM.

4.4.3 Scanning Electron Microscopy

Scanning Electron Micrographs were obtained using FEI Nova 200 Nanolab. Ag nanoparticles were deposited from ethanol solution onto pre-cleaned Si wafers for imaging. For the standard catalyst imaging, the monlith was cross-sectioned and directly imaged. Accelerating voltage was 5kV for all images.

4.4.4 X-Ray Diffraction

X-Ray Diffraction (XRD) spectra were collected using a Cu-Kα on a Philips XRG5000 3kW x-ray generator with a Rigaku camera and a crystal alignment stage. Peaks were identified using Jade v.7 software.

4.4.5 UV-visible Absorbance Spectroscopy

UV-vis absorbance spectroscopy was performed using an 8453 UV-vis Chem Station spectrophotometer from Agilent Technologies. Samples were prepared by

diluting a purified nanowire solution 100X in de-ionized water. Concentrations were adjusted such that all signals would be on the same scale.

4.4.6 Reactor Studies

All reactor studies were performed in a horizontally oriented tube reactor operated isothermally at 237ºC and atmospheric pressure. A 1.0 g α-Al_2O_3 foam monolith support (99.5%, Vesuvius Hi-Tech Ceramics) with surface area of .3 m^2/g was used in all experiments. The monolith was secured in a quartz reactor tube using quartz wool. Total inlet flow rate was kept constant at 100 standard cubic centimeters per minute (sccm); gas flow-rates were controlled using gas flow controllers and all gases used were the highest purity available. All catalysts were allowed to run at 10 sccm O_2, 10 sccm C_2H_4 and 80 sccm N_2 until they reached steady state. The O_2/C_2H_4 ratio was then varied by increasing the O_2 flowrate, decreasing the N_2 carrier gas flowrate while holding the C_2H_4 flowrate constant. Product gases were analyzed in line with a Varian gas chromatograph (Varian CP 3800) equipped with TCD and FID detectors.

4.5 Results and Discussion

4.5.1 DFT Calculations

As discussed in the introduction, DFT calculations and a wealth of surface science experiments indicate that selectivity in the epoxidation of ethylene over Ag surfaces is controlled by the parallel reaction network involving the isomerization of the oxametallacycle intermediate to either EO or AC. We have used DFT calculations, within the nudged elastic band framework, to calculate the geometric features and

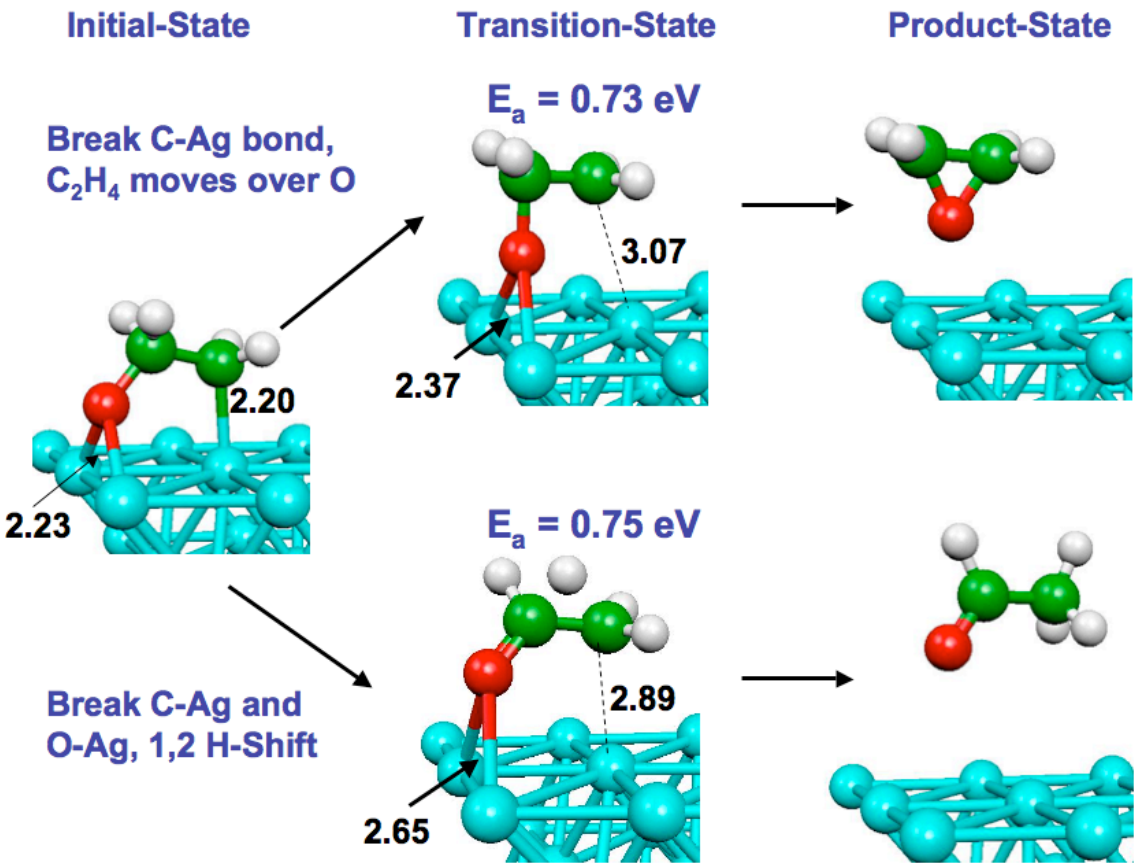

Figure 4.2 DFT calculated reaction pathways over Ag(111). The figure shows the initial state (oxametallacycle), transition-states and final states (EO and AC) in the parallel reaction pathway. The figure shows similar activation barriers for the formation of both products.

energetics association with the competing reactions over Ag(111) and Ag(100) surfaces. The Ag(111) surface is the most studied single crystal plane of Ag for ethylene epoxidation and is the major surface facet exposed on industrial Ag catalysts, synthesized through standard approaches.[13,22] In Figure 4.2 the calculated pathways for the formation of EO and AC from the OMC on Ag(111) are shown. The figure shows the structure of the OMC intermediate, the transition states and the final configuration of the products. The formation of EO is characterized by the breaking of the Ag-C bond in the OMC structure, followed by ring closure to form EO. The formation of AC is characterized by the extension of both the Ag-O and Ag-C bonds in the OMC to allow for the 1,2 hydrogen transfer; resulting in the formation of AC. The energy barrier associated with the formation of EO from the OMC is 0.73 eV, whereas the formation of AC requires 0.75 eV. The equivalence of these activation barriers, as well as the magnitude, are in-line with previous calculations and the limited selectivity of the Ag(111) surface.[18]

Identical calculations were performed on the Ag(100) surface to understand how variations in Ag surface structure affect selectivity. The Ag(100) surface is the second most thermodynamically stable surface facet of Ag. The (100) surface is characterized by a cubic structure, as compared the hexagonal packing that characterizes the (111) surface, see Figure 4.3. Figure 4.3 shows the DFT calculated potential energy surfaces for the formation of EO and AC on the Ag (111) and (100) surface. There are two major difference in the energetics when comparing the (111) and (100) surfaces. First, the calculated activation barriers for both EO and AC formation are increased on the (100) surface, with respect to the (111) surface. This can be understood in terms of the reduced coordination number of surface atoms in the (100) surface compared to the (111) surface,

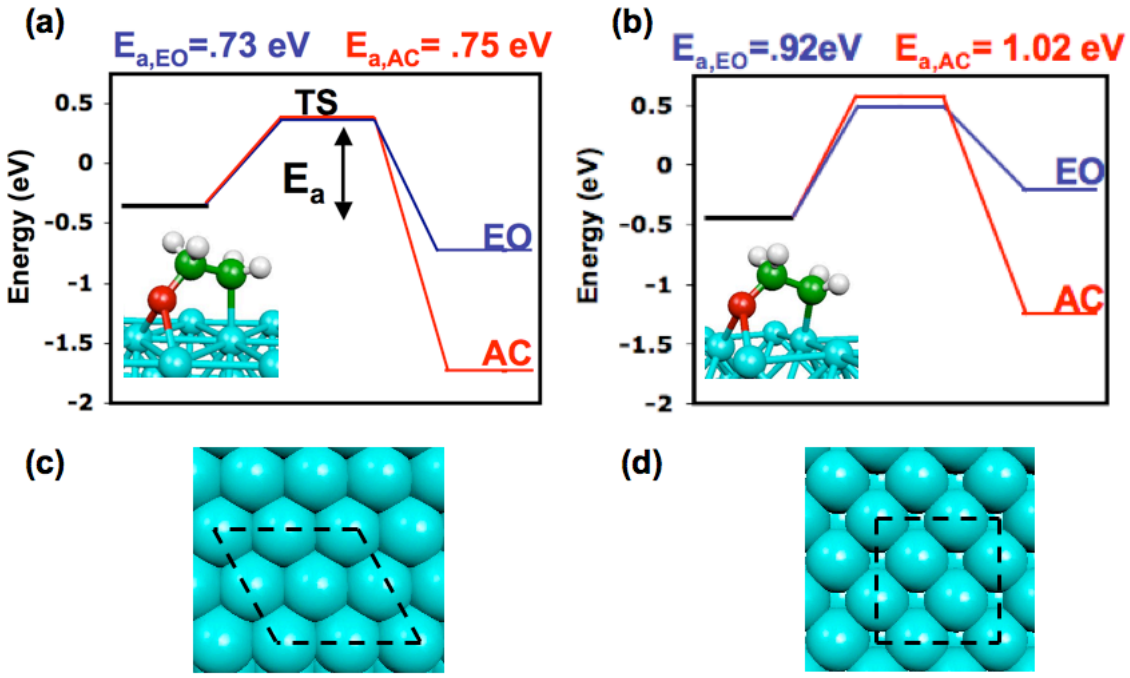

Figure 4.3 DFT Comparison of Ag (111) and Ag (100) for selective ethylene epoxidation. (a) Potential energy surface for the formation of EO and AC from the OMC on Ag(111). (b) Potential energy surface for the formation of EO and AC from the OMC on Ag(100). (c) Model system used in the DFT calculations for the Ag(111) surface. (d) Model systems used in the DFT calculations for the Ag(100) surface.

which is well-known to be correlated to the binding strength of adsorbates on metallic surfaces.[33,34] Secondly, Figure 4.3 shows that the difference in the activation barriers associated with the formation of AC and EO is by ~ 0.1 eV larger on Ag(100) than on Ag(111). This suggests that the (100) surface should be intrinsically more selective to EO that the (111) surface, because the activation barrier to form EO is significantly lower than the barrier required to form AC. In general, the calculations shown in Figures 4.2 and 4.3 show that, although the (100) surface exhibits higher activation barriers for product formation, this surface should be inherently more selectivity than the (111) surface, which dominates industrial catalysts.

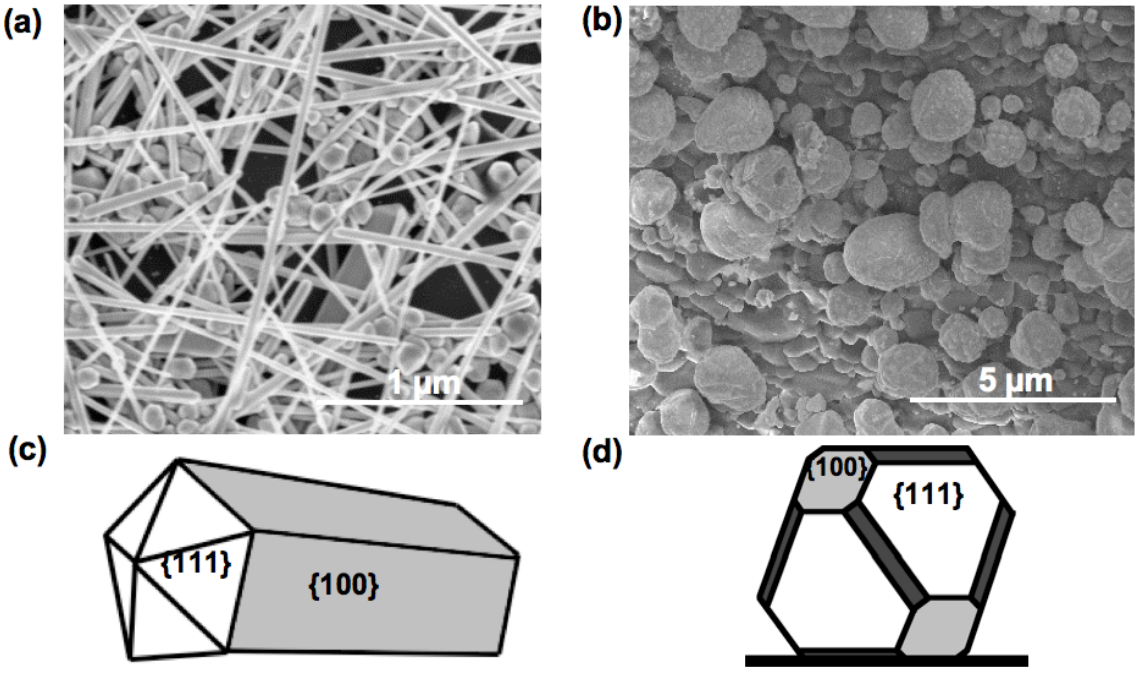

Figure 4.4 Structural comparison of nanowires and spherical particles. (a) SEM images of the 75 nm diameter Ag nanowires. (b) SEM image of the spherical catalytic particles synthesized using impregnation approach. (c) Structural model of the pentagonal Ag nanowires. (d) Structural model of the spherical, Wulff construction particles.

4.5.2 Catalyst Characterization

To test the DFT calculated enhanced EO selectivity of the (100) surface compared to the (111) surface, we have synthesized two different monometallic Ag catalysts supported on alpha-Al_2O_3: (i) Ag nanowires dominated by the (100) surface facet and (ii) conventional Ag catalyst dominated by the (111) facet. A standard incipient wetness technique was used to synthesize Ag particles with a majority of Ag(111) surface planes. The self seeding polyol synthesis was used to synthesize pentagonal Ag nanowires grown from multiply twinned particles which are dominated by the Ag(100) surface.[31] See Figure 4.4 for SEM images and structural models of the two catalytic structures.

Ag nanowires synthesized using the self-seeding polyol process have been characterized previously in electron diffraction experiments showing that the wires are terminated on all sides by the (100) planes.[35,36] The (100) terminations of Ag nanowires was also verified in scanning tunneling microscope measurements.[37] This is further supported by the results of X-ray diffraction (XRD) studies in Figure 4.5(a) indicating that the Ag nanowire catalysts have reduced quantities of high-index Miller planes as compared to the impregnation catalyst, i.e., the growth of nano-wires is in the longitudinal direction, in the (110) direction. We have also established that the diameter of nanowires can be systematically manipulated by controlling the concentration and the rate of addition of the Ag salt and the stabilizer molecules, this is discussed in detail in Chapter 2. Figure 4.5(b) shows UV-vis absorbance spectra for two different nanowire solutions. The measured spectra are a consequence of the excitation of surface plasmons and are characteristic of nanowires with approximate diameters of 75 and 175 nm.[38] The effect particle size and shape of Ag particles on the interaction with UV and visible

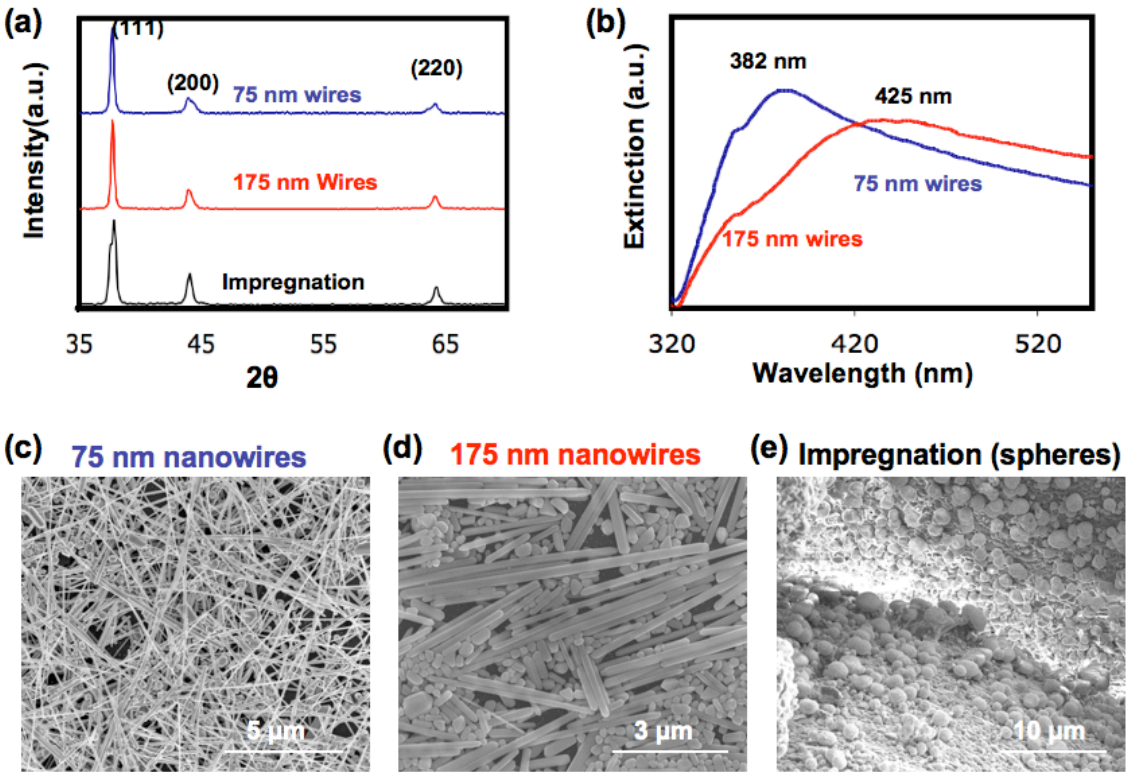

Figure 4.5 Characterizing nanostructured catalysts. (a) The figure shows XRD spectra associated with the 3 catalysts. The spectra are normalized such that the intensity of the (111) peak is constant. (b) Transmission UV-vis spectra of the 75 and 175 nm Ag nanowires in ethanol solutions. (c) SEM image of the 75 nm nanowires, (d) 175 nm nanowires, and (e) impregnation catalyst.

photons is discussed in detail in chapter 3. SEM images of the 3 catalysts tested in this chapter are shown in Figure 4.5(c)-(e). The SEM images were used to measure the average particle sizes, where a good agreement with the UV-vis measurements was found. The impregnation catalyst contained spherical particles with average diameter of over 1μm diameter.

4.5.3 Reactor Studies

The particle and nanowire catalysts were tested in the ethylene epoxidation reaction in a continuous flow reactor at constant total flow rate, differential conversion, temperature T = 510 K, and atmospheric pressure. Figure 4.6 shows the measured selectivity to EO, defined as the amount of EO produced divided by the amount of ethylene consumed, as a function of oxygen to ethylene feed ratio. The conversion for different catalysts, defined as the amount of ethylene consumed divided by the amount of ethylene entering the reactor, was kept constant by adjusting the mass of active Ag material. The catalysts were on stream for 5-7 days with stable selectivity and conversion. The measurements in Figure 4.6 show that the nanowire catalysts are more selective than the particle catalyst over a wide range of external conditions. For example, the highest measured selectivity for a nanowire catalyst was 65 %, while the Ag particle catalysts reached the selectivity of 47 %. The measured selectivity for the spherical impregnation catalyst, between 37-47%, is in agreement with previous measurements of the Ag(111) surface and on large Ag nanoparticle catalysts. It is important to point out that the measured turn over frequencies (TOF) per surface site for nanowire catalysts were similar to the TOF for the particle catalyst. However, since the nanowires had larger

surface to volume ratio that the particles, the EO yield on per catalyst mass basis was significantly higher for the nanowire catalyst. The results in Figure 4.6 also show that the selectivity to EO of the nanowire catalyst increased as the average diameter of Ag nanowires was increased. It is believed that this enhancement in the EO selectivity is a result of an increased ratio of well-coordinated Ag sites with respect to under-coordinated step and kink sites for larger nanowires; this is discussed in more detail in Chapter 5.

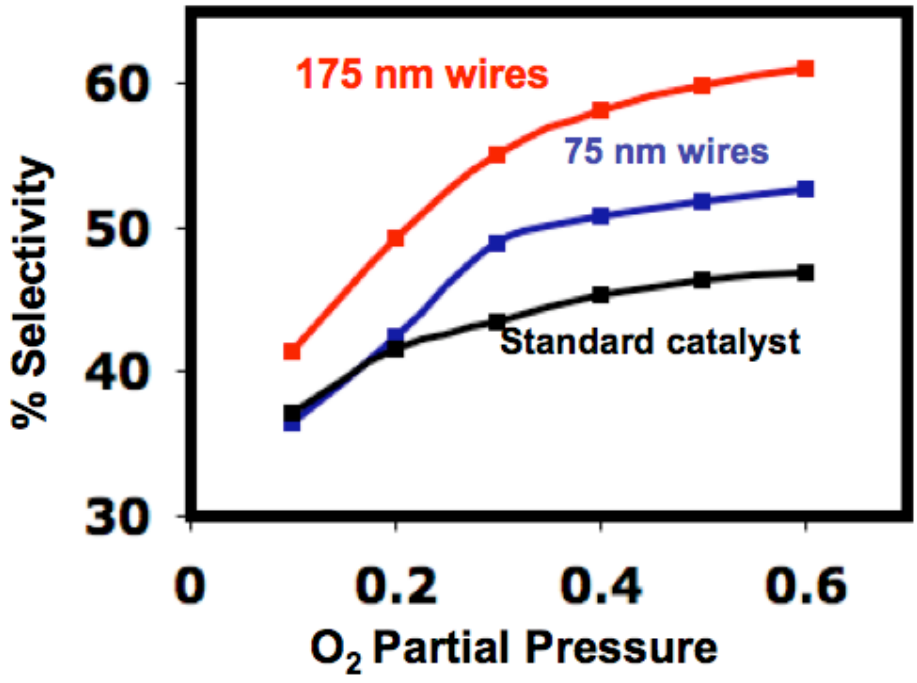

Figure 4.6 EO Selectivity measured as a function of O_2 partial pressure for the three catalysts. All reactions were carried out at differential conditions, < 5%, and a temperature of 510 K. The partial pressure of the carrier gas, N_2 was varied to compensate for changes in O_2 partial pressure, such that the total flow rate was constant at 100 sccm for all experiments.

4.5.4 Why is Ag(100) More Selective Than Ag(111)?

Because all experimental conditions that affect EO selectivity (temperature, partial pressure, conversion, support materials) were kept constant in these studies, we postulated that the underlying mechanism controlling the difference in selectivity is the dominant surface facet on the tested catalysts. To understand the origin of the selectivity increase for the nanowire (100) catalysts, the calculated geometries of the transition states (TS's) for the formation of AC and EO were analyzed, see Figure 4.2. The analysis showed that on both surfaces, Ag(111) and Ag(100), the TS leading to AC requires significant elongation of the O-Ag and C-Ag bonds in the oxametallacycle. On the other hand, for the EO TS, the O-Ag bond distance in the oxametallacycle is only slightly changed while the C-Ag bond is substantially elongated.[39] The effect of changing the surface structure from (111) to (100) on the energetics of these processes can be understood at a simple level, simply by considering that the adsorption energy of O on Ag(100) is ~0.3 eV more exothermic than on Ag(111). This means that the formation of AC, which requires a breaking of the Ag-O bond, will be affected to a large extent than EO formation, which does not require the Ag-O bond breaking, when moving to the more reactive Ag(100) surface.

We have analyzed the underlying mechanism of the selectivity difference by calculating the adsorption energies for two functional groups, OCH_3 and CH_3, that form the surface oxametallacycle on Ag(111) and (100).[39] Using this approach we can analyze the effect of surface structure on the strength of the interaction between each moiety involved in the isomerization processes and the Ag surfaces. The analysis showed that the adsorption energy of the OCH_3 fragment is by 0.38 eV more exothermic on Ag(100)

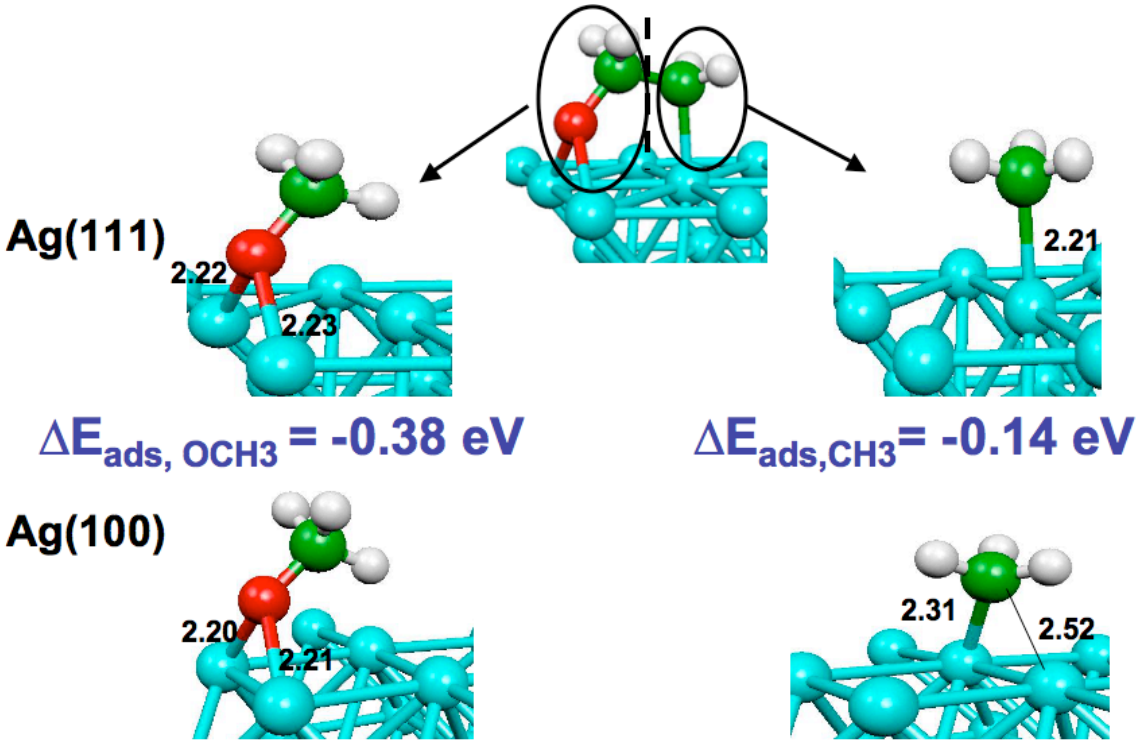

Figure 4.7 The figure shows the results of the bond decomposition calculations. On the left side the adsorption of OCH_3 is compared on the Ag (111) and (100) surfaces. On the right side the adsorption of CH_3 is compared on the two surfaces. See the text for details of the calculations and adsorbate geometries.

compared to Ag(111), indicating that it is energetically more demanding to elongate the O-Ag bond on Ag(100) than on Ag(111). The adsorption of the CH_3 group is more exothermic on Ag(100) by only 0.14 eV, see Figure 4.7. This analysis suggests that the strong difference in the Ag-O interaction, compared to the Ag-C interaction, when comparing the Ag surfaces is the underlying mechanism that allows for the higher selectivity on the (100) surface as compared to the (111) surface.

4.6 Conclusions and Outlook

In the context of results presented herein it is important to revisit the concept of structure sensitivity in ethylene epoxidation on Ag and generally in heterogeneous catalysis. Structure sensitivity has classically been defined in terms of the variation in turnover frequencies (TOF) as a function of the size of catalytic particles. The reactions for which there is a small change in TOF as the average size of active catalytic particles is changed are termed structure insensitive.[40,41] It has been shown previously that for varying diameter of conventional Ag particle catalysts, ethylene epoxidation is structure insensitive.[12] The results presented in this chapter suggest that TOF's for ethylene epoxidation on Ag are similar for the nanowire and particle catalysts, i.e., relative to the definition of structure sensitivity; the reaction is structure insensitive irrespective of the shape of active catalytic structures. We note that this does not mean that the activation barriers for individual elementary steps are not affected by Ag surface structure, but rather it suggests that complex interplay of the elementary steps yields macroscopic TOF's that are similar for different Ag surfaces. The concept of structure sensitivity as defined above reflects only on the TOF's (i.e. the rate of ethylene consumption). More

importantly, our results show that the selectivity to EO is affected significantly by the nature of the dominant Ag surface facet. This would suggest that this reaction is highly structure sensitive with respect to the selectivity to EO. The structure sensitivity of the selectivity to EO is a consequence of significantly different activation barriers associated with the isomerization of the OMC intermediate to form EO and AC on Ag(111) and Ag(100).

In conclusion, in this chapter we show that the Ag nanowire catalysts exhibit higher selectivity to EO that conventional particle catalysts in the ethylene epoxidation reaction. The higher selectivity of the nanowire catalysts was attributed to a higher concentration of the Ag(100) surface facets in the nanowire catalysts compared to the particle catalysts. DFT calculations showed that the transformation of the surface oxametallacycle intermediate to form the selective product, EO, is more favorable on the Ag(100) than on Ag(111). The studies showed that recent advances in the controlled synthesis of uniform nanostructures with well-defined surface facets might provide an important platform for the design of highly selective heterogeneous catalysts. Finally, we also showed that the ethylene epoxidation reaction is highly structure sensitive with respect to selectivity.

4.7 References

[1] G.A. Somorjai, R.M. Rioux, *Catal. Today*, **100**, 201, 2005.

[2] H.-J. Freund, *Top. in Catal.*, **48**, 137, 2008.

[3] Y. Sun, Y. Xia, *Science*, **298**, 2176, 2002.

[4] J. Chen, T. Herricks, Y. Xia, *Angew. Chem., Int. Ed.,* **44**, 2589, 2005.

[5] P. Christopher, S. Linic, *J. Am. Chem. Soc*, **130**, 11264, 2008.

[6] N. Tian, Z. Zhou, S. Sun, Y. Ding, Z.L. Wang, *Science,* **316**,732, 2007.

[7] R.J. Chimentao, I. Kirm, F. Medina, X. Rodriguez, Y. Cesteros, P. Salagre, J.E. Sueiras, *Chem. Commun.*, **7**, 846, 2004.

[8] S. Linic, M.A. Barteau, "Heteroegenous catalysis of alkene epoxidation", Chapter 14.11.6 in *Handbook of Heterogeneous Catalysis*, 2nd edition, Ertl, G., Knozinger, H., Schuth, F., Weitkamp, J. (eds.), Wiley-VCH, 2007.

[9] ICIS News, *Ethylene Oxide (EO) Uses and Market Data*, (ICIS Publication May 2008; http://www.icis.com/v2/chemicals/9075772/ethylene-oxide/uses.html). [The easiest access to this source is by Internet]

[10] K. Weissermel, H.-J. Arpe, *Industrial Organic Chemistry, 2nd Ed.*, VCH, Weinheim, Germany, **1993**, p. 264-272.

[11] F. Ullman, *Encyclopedia of Industrial Chemistry*, 5th, VCH: Deerfield Beach, FL, USA, **1985**.

[12] D.J. Sajkowski, M. Boudart, *Catal. Rev. Sci. Eng.*, **29**, 325, 1987.

[13] X.E. Verykios, F.P. Stien, W.R. Coughlin, *J. Catal.*, **66**, 386, 1980.

[14] J. G. Serafin, A. C. Liu, S. R. Seyedmonir, *J. Mol. Catal.,* **131**, 157, 1998.

[15] R. A. van Santen, H. P. C. Kuipers, *Adv. Catal.,* **35**, 265, 1987.

[16] R. A. Kemp, US Patent 5, 663, 385, assigned to Shell Oil, 2005.

[17] S. Linic, M.A. Barteau, *J. Am. Chem. Soc.,* **125**, 4034, 2002.

[18] S. Linic, M. A. Barteau, *J. Am. Chem. Soc.* **125**, 4034, 2003.

[19] S. Linic, M.A. Barteau, *J. Catal.*, **214**, 200, 2003.

[20] R. J. Madix, *Science*, ***233***, 1159, 1986.

[21] S. Linic, M. A. Barteau, *Angew. Chem. Intl. Ed*., ***43***, 2918, 2004.

[22] C.T. Campbell *J. Catal.* **94**, 436, 1985.

[23] J. Couves, M. Atkins, M. Hague. B.H. Sakakini, K.C. Waugh, *Catal. Lett.*, **99**, 45, 2005.

[24] N. W. Cant, W. K. Hall, *J. Catal.*, ***52***, 81, 1978.

[25] J. Greeley, M. Mavrikakis, *J. Phys. Chem. C*, **111**, 7992, 2007.

[26] A. Kokalj, P. Gava, S. Gironcoli, S. Baroni, *J. Phys. Chem. C,* **112**, 1019, 2008.

[27] J.P. Perdew, *et. al., Phys. Rev. B*, **46**, 6671, 1992.

[28] G. Kresse, J. Furthmuller, *Comput. Mater. Sci.,* **6**, 15, 1996.

[29] D. Vanderbilt, *Phys. Rev. B*, **41**, 7892, 1990.

[30] G. Hankelman, B.P. Uberuaga, H. Jonsson, *J. Chem. Phys.,* **113**, 9901, 2000.

[31] Y. Sun, Y. Xia, *Adv. Mater.,* **14**, 833, 2002.

[32] J.T. Jankowiak, M.A. Barteau, *J. Catal.,* **236**, 366, 2005.

[33] B. Hammer, J.K. Norskov, *Nature,* **376**, 238, 1995.

[34] T. Bligaard, J.K. Norskov, S Dahl, J. Matthiesen, C.H. Christensen, J. Sehested, *J. Catal*, **224**, 206, 2004.

[35] Y. Sun, B. Mayers, T. Herricks, Y. Xia, *Nano Lett.*, **3**, 955, 2003.

[36] J. Reyes-Gasga, J.L. Elechiguerra, C. Lui, A. Camacho-Bragado,J.M. Montejano-Carrizales, M.J. Yacaman, *J. Cryst. Growth,* **286**, 162, 2006.

[37] C.G. Tao, W.G. Cullen, E.D. Williams, S.E. Hunyadi, C.J. Murphy, *Surf. Sci.*, **601**, 4939, 2003.

[38] K.L. Kelly, E. Coronado, L.L. Zhao, G.C. Schatz, *J. Phys. Chem. B*, **107**, 668, 2003.

[39] A. Kokalj, P. Gava, S. Gironcoli, S. Baroni, *J. Catal.,* **254**, 304, 2008.

[40] M. Boudart, *Adv. Catal.*, **20**, 153, 1996.

[41] G.A. Somorjai, *Introduction to Surface Chemistry and Catalysis*; Wiley: New York, 1998.

Chapter 5

Shape- and Size-Specific Chemistry of Ag Nanostructures in Catalytic Ethylene Epoxidation

5.1 Summary

In this chapter we examine the effect of Ag nanoparticle size and shape and external conditions on the selectivity of catalytic ethylene epoxidation. Shape and size controlled synthesis of Ag nanoparticles, through a solution-based approach, is used to show that silver nanocubes exhibit higher selectivity than nanowires and nanospheres. For a given shape we find that larger particles offer improved selectivity. The enhanced selectivity toward ethylene oxide is attributed to the nature of the exposed Ag surface facets; Ag nanocubes and nanowires are dominated by (100) surface facet and Ag nanospheres are dominated by (111). Furthermore we demonstrate that the concentration of undercoordinated surface sites is related to diminished selectivity to ethylene oxide. We demonstrate that a simple model can account for the impact of chemical and physical factors on the reaction selectivity. These mechanistic insights were used to design a highly selective catalyst for the ethylene epoxidation reaction.

5.2 Introduction

Low selectivity of heterogeneous catalysts has been one of the critical obstacles to a wider use of heterogeneous processes in the commercial production of high value chemicals.[1] The limited selectivity is related to a number of issues, including the lack of predictive theories that guide the discovery of the optimal catalytic site, the dearth of strategies to synthesize the targeted sites at high concentrations and the difficulties associated with preserving these sites under reaction conditions.[1,2,3] Advances in the fields of theoretical and synthetic chemistry are beginning to address some of these issues and provide a framework for the identification (based on molecular insight) and synthesis of highly selective uniform catalytic structures with high concentration of targeted surface sites.[4,5,6,7,8,9,10,11]

In Chapter 4 it was shown that the shape of catalytic silver (Ag) particles affects the measured selectivity in the epoxidation of ethylene to form ethylene oxide (EO) ($C_2H_4 + \frac{1}{2} O_2 \rightarrow C_2H_4O$). The selective product in the process is EO, while H_2O and CO_2 are produced as a result of complete combustion of ethylene and are undesired by-products. The studies showed that the selectivity to EO on Ag nanowire catalysts was significantly higher than on conventional spherical Ag particles for identical external conditions.[9] The enhanced EO selectivity of the nanowire catalysts was attributed to a higher concentration of the Ag(100) surface facets on nanowires compared spheres. Density Functional Theory (DFT) calculations showed that the Ag(100) surface facet is inherently more selective than the Ag(111) facet.

In this chapter we show that the selectivity to EO in the ethylene epoxidation reaction is further enhanced on uniform supported Ag nanocube catalysts. By comparing

the catalytic performance of Ag nanocubes, pentagonal nanowires, and spherical catalytic particles of varying size, we derive a simple model, which can account for the impact of chemical (for example, inherently different outcome of a chemical process on catalytic particles of different shapes), and physical (size of catalytic particles, and the impact of external operating conditions) factors on the reaction selectivity. Our studies show that catalytic particles of controlled size and shape not only represent promising heterogeneous catalysts for selective production of chemicals, but also act as a critical platform to study heterogeneous catalytic process and identify crucial factors that impact process selectivity.[12]

5.3 Experimental Methods

5.3.1 Ag Nanocube Synthesis

The synthesis reported here is based on previous reports.[13] 5 mL ethylene glycol (JT Baker item 9300, low Cl <. 1 PPM and lower Fe concentrations < .01 PPM) and a magnetic stir bar (must be cleaned with piranha clean or something similar) were added to a 20 mL vial and submerged in an oil bath heated to 140-145 ^{0}C on a stirring hotplate. The cap to the vial was loosely placed on top to allow boiling off of vapors from any contaminant solvent. The solution was heated for 1 hour. 100 μL of 30mM HCl in ethylene glycol solution was added to the hot ethylene glycol. 5-10 minutes was allowed for this solution to homogenize. 3 mL of 0.1M AgNO3 (99% purity, Sigma Aldrich cat. No. 209139) in ethylene glycol and 3 mL of 0.15M polyvinylpyrrolidone (55,000 M.W. Sigma Aldrich cat. No. 856568) in ethylene glycol were added to the heated vial using a syringe pump at a rate of 0.75 mL/min. At this point the cap was loosely placed back on

the vial, (1 turn just to secure the cap). This solution was allowed to react for a period of about 24 hrs. After 24 hours the cap on the vial can be tightened such that the vial becomes airtight (the solution is basically colorless at this point). Over the next 2-3 hours a series of color changes were observed resulting in a thick tan/ocher colored solution. This produced cubes of about 60 nm edge-length. To increase the size of the cubes to 90-100 nm, the aliquot of acid should be reduced to 60 μL. Large cubes (350 nm) were synthesized using Sigma Aldrich ethylene glycol (No. 324558, 99.8% anhydrous) heated to 140-145^{0}C, the vial was loosely capped to allow for evaporation of vapors. 100 μL of 30 mM HCl was added to the solution after 1 hour of heating. 3mL of 0.3M $AgNO_3$ and 3 mL of 0.45M PVP were then added at a rate of 0.75 mL/min. Once again the cap was loosely placed on the vial; the growth took place over the course of 2-3 hours resulting in a tan/ocher color.

5.3.2 Ag Nanowire Synthesis

The smaller nanowire synthesis (75 and 125 nm) is identical to the nanocube synthesis, except the cap should be closed after 6 hours. Large wires (175 nm) were synthesized using Sigma Aldrich ethylene glycol heated to 140-145 ^{0}C, cap was loosely placed on the vial to allow for evaporation of vapors. 3mL of 0.25M $AgNO_3$ and 3 mL of 0.375M PVP were then added at a rate of 0.75 mL/min. Once again, the cap was loosely placed on the vial; the growth took place over the course of 2-3 hours resulting in a tan/ocher color.

5.3.3 *Ag Nanosphere Synthesis*

The 75 nanospheres were synthesized using a similar process to the large wire and cube sunthesis. 5mL Sigma Aldrich ethylene glycol was heated to 160-165 ^{0}C. 3mL of 0.10 M AgNO3 and 3 mL of 0.6M PVP were quickly added to the solution and the vial cap was tightened. Reaction was stopped after 1 hr. 100 nm spheres were obtained by increasing the $AgNO_3$ concentration and PVP concentration by 2.5 times. Spherical particles of 1 μm diameter were synthesized using a wetness impregnation method. A pre-cleaned monolith was contacted with a silver nitrate ($AgNO_3$) solution with a small excess of Ag compared to the desired loading, and dried in air at 90 ^{0}C. The catalyst was reduced in-situ, prior to the start of the reaction, in a hydrogen atmosphere at 300 ^{0}C for 3 hours.

5.3.4 Catalyst Preparation

The nanostructure catalysts were prepared using concentrated solutions of nanoparticles in ethanol as the impregnation solution (solutions were concentrated using centrifugation). The α-Al_2O_3 foam monolith was then contacted with the impregnation solution and was allowed to dry at 70ºC in air. The weight loadings were estimated knowing the concentration of nanoparticles in solution and verified by weighing the support before and after impregnation. The polymeric stabilizer and any impurities were removed from the nanoparticles by exposing the catalyst to air for 3 hours at 500 K. X-Ray photoelectron spectroscopy and Surface Enhanced Raman Spectroscopy were utilized to confirm that the catalysts were free of any contaminant that could impact selectivity measurements.

5.3.5 UV-visible Absorbance Spectroscopy

UV-vis absorbance spectroscopy was performed using an Evolution 300 UV-visible spectrometer made by Thermo-Fisher. Samples were prepared by diluting a purified nanoparticle solution in de-ionized water. Concentrations of different size and shape nanoparticles were adjusted such that all measured absorbances were on the same scale.

5.3.6 Scanning Electron Microscopy (SEM)

Scanning Electron Micrographs were obtained using FEI Nova 200 Nanolab. Ag nanoparticles were deposited from ethanol solution onto pre-cleaned Si wafers for imaging in the as-synthesized state. For the imaging of Ag nanoparticles on support, the monolith was cross-sectioned and directly imaged. Accelerating voltage was 5kV for all images.

5.3.7 *Transmission Electron Microscopy (TEM)*

Transmission electron micrographs were obtained on a JOEL 3011 high resolution TEM. Dilute solutions of Ag nanoparticles in ethanol were deposited on Cu grids prior to imaging. The nanostructures were brought into focus, and the sample stage was rotated to align the nanostructure along the desired zone axis, based on the selected area electron diffraction patterns. Image J software was used to analyze lattice spacing. The lattice spacing was averaged over 15 atomic layers.

5.3.8 *Reactor Studies*

All reactor studies were performed in a horizontally oriented tube reactor operated isothermally at 510 K and atmospheric pressure. A 1.0 g α-Al2O3 foam monolith support (99.5%, Vesuvius Hi-Tech Ceramics) with surface area of 0.3 m^2/g was used in all experiments. The monolith was secured in a quartz reactor tube using quartz wool. Total inlet flow rate was kept constant at 100 sccm; gas flowrates were controlled using gas flow controllers and all gases used were the highest purity available. The catalysts were pretreated at 500K in 25 sccm O_2 and 65 sccm N_2 for three hours to remove the stabilizer and all impurities. All catalysts were allowed to run at 10 sccm O2 and C2H4 and 80 sccm N_2 until they reached steady state (usually at least 24 hours). The O_2/C_2H_4 ratio was then varied by increasing the O_2 flowrate, decreasing the N_2 carrier gas flowrate while holding the C2H4 flowrate constant. Product gases were analyzed in line with a Varian gas chromatograph (Varian CP 3800) equipped with TCD and FID detectors. The selectivity was calculated using the FID and the TCD to ensure accurate measurements.

5.4 Results and Discussion

5.4.1 Catalyst Characterization

To study the effect of size and shape of Ag catalytic particles on the selectivity in ethylene epoxidation, three different sizes of Ag spherical, nanowire and nanocube structures were synthesized. All particles were synthesized using a modified polyol process, where the concentrations of precursor and modifier were varied to control size and shape (see experimental section).[13] Scanning electron microscopy (SEM) and UV-vis absorbance spectroscopy were used to ensure that the tested catalyst samples

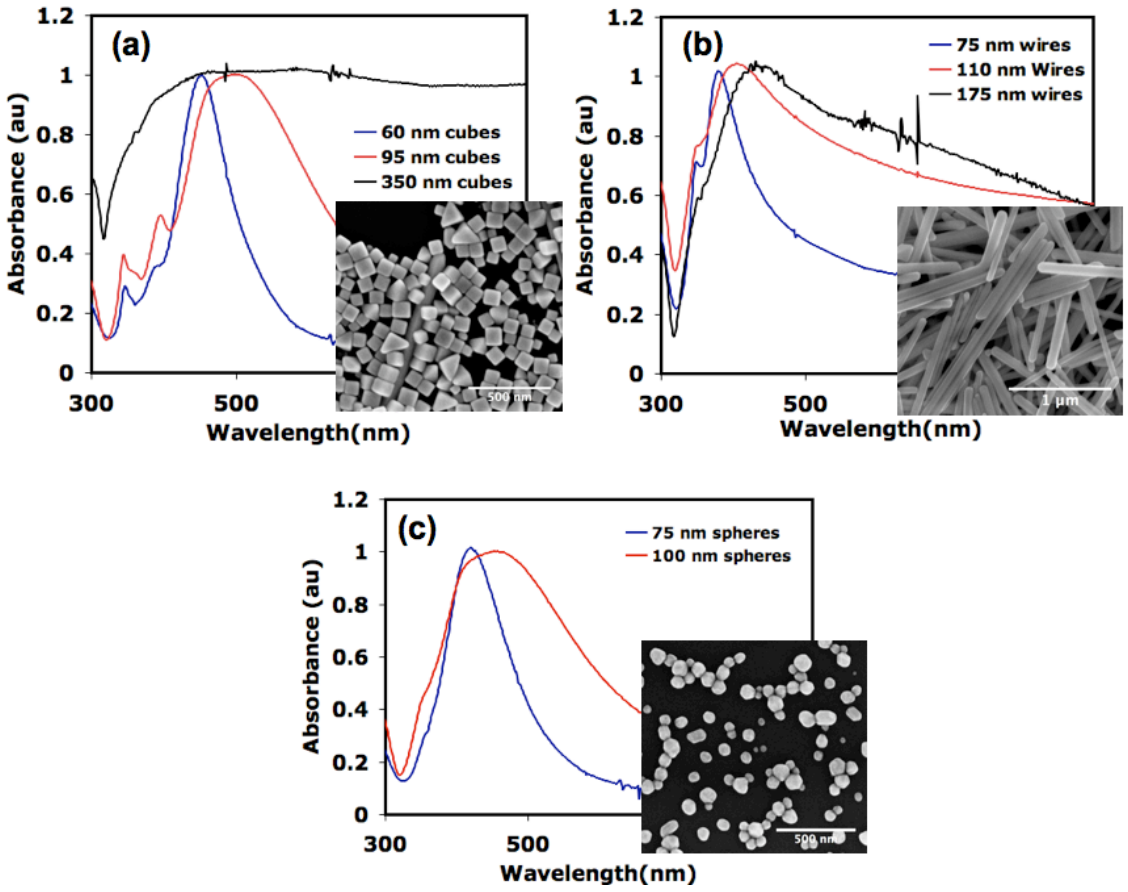

Figure 5.1 Physical characteristics of Ag nanoparticles used in these studies. UV-vis extinction spectra and representative SEM images of the Ag nanocubes (a), Ag nanowires (b) and Ag nanospheres (c) used in these studies.

contained uniform Ag particles of desired shape and size. Figure 5.1 shows representative SEM images of as-prepared 90 nm nanocubes, 125 nm nanowires and 100 nm nanospheres samples deposited on a Si wafer. The SEM images show that each sample is very uniform in terms of both the size and shape of Ag nanoparticles. Figure 5.1 also shows UV-vis spectra associated with all 9 catalysts used in this study. The shape and peak position of the UV-vis spectra, which is due to the excitation of surface plasmons, show that each sample contains uniform size and shape Ag nanoparticles, see the discussion on shape and size dependent plasmon resonance in Chapter 3. In addition, comparison of the measured UV-vis absorbance spectra to the spectra calculated using finite-difference time-domain (FDTD) method showed that the respective samples contained Ag particles of fairly uniform size and shape.

High resolution-transmission electron micrographs (HRTEM) and selected area electron diffraction (SAED) patterns of a representative as-prepared Ag nanocube and nanowire are shown in Figure 5.2. The HRTEM micrograph of the nanocube, Figure 5.2(a), was obtained by aligning the electron beam parallel to the (100) plane. The analysis showed that the average distance between the Ag planes was 0.204 nm, which is consistent with the (100) surface termination.[14] Figure 5.2(b) shows a HRTEM micrograph of the edge of a pentagonal Ag nanowire obtained with an electron beam aligned parallel to the (111) plane. The beam path is indicated with a red arrow in the inset on Figure 5.2(b). The distance between successive planes was measured to be 0.236 nm. The measured plane-to-plane distance agrees with previous HRTEM analysis and DFT calculations, which shows that the bulk lattice structure of the nanowire is an unstrained FCC structure and that the nanowire is terminated with the (100) plane.[14,15]

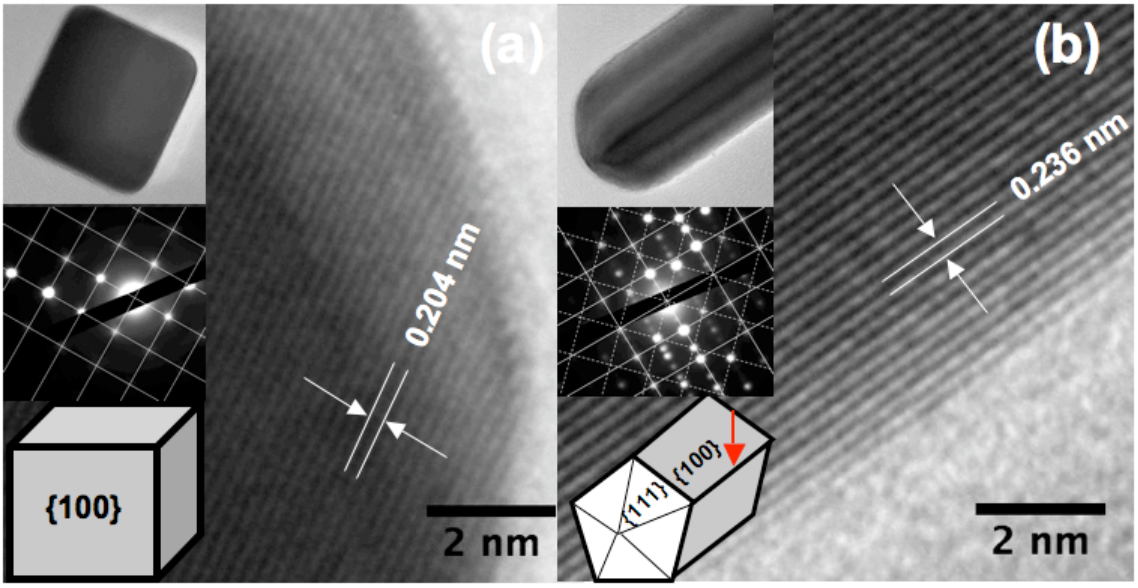

Figure 5.2 HRTEM Characterization of Ag nanoparticles. HRTEM images of (a) the Ag nanocube and (b) the Ag nanowire. Insets : Top) zoomed-out TEM images of the nanostructures; middle) selected area electron diffraction patterns used for zone axis identification; bottom) model structures. The arrow in 1(b) indicates the beam path aligned parallel to the (111) plane.

The measured SAED patterns in Figure 5.2 are also consistent with the proposed (100) surface terminations of the Ag nanowires and nanocubes.[15] The TEM analyses are consistent with previous studies showing that Ag nanocubes and pentagonal nanowires are terminated by the (100) surface facet.[16,17] It is important to note that previous measurements have shown that while the bulk of an Ag nanowire is an unstrained FCC structure, the nanowires are slightly strained in the regions where two sides of the pentagon meet each other, which might result in higher concentration of dislocations and undercoordinated sites on the nanowires compared to nanocubes.[15]

5.4.2 The Effect of Shape on Ethylene Oxide Selectivity

To measure intrinsic selectivity of the catalysts containing Ag nanostructures, we performed reactor studies where the selectivity to EO was measured at differential conversions (~2-4% of ethylene was converted in all measurements) of reactants. We performed the experiments at differential conversions to insure that the loss of the EO selectivity due to subsequent reactions of EO was minimal for all samples. The reported selectivities were measured when a steady-state conversion was achieved, typically after 24 hours on stream. All catalysts contained Ag nano-structures deposited on α-Alumina supports and were pre-treated using an identical procedure. The weight loadings were manipulated to ensure similar conversions on all catalysts. The weight loadings, pre-treatment and external conditions were all chosen to remove any possible effects on selectivity not related to the geometric feature of the Ag catalysts. Figure 5.3 shows the EO selectivity as a function of the size and shape of Ag catalytic particles, as well as the partial pressure of O_2, $P[O_2]$, for 6 different catalysts measured at

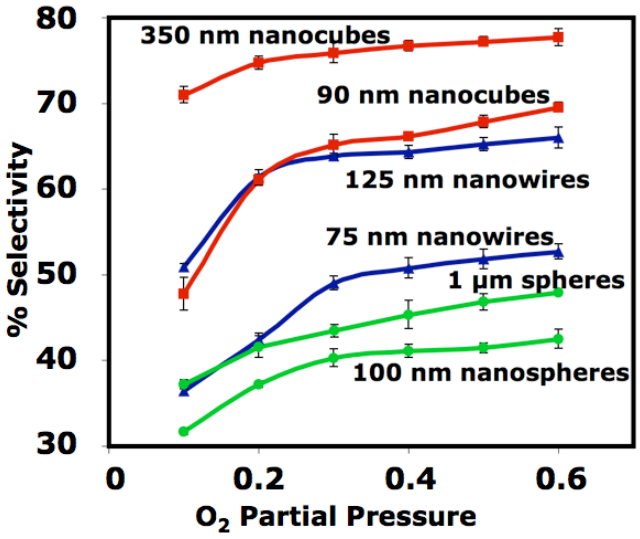

Figure 5.3 Shape, size, and environment dependent EO selectivity. Selectivity to EO for Ag nanocubes, nanowires, nanospheres of 2 different sizes over a range of P[O_2].

Catalyst	Loading [g][a]	Surface area Ag [$m^2 g^{-1}$][b]	Rate [$mmol\,g^{-1}\,min^{-1}$][c,d]
90 nm cubes	0.027	0.029	2.3×10^{-3}
350 nm cubes	0.063	0.022	9.6×10^{-4}
75 nm wires	0.012	0.060	1.2×10^{-2}
125 nm wires	0.014	0.042	9.6×10^{-3}
100 nm spheres	0.009	0.06	1.9×10^{-2}
1 µm spheres	0.12	0.069	1.5×10^{-3}

[a] 1.0 g α-Al_2O_3 monolith support used in all experiments; [b] based on weight loading and idealized particle geometries; [c] measured at a p_{O_2}/p_{Et} ratio of 2.5; [d] rate calculated on per gram Ag basis.

Table 5.1 Table showing the physical characteristics of the catalysts used in the experiments shown in Figure 5.3.

510 K. The partial pressure of ethylene was 0.1 for all experiments and the balance was N_2. Weight loadings, surface areas (estimated based on idealized particle geometries), and measured rates are reported in Table 5.1.

There are three main observations that can be drawn from Figure 5.3: (i) for a given set of external conditions, nanocube and nanowire catalysts are significantly more selective than the nanosphere catalysts for all particle sizes with Ag nanocubes showing better performance than Ag nanowires, (ii) for a given particle shape, higher selectivity is obtained on larger particles, (iii) as the $P[O_2]$ is increased (higher oxygen/ethylene ratio) the selectivity to EO increases.

The discrepancy in the EO selectivity among particles of different shapes can be explained with inherently higher selectivity of the Ag(100) facet compared with the Ag(111) facet. The Ag(100) facet is present at higher concentrations on the surface of Ag nanocubes and nanowires compared to spherical particles which are dominated by the Ag(111) surface facet. We have shown previously using quantum chemical calculations that the higher inherent selectivity of the Ag(100) facet can be attributed to a preferential ring closure of the surface oxametallacycle (it has been proposed that the oxametallacycle is a critical surface intermediate that governs the selectivity in ethylene epoxidation on Ag)[18,19,20] to form EO on this surface compared to the Ag(111) surface.[9] The data in Figure 5.3 shows that large Ag nanocubes exhibit exceptionally high rates for a pure Ag catalyst. The selectivity is measured to be 72-77% towards EO based on external conditions. This is significantly higher than typically observed for spherical Ag nanoparticles dominated by the (111) facet.

Figure 5.4 shows SEM images of the 90 nm Ag nanocubes and the 125nm Ag nanowires through the synthesis, deposition on support and reaction process. The figure shows that there is no change in shape or uniformity of the nanoparticle during the deposition of the particles onto the Al_2O_3 support. The post reaction SEM images (48 hrs on stream) show that, while there is change in the particle morphology, the shapes of the used Ag nanostructures are still discernible. While we did not test extensively the stability of the catalysts, we have observed 2-3% loss in selectivity during the course of a typical lab scale experiment (48 hours).

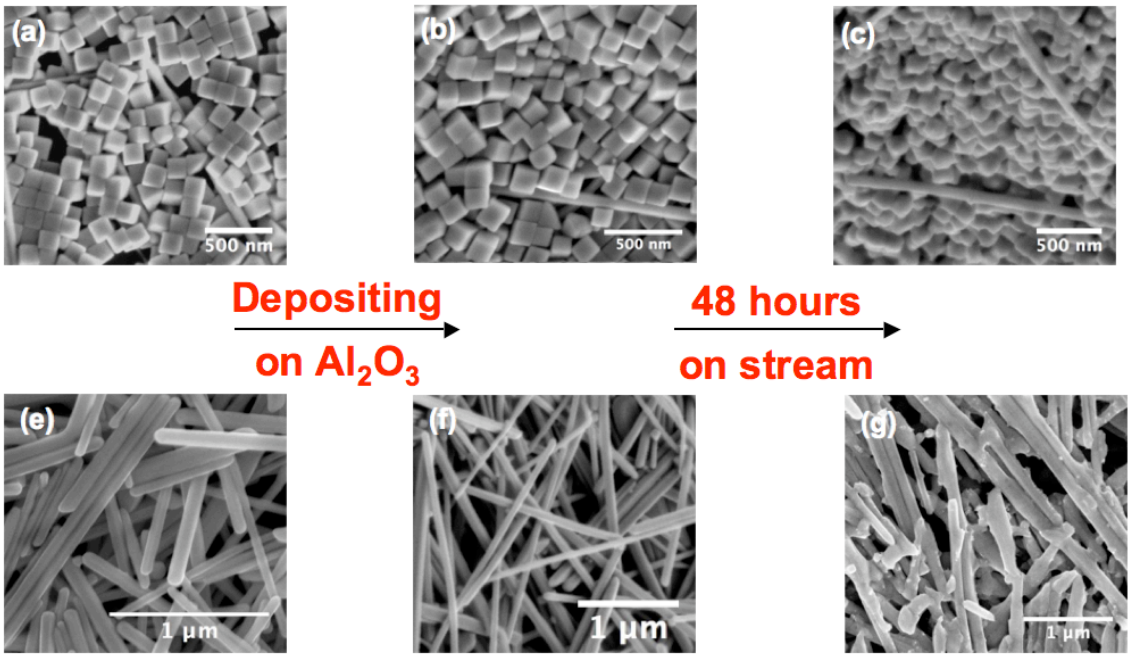

Figure 5.4 Ag nanoparticle stability. SEM images of as-synthesized Ag nancubes (a), Ag nanocubes deposited on Al_2O_3 (b) and Ag nanocubes after 48 hours under reactions conditions. The same series of SEM images are shown for Ag nanowires (d)-(f).

5.4.3 The Effect of Nanoparticle Size on Selectivity

Figure 5.3 shows that for a given particle shape, the EO selectivity is affected by the size of particles. The effect of particle size on the product distribution in a catalytic process is usually explained in terms of the particle-size-dependent concentration of under-coordinated (atomic steps and particle edges) surface sites.[21,22] For a static particle geometry, the relative concentration of under-coordinated surface sites with respect to well-coordinated sites decreases with increasing particle size. For example, if we assume perfect particle geometries, the ratio of under-coordinated surface sites with respect to well-coordinated terrace sites for a given particle shape scales as 1/characteristic length (1/L). The characteristic length for the cube is edge length, while for spheres and wires the characteristic length is diameter. In Figure 5.5 we plot the EO selectivity measured at differential conversion and a $P[O_2]/P[Et]$ ratio of 2.5 as a function of inverse characteristic lengths (1/L) for different shapes of Ag particles. The linear relationships in Figure 5.5 imply that under-coordinated sites on Ag particles might be involved in the formation of unselective products. Smaller particles have larger concentration of the under-coordinated sites and therefore the catalysts are less selective. Similar linear relationships between the EO selectivity and the concentration of under-coordinated sites were obtained irrespective of operating conditions. It is worth noting that if the selectivity plot in Figure 5.5 is extrapolated to $1/L \rightarrow 0$ (infinitely large surface facets, i.e., the Ag single crystal surface) the nanowire and nanocube selectivity would reach ~ 80 %, while the selectivity of spheres would reach ~ 45 %. The extrapolated selectivity for spherical particles is consistent with previously measured EO selectivity on the clean Ag(111) single crystal surface.[23,24,25]

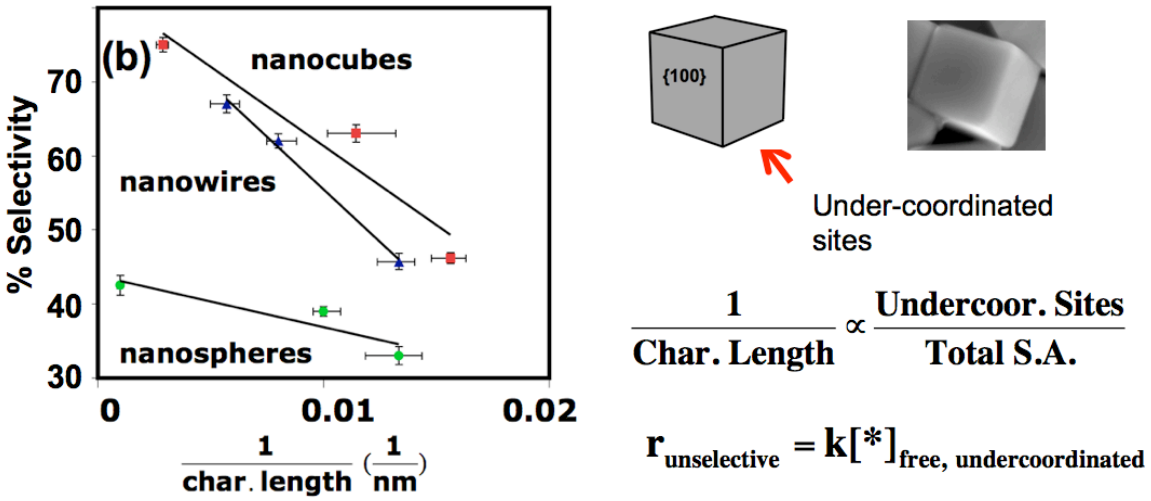

Figure 5.5 The role of under-coordinate sites in dictating EO selectivity. Selectivity as a function of L^{-1} for nanocubes, nanowires and nanospheres of 3 different sizes. The model on the right shows that the linear relationships between selectivity and L^{-1} indicate that the under-coordinated Ag sites are not selective towards EO.

5.4.4 Effect of External Conditions on Selectivity

Figure 5.3 also shows that for all tested sizes and shapes of Ag particles, the selectivity increase as the $P[O_2]$ increases. We also found that ethylene conversion increases as a function of $P[O_2]$, which is not surprising considering that ethylene has a positive reaction order with respect to $P[O_2]$.[25] To investigate the impact of the $P[O_2]$ on the selectivity to EO, in Figure 5.6(a) we have plotted differential EO selectivity as a function of $P[O_2]$ for Ag nanocubes of 60, 90 and 350 nm edge length. We define the differential EO selectivity as the selectivity to EO associated only with the reaction products produced due to an incremental increase in $P[O_2]$, Equation 1. Where $P_{EO}(n+1)$ and $P_{EO}(n)$ are the partial pressures of EO measured at the reactor exit for an experiment n, performed with one partial pressure of O_2, and an experiment (n+1) performed with a slightly higher partial pressure of O_2. $P_{Et,0}$ is the partial pressure of ethylene fed to the reactor. This partial pressure is identical for experiments n and (n+1). X(n+1) and X(n) are the conversions of ethylene in experiments (n+1) and n respectively.

$$\text{Diff.Sel.} = \frac{\Delta P_{EO}}{\Delta P_{EO} + \frac{1}{2}\Delta P_{CO_2}} = \frac{P_{EO}(n+1) - P_{EO}(n)}{P_{Et,0}(X(n+1) - X(n))} \qquad (1)$$

Figure 5.6(a) shows differential EO selectivity for three different sizes of cubes as a function of the partial pressure of oxygen $P[O_2]$. It is observed that as the $P[O_2]$ is increased, the differential EO selectivity increases. The differential selectivity reaches a maximum value of ~ 80% at $P[O_2]/P[Et] > 3$ for all cubes of different sizes, i.e., the effect of particle size is neutralized. The discrepancy in the differential selectivity for nanocubes of different sizes at low $P[O_2]$ can be understood in terms of a high contribution to the overall rate of chemically active but not highly selective under-

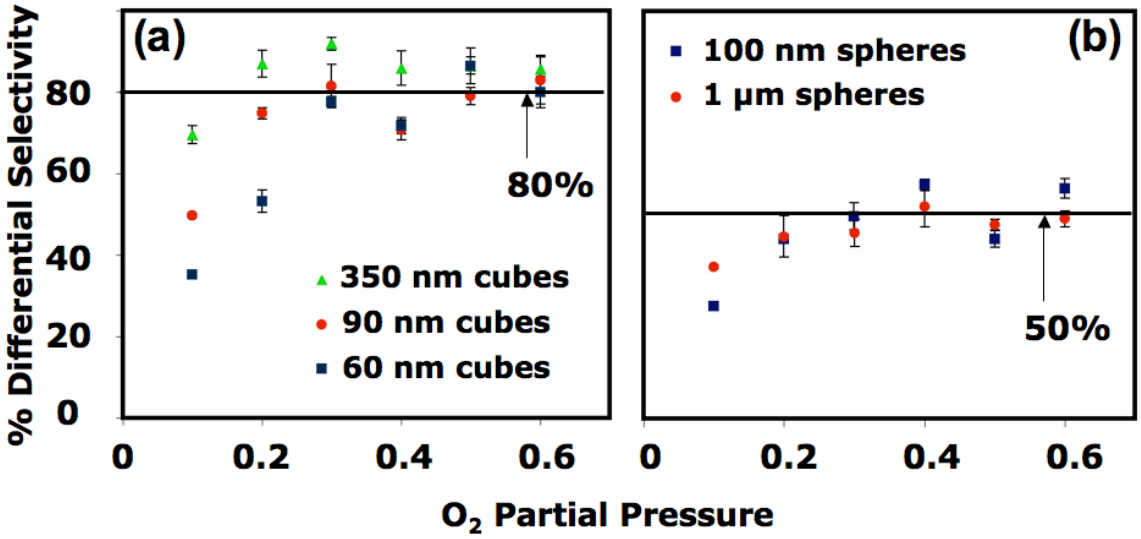

Figure 5.6 Differential selectivity versus O_2 partial pressure. a) Differential selectivity (see text for definition) vs. O_2 partial pressure for 60, 90, and 350 nm cubes. b) Differential selectivity vs. oxygen partial pressure for 100 nm and 1 mm spherical particles

coordinates surface sites. As the $P[O_2]/P[Et]$ ratio increases, the contribution of under-coordinated surface sites is saturated and less chemically active sites, such as the terrace sites, become more important, i.e., different surface sites are populated sequentially as a function of the $P[O_2]$. The differential selectivity accounts only for the selectivity associated with the reaction products produced due to the increase in the reaction rate, in response to the increase in oxygen partial pressure. At high $P[O_2]$ the differential EO selectivity is basically the selectivity due to well-coordinated surface sites which are, for a given particle shape, chemically identical regardless of the particle size. Similar asymptotic behavior of differential selectivity with respect to $P[O_2]$ is observed for Ag spheres, shown in Figure 5.6(b); however, in this case the maximum reached differential selectivity is about 50%. This once again shows the difference in selectivity of the (111), ~50%, and (100), ~80%, surfaces.

The results of the differential selectivity analyses are in direct agreement with the hypothesis that the under-coordinated step and edge sites on Ag catalysts act as combustion sites. It is well known that step and edge sites bind atomic oxygen more strongly than terrace sites.[26] Based on this difference it is expected that undercoordinated sites would saturate their oxygen coverage and correspondingly their activity, at lower $P[O_2]$ as compared to terrace sites. The results in Figures 5.6(a) and (b) show that at low $P[O_2]$, steps and edges account for a significant portion of the overall activity of smaller Ag nanostructures. As the $P[O_2]$ is increased, the undercoordinated sites become saturated, while the terrace sites are still being populated with atomic O. At high relative $P[O_2]$, only terrace sites are being populated, regardless of Ag nanoparticle size, thus the differential selectivity becomes constant, regardless of size or increasing $P[O_2]$. This

analyses, coupled with the comparison of the (100) and (111) sites, provides excellent insight into how the geometry of the active Ag site dictates the EO selectivity.

5.4.5 Design of Highly Selective Catalyst

The analysis presented above shows that the impact of the shape and size of catalytic particles on the selectivity of a chemical reaction is manifested through a complex interplay of chemical and physical mechanisms. Our studies show that catalytic particles of different shape and size might exhibit different selectivity due to; (i)shape-dependant presence of different surface facets that can activate different chemical pathways, (ii) shape- and size-dependent concentration of under-coordinated sites, and (iii) shape- and size-specific response to external operating conditions such as temperature and partial pressures of reactants. In the case of ethylene epoxidation on Ag we find that large particles terminated by the (100) facet with minimal number of under-coordinated surface sites, operated under external conditions where the impact of the under-coordinated sites is minimized should offer optimal selectivity to EO.

We have attempted to use these molecular insights to design a catalyst with high selectivity. We synthesized large Ag cubes (the edge of the cube was 350 nm), mainly terminated with the Ag(100) surface facets. To minimize the impact of low-coordinated sites we have promoted the catalysts with small amount of the chlorine promoter, fed continuously at 2 ppm in the form of vinyl chloride.[27,28,29] Vinyl chloride easily decomposes on an Ag surface forming atomic Cl.[28] Our density functional theory calculations have shown that Cl preferentially adsorbs on the low-coordinated sites of Ag, effectively poisoning these sites. The selectivity as a function of time for this

catalyst, operated at 510 K and 3:1 P[O_2]/P[Et] ratio (high enough to reach asymptotic differential selectivity) is shown in Figure 5.7. It is clear that the catalyst exhibits a very high selectivity, 84%, and good stability for the duration of the experiment (up to 15 hours). We note that the measured selectivity for this fairly simple catalyst, containing only Ag promoted with Cl, is approaching the selectivity achieved by industrial catalysts, which employ Ag particles promoted with multiple promoters including Cl, Cs, Re, and others and operated in the presence of sacrificial organic compounds such as methane and ethane.[30]

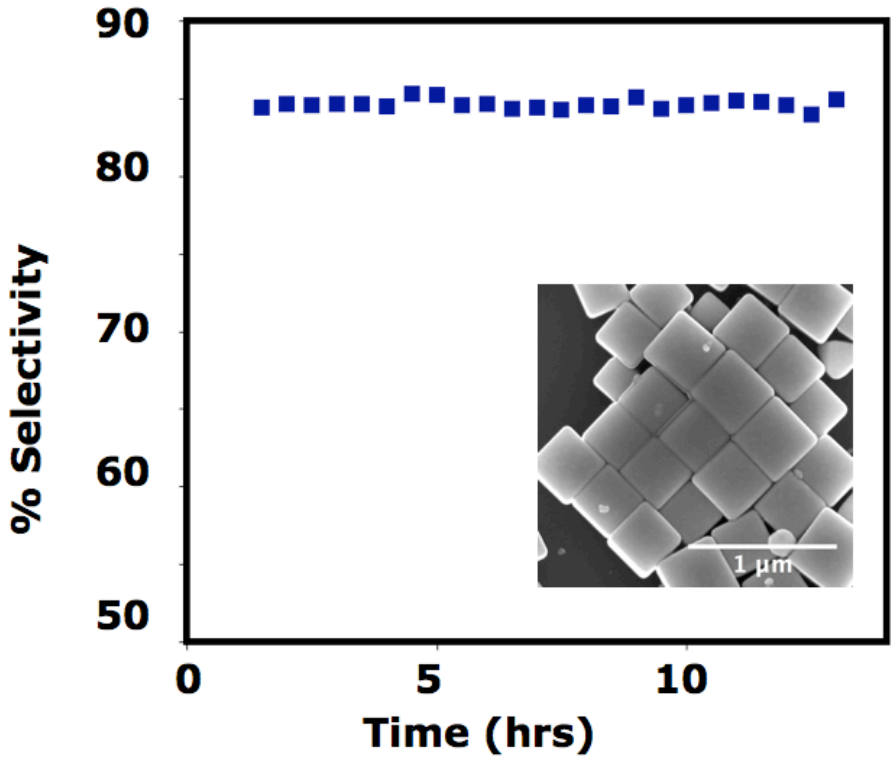

Figure 5.7 Rational design of a highly selective EO catalyst. Selectivity as a function of time for 350 nm nanocubes with 2 ppm vinyl chloride, P[O_2]/P[Et] =3, T = 510 K, steady state ethylene conversion was 3%.

5.5 Conclusions and Outlook

In conclusion, we show that the selectivity of Ag catalysts in ethylene epoxidation is governed by the nature of the Ag surface facets, the abundance of unselective under-coordinated surface sites and the operating conditions. Our studies in Chapter 4 and 5 show that the reaction selectivity can be manipulated by controlling the shape and size of Ag catalytic particles.[9,12] We also demonstrate that catalytic particles of controlled size and shape represent a promising class of materials to study heterogeneous catalytic processes and isolate physical and chemical mechanisms that govern selectivity.

These reports clearly illustrate that the size and shape of catalytic particles represent critical design levers that can be exploited to design catalytic structures with high concentrations of the surface sites that exhibit high selectivity. On a very basic level, by controlling size and shape we are effectively synthesizing surface sites that fill the large gap in the chemical activity of neighboring elements in the periodic table, allowing us to tune and optimize heterogeneous catalysts.[31] This ability to tune chemical reactivity of heterogeneous catalysts by controlled synthesis of targeted sites is particularly important for the design of selective catalysts, because small changes in the inherent chemical reactivity of a site can lead to much larger changes in selectivity toward a particular product. In addition, these reports also suggest that quantum chemical Density Functional Theory (DFT) calculations have reached a level of maturity to be useful in not only explaining various experimental observations, but also in guiding the discovery of optimal catalytic sites. Without useful predictive theories and models, such as those offered by DFT calculations and detailed experimental studies of the mechanisms of

relevant surface reactions, it will be impossible to identify the surface sites that exhibit optimal selectivity and that should be targeted in the process of catalyst synthesis.

While the findings discussed above indicate that heterogeneous catalysis could play a larger role in the commercial synthesis of high value, low volume commodity chemicals, there are a number of questions that need to be addressed. Strategies for the synthesis of shape- and size-selected metal particles are inherently complex and do not lend themselves to convenient scale-up. Furthermore, controlled synthesis of particles of targeted shapes and sizes directly on high surface area supports is currently not possible. In addition, the unique chemical activity of the above-discussed metal nanostructures is derived from their unique geometric and electronic features, which in turn are related to the fact that these structures are not the most thermodynamically stable structures. In general, under reacting environments there will be a thermodynamic driving force for metal particles of different shapes to collapse into the lowest energy structures, and for small clusters to agglomerate into larger structures. It is imperative to identify approaches to preserve the targeted, optimal shape and size of catalytic particles in reactive environments on commercial time scales, which are two to three orders of magnitude larger than standard lab time scales under which the reactions reported in the above-mentioned contributions were performed. One possible way to accomplish this task relies on lowering the operating temperature of the process.[32] The low operating temperatures would reduce the frequency of events leading to the changes in the size and shape of catalytic particles. Naturally, this means catalytic sites need to be able to activate chemical transformations at reasonable turn over frequencies at low temperatures. Another possible approach is to increase the inherent stability of the size- and shape-

specific structures. It has been suggested that this can be accomplished by encasing these structures in oxide shells or stabilizing them with organic stabilizer molecules adsorbed on the surface of the nano-structures.[33,34,35] All these approaches are in embryonic stages of their development.

In conclusion, recent developments in the areas of DFT modeling of catalytic reactions, powerful experimental techniques allowing us to study surface chemical transformation at molecular scales and often under relevant conditions, and controlled synthesis of the targeted catalytic sites potentially represent landscape changing advances that might create opportunities for the design of catalysts for the selective heterogeneous production of low volume, high value commodity chemicals. While these advances are encouraging, the scale-up issues in the synthesis of exotic nanostructures and their long-term stability under reacting environments need to be addressed.

5.6 References

[1] G.A. Somorjai, R.M. Rioux, *Catal. Today*, **100**, 201, 2005.

[2] A.T. Bell, *Science*, **299**, 1688, 2003.

[3] J.K. Norskov, T. Bligaard, J. Rossmeisl, C.H. Christensen, *Nat. Chem.*, **1**, 37, 2009.

[4] T.S. Ahmadi, Z.L.Wang, C.T. Green, A. Henglein, M.A. El-Sayed, *Science***, 272**, 1924, 1996.

[5] Y. Sun, Y. Xia, *Science*, **298**, 2176, 2002.

[6] J. Chen, T. Herricks, Y. Xia, *Angew. Chem., Int. Ed.,* **44**, 2589, 2005.

[7] R.J. Chimentao, I. Kirm, F. Medina, X. Rodriguez, Y. Cesteros, P. Salagre, J.E. Sueiras, *Chem. Commun.*, **7**, 846, 2004.

[8] K.M. Bratlie, H. Lee, K. Komvopoulos, P. Yang, G.A. Somorjai, *Nano Lett.*, **7**, 3097, 2007.

[9] P. Christopher, S. Linic, *J. Am. Chem. Soc*, **130**, 11264, 2008.

[10] I. Lee, R. Morales, M.A. Albiter, F. Zaera, *Proc. Natl. Acad. Sci. U. S. A.*, **105**, 15241, 2008.

[11] E. Nikolla, J. Schwank, S. Linic, *J. Am. Chem. Soc.*, **131**, 2747, 2009.

[12] P. Christopher, S. Linic, *ChemCatChem*, **2**, 78, 2010.

[13] S. H. Im, Y. T. Less, B. Wiley, Y. Xia, *Angew. Chem. Int. Ed.*, **117**, 2192, 2005.

[14] D.S. Su, T. Jacob, T.W. Hansen, D. Wang, R. Schlogl, B. Freitag, S. Kujawa, *Angew. Chem., Int. Ed.***, 47**, 1, 2008.

[15] J. Reyes-Gasga, J.L. Elechiguerra, C. Lui, A. Camacho-Bragado,J.M. Montejano-Carrizales, M.J. Yacaman, *J. Cryst. Growth,* **286**, 162, 2006.

[16] Y. Sun, B. Mayers, T. Herricks, Y. Xia, *Nano Lett.*, **3**, 955, 2003.

[17] C.G. Tao, W.G. Cullen, E.D. Williams, S.E. Hunyadi, C.J. Murphy, *Surf. Sci.*, **601**, 4939, 2003.

[18] S. Linic, M.A. Barteau, *J. Am. Chem. Soc.,* **125**, 4034, 2002.

[19] S. Linic, M.A. Barteau, *J. Catal.*, **214**, 200, 2003.

[20] S. Linic, J. Jankowaik, M.A. Barteau, *J. Catal*, **224**, 489, 2004.

[21] K. Honkala, A. Hellman, I.N. Remediakis, A. Logadottir, A. Carlsson,S. Dahl, C.H. Christensen, J.K. Norskov, *Science*, **307**, 555, 2005.

[22] G. C. Bond, *Surf. Sci*, **156**, 966, 1985.

[23] C.T. Campbell *J. Catal.* **94**, 436, 1985.

[24] J.G. Serafin, A.C. Liu, S.R. Seyedmonier, *J. Mol. Cat. A*: Chem., **131**, 157, 1998.

[25] J.T. Jankowiak, M.A. Barteau, *J. Catal.*, **236**, 366, 2005.

[26] B. Hammer, *Topics in Catal.*, **37**, 3, 2006.

[27] C.T. Campbell, *J. Catal.*, **99**, 28, 1986.

[28] D.P. Pursell, M.L. Bocquet, J.M. Vohs, H.L. Dai, *Surf Sci.,* **522**, 90, 2002.

[29] H. Zhang, Q. Fu, Y. Yao, Z. Zheng, T. Ma, D. Tan, X. Bao, *Langmuir*, **24**, 10874, 2008.

[30] F. Ulman, *Encyclopedia of Industrial Chemistry*, 5th, VCH: Deerfield Beach, FL, USA, 1985.

[31] T. Bligaard, J.K. Norskov, S Dahl, J. Matthiesen, C.H. Christensen, J. Sehested, *J. Catal*, **224**, 206, 2004.

[32] P. Christopher, H. Xin, S. Linic, *Nature Chem.,* **3**, 467, 2011.

[33] S. H. Joo, J.Y. Park, C.K. Tsung, Y. Yamada, P. Yang, G.A. Somorjai, *Nature Mater.*, **8**, 126, 2009.

[34] D. Aherne, D.E. Charles, M.E. Brennan-Fournet, J.M. Kelly, Y.K. Gun'ko, *Langmuir*, **25**, 10165, 2009.

[35] J. Zeng, J. Tao, D. Su, Y. Zhu, D. Qin, Y. Xia, *NanoLett*,, **11**, 3010, 2011.

Chapter 6

Using Ag Nanoparticle Plasmon Resonance to Enhance Photocatalytic Rates on TiO_2 Nanoparticles

6.1 Summary

In this chapter we show that composite materials composed of plasmonic Ag nanostructures and TiO_2 photo-catalysts show enhanced photo-activity compared to the pure TiO2 in the decomposition of methylene blue. The enhanced photocatalytic activity is attributed to radiative transfer of energy, mediated by surface plasmons, from Ag particles to the semiconductor leading to higher concentrations of charge carriers (e-/h+ pairs) in the semiconductor and therefore to higher photocatalytic activity. We demonstrate that the performance of the composite photocatalysts is a strong function of the size and shape of Ag nanostructures. This can be explained by the size- and shape-specific optical activity of Ag nano-structures. We show that by rationally changing size and shape of Ag nanostructures it is possible to maximize photo-catalytic activity of a semiconductor at a given excitation wavelength.

6.2 Introduction

In the previous chapters we showed that the size and shape of Ag nanoparticles could be manipulated to control the selectivity of the industrially important ethylene epoxidation reaction. The results showed that by manipulating the geometric structure of catalytic Ag nanoparticles, the relative concentration of various surface facets could be controlled and that this played the crucial role in dictating the process selectivity. In addition to controlling the concentration of various surface facets, controlling Ag nanoparticle shape and size allows a control over the interaction between the Ag nanoparticles and UV and visible photons.[1,2,3] In this chapter we show how the interaction between Ag nanoparticles and a UV photon source can be rationally manipulated to enhance the rate of photocatalytic reactions on nearby semiconductor photocatalysts.[4]

As discussed in the introduction to this dissertation, the development of chemical processes that are driven by solar energy is an extremely attractive route towards establishing more environmentally friendly, energy efficient chemical and energy conversion industries. One promising route towards solar driven chemical process is the use of photocatalytic materials that can directly convert the energy of a photon flux into the energy of chemical bonds. In these systems, a flux of photons is absorbed by a semiconductor, causing an excitation of an electron in the semiconductor valence band to the conductance band. The result of this process is the creation of an energetic electron in the conductance band and an energetic hole in the valence band that can both perform chemistry. The difference in energy between the valence and conductance band is known as the band gap and dictates the threshold energy required of incoming photons to drive

photocatalysis. The charge carriers separate from each other and diffuse to catalytically active sites at the semiconductor/liquid interface where they drive chemical transformations.

In addition to abundance and robustness, effective photocatalysts need to: (i) efficiently absorb photons across the UV-visible region of the solar spectrum and convert these into electron hole (e^-/h^+) pairs, (ii) have surface electronic structure tailored so that the oxidation/reduction half reactions are thermodynamically feasible, and (iii) have surface chemical properties that allow elementary surface chemical transformations associated with the oxidation/reduction half reactions to be performed with modest activation barriers. These strict constraints have made it very difficult to identify promising photocatalysts, as most single component materials do not satisfy all the requirements.[5,6,7] For example, the most investigated photocatalytic material, TiO_2, has a number of drawbacks including the large band gap, ~3.0 eV, which limits photo-absorption to the UV region of the solar spectrum.[8,9] The photo-absorption of TiO_2 can be extended to the visible region by doping with nitrogen, carbon, and a few other elements.[10,11] However, the doped materials suffer from lower absorbance than undoped TiO_2 and fast e^-/h^+ recombination rates, which ultimately limits their photo-chemical activity.

In this chapter it is shown that composites of semiconductor nanoparticles and plasmonic metallic nanostructures, represent a promising alternative to conventional photocatalysts. The main feature of these photocatalysts is that the interaction between semiconductor and metallic building blocks results in very efficient conversion of incident photons into e^-/h^+ pairs in the semiconductor. As a consequence, these materials

exhibit photocatalytic reactivities that are significantly larger than a simple superposition of the reactivities of the building block materials. We also show that the photocatalytic reactivity of the composite materials can be rationally manipulated by changing the shape, size and geometric arrangement of the building blocks. These findings suggest a large degree of design flexibility where specific combinations of semiconductors and plasmonic metallic particles can be tailored to exhibit optimal performance for a particular photo-catalytic transformation.

The conclusions were obtained in a case study showing that photocatalytic reactivity of TiO_2, quantified by the photo-decomposition of methylene blue (MB)[11], is enhanced significantly when TiO_2 is combined with plasmonic Ag nanostructures. Our analysis showed that the enhanced photo-catalytic reactivity is a result of the efficient creation of resonant Ag surface plasmons in response to a photon flux. The decay of plasmons results in energy transfer from the Ag nanostructure to TiO_2 ultimately yielding a higher concentration of TiO_2 e^-/h^+ pairs in the Ag/TiO_2 samples compared to the TiO_2-only samples. Controlling the size and shape of Ag nanostructures allows for the control of the properties of Ag surface plasmons (mainly the resonant energy and the mechanism of the plasmon decay), making it possible to tailor a particular metallic nanostructure to maximize the photocatalytic reactivity of specific semiconductors at a given excitation wavelength.

6.3 Experimental and Theoretical Methods

6.3.1 Ag and Au Nanoparticle Synthesis

The Ag nanoparticles were prepared using a modified procedure based on the polyol synthesis[12] method that we have previously reported and described in the previous chapters.[13] Briefly the Ag nanocubes were synthesized by heating 5 mL of ethylene glycol (J.T. Baker) to 143 ^{0}C for 1 hour in a stirred 20 mL vial. 100 μL of a 30 mmol HCl in ethylene glycol solution was added to the heated ethylene glycol using a micropipette. After 10 minutes, 3 mL of a 0.1 M $AgNO_3$ solution in ethylene glycol and 3 mL of a 0.15 M PVP (MW = 55,000) solution in ethylene glycol were simultaneously added to the heated ethylene glycol using a two channel syringe pump at a rate of 0.75 mL/min. The cap of vial was left open to allow oxygen to enter the synthesis vessel. Ag nanowires were formed by tightening the cap on the vial (removing the O_2 supply) after 5 hours. Ag nanocubes were synthesized by allowing 24 hours prior to removing the O_2 supply from the synthesis vessel. Ag nanospheres were synthesized by mixing 5 mL ethylene glycol, 3 mL of a 0.1 M $AgNO_3$ solution in ethylene glycol and 3 mL of a 0.6 M PVP (MW = 55,000) solution in ethylene glycol in a 20 mL vial. The solution was heated to 160 ^{o}C and allowed to react for 1 hour. All Ag particles particles were washed with acetone once via centrifugation and re-dispersed in 200 proof ethanol, prior to use in these studies.

Au nanoparticles were synthesized via the citrate reduction method,[1] concentrated by centrifugation and dispersed in a 10:1 ethanol:H_2O solution prior to drop coating on SiO_2 substrates.

6.3.2 Thin Film Deposition

The particles were drop coated onto pre-cleaned 1cm^2 SiO_2 substrates and allowed to dry in a stagnant atmosphere. Ag and Au nanoparticles were drop coated onto pre-cleaned SiO_2 substrates from the concentrated solutions. The weight of Ag or Au deposited was calibrated by drop coating known volumes onto 1cm^2 Si substrates and imaging the substrates using scanning electron microscopy. Based on particle density and size distributions, metal mass fractions were estimated. A solution of 2.3 mg of P25 TiO_2 particles in 2 mL of 200 proof ethanol was prepared and sonicated for 2 hours. 20 uL of this solution was deposited on the Ag nanoparticle covered or clean SiO2 substrates and allowed to dry in a stagnant atmosphere. This procedure produced well-dispersed films with fairly constant optical properties across the entire surface.

6.3.3. Scanning Electron Microscopy

Scanning electron micrographs were obtained using an FEI Nova 200 Nanolab. Images were obtained directly from the thin films deposited on SiO_2 substrates. The accelerating voltage was 5kV for all images.

6.3.4 UV-vis Absorbance Spectroscopy

Transmission UV-vis absorbance spectroscopy was performed using an 8453 UV-vis Chem Station spectrophotometer (Agilent Technologies). Reflection absorbance UV-vis measurements were recorded using an AvaSpec 2048 spectrometer and an AvaLight DHc compact deuterium halogen light source (Avantes).

In-situ UV-vis measurements were performed to examine the extent of charge transfer between the metal and semiconductor building blocks. Thin-film samples were

mounted on a reflective surface in a small (2 mL) beaker filled with de-aerated ethanol. The sample was illuminated with the UV light source, and reflection absorbance UV-vis measurements (through the thin-film samples) were collected every minute for 15 minutes.

6.3.5. Photoluminescence Spectroscopy

Photoluminescence (PL) measurements were made using Fluoromax-3 spectrofluorometer (Jobin Yvon/Spex Horiba, NJ). Thin-film samples were mounted on a custom designed sample holder to allow for transmission PL measurements. The excitation energy was varied and the emission spectra ware collected for various samples. The peak height of the 467 nm emission line was used to analyze the PL strength.

6.3.6. Photocatalytic Testing

Methylene blue (MB) was deposited by submerging the thin-film substrates in a 0.65 mM MB in ethanol solution for 2 hours, followed by rinsing with ethanol. The films were allowed to dry for 2 hours, in the dark, prior to photo-catalytic testing. The photo-catalytic experiments were performed using a 100W source with an emission wavelength of 365 nm and a FWHM of 4 nm, about 10mW/cm^2 at the sample. The degradation of MB was monitored using reflection UV-vis spectroscopy every 1 minute for the course of the experiment. MB concentration was monitored by following the magnitude of the 650 mn absorption peak.

6.3.7 FDTD Simulations

The interaction of light with the Ag nanoparticles was simulated using the finite-difference time-domain (FDTD) method. FDTD is a computational electro-dynamics modeling technique, which solves discretized Maxwell equations in space and time subject the input geometry, material properties, and boundary conditions.[14] The optical properties of Ag are represented using a Drude-Lorentz model[15] with empirical optical constants,[16] which has been shown to give accurate results for Ag nanostructures.[17] Extinction, scattering, and absorbance cross-sections were calculated using the total-field/scattered-field (TFSF) formalism.[14] The scattering efficiency at 365 nm was calculated by dividing the simulated scattering cross section at a wavelength of 365 nm by the particle's geometric cross-sectional area.

6.4 Results

6.4.1. Photocatalyst Characterization

Three different composite Ag/TiO_2 photo-catalysts as well as pure TiO_2 and Ag samples were tested. The three composite materials contained P25 TiO_2 nanoparticles (equivalent to 2 - 3 close-packed monolayers) deposited on SiO_2 substrates that contained sub-monolayer coverage of Ag nanostructures. The TiO_2 weight loading was kept constant at 0.023 mg for all samples and all experiments. The weight loading of Ag in different experiments ranged from 5 to 25 wt% with respect to TiO_2. We explored Ag/TiO_2 composite materials with three different Ag nanostructures: 75±13 nm diameter nanospheres, 79±12 nm edge length nanocubes, and 90±12 nm diameter nanowires with an aspect ratio > 30. SEM images of the particles are shown in Figure 6.1(a)-(c). All Ag particles were synthesized using a modified polyol process, and the polyvinylpyrrolidone

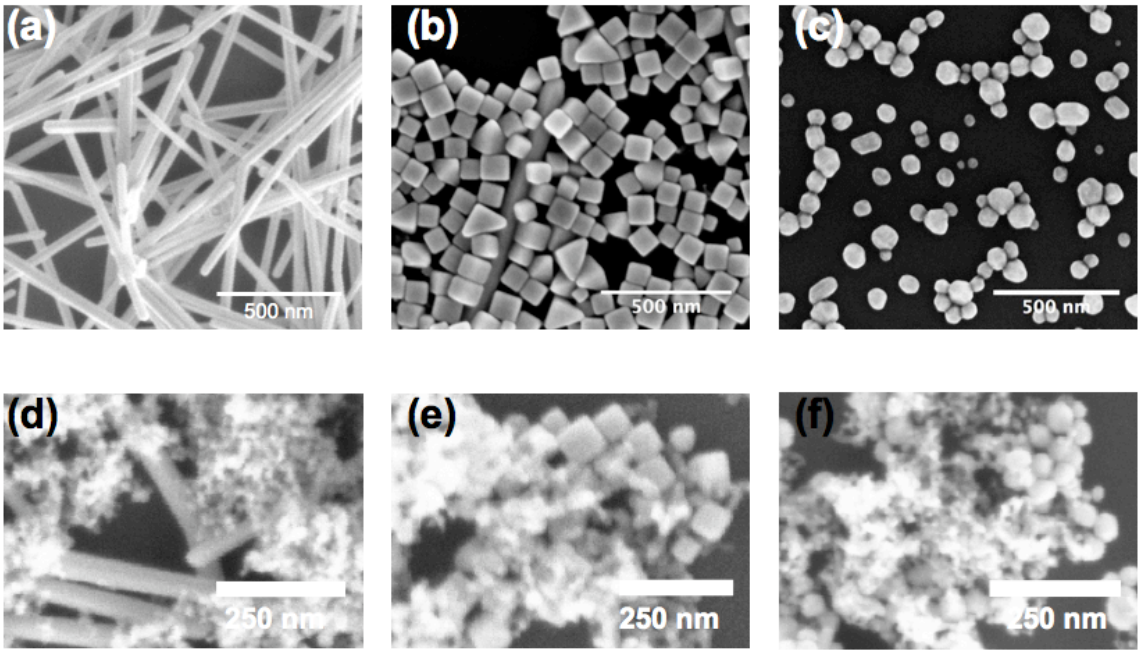

Figure 6.1 Scanning electron micrographs of the Ag and Ag/TiO_2 composite films used in these studies. (a)-(c) SEM micrographs of as-synthesized Ag nanowires, nanocubes and nanospheres on Si wafers. The scale bar is 500 nm. (d)-(f) SEM micrographs of Ag nanowire/TiO_2 composite, Ag nanocube/TiO_2 composite and Ag nanosphere/TiO_2 composite. The scale bar is 250 nm.

(PVP) stabilizer was not removed after synthesis. Representative SEM images of Ag/TiO_2 composites are shown in Figure 6.1 (d)-(f). The composite system is characterized by Ag nanostructures partially covered by P25-TiO_2. The building blocks are separated only by the non-conductive PVP stabilizer that surrounds the Ag particles. UV-vis extinction spectra for the pure Ag (Figure 6.2(a)) and Ag/TiO_2 composite films (Figure 6.2(b)) are shown in Figure 6.2. We note for this configuration the resonant energy or spectral shape of the Ag UV-vis extinction spectra, see Figure 6.2(b), is not affected significantly by TiO_2 due to the small direct contact area between Ag and TiO_2 particles and the incomplete coverage of TiO_2 on Ag.

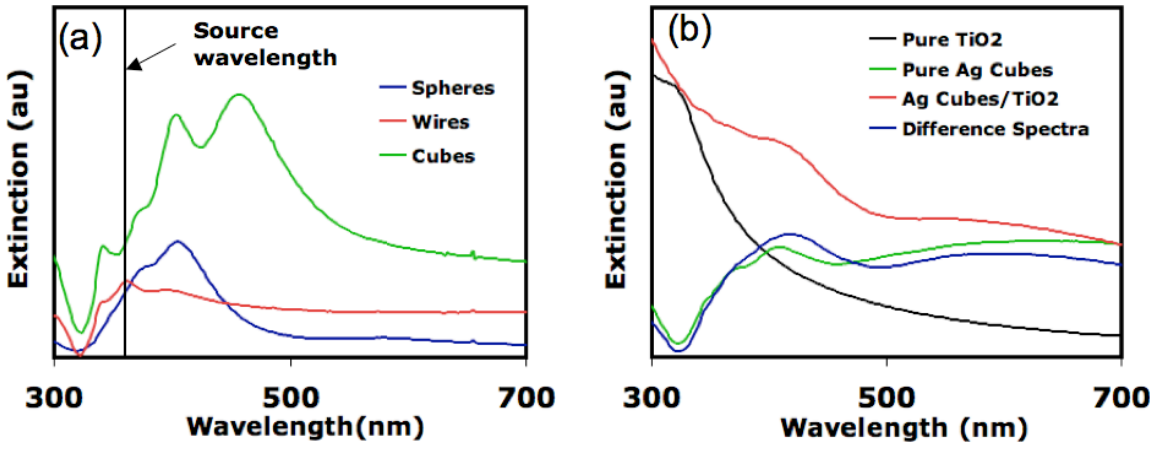

Figure 6.2 UV-vis extinction spectra of the samples used in these studies. (a) Normalized (on a weight basis) UV-vis extinction spectra for Ag nanowire, nanosphere and nanocube films on a SiO_2 substrate. (b) UV-vis spectra for a ~60-nm Ag cube sample, a P25 TiO_2 sample, composite sample and a difference spectrum calculated by subtracting the contribution of TiO_2 from the composite spectrum. All spectra were recorded in transmission mode through the SiO_2 supporting substrate.

6.4.2 Photocatalytic Methylene Blue Decomposition Experiments

Figure 6.3 shows the result of the MB decomposition experiments for the pure TiO_2, pure Ag, and the Ag/TiO2 composite materials. The Ag/TiO_2 composite systems shown in Figure 6.3 contained a 15% weight loading of Ag particles with respect to the TiO_2 loading. We note that the interfacial area between the Ag nanoparticles and the TiO_2 are similar, regardless of shape. Figure 6.3 shows that: (1) the decomposition rate is first order in MB, (2) the pure Ag systems do not exhibit measurable photocatalytic activity, (3) the composite materials exhibit enhanced rates of MB decomposition compared to pure TiO_2, and (4) the magnitude of the rate enhancement on the composite materials compared to pure TiO_2 is a function of the shape of Ag nanostructure. The measured rate enhancement factors for the Ag/TiO2 composite systems compared to pure TiO2 were 2.1 for the Ag nanowires composite, 2.4 for the Ag nanospheres composite, and 3.8 for the Ag nanocubes composite.

6.5 Mechanistic studies

6.5.1 Potential Plasmon Mediated Enhancement Mechanisms

There are a number of physical mechanisms that could potentially explain the enhanced photo-catalytic reactivity of the composite systems compared to pure TiO2 including: (i) electron transfer from TiO_2 to Ag nanoparticles effectively increasing the lifetime of e^-/h^+ pairs (Figure 6.4(a)),[18,19] (ii) electron transfer from Ag to TiO_2 mediated by Ag surface plasmons (Figure 6.4(b)),[20,21] (iii) the localized heating of Ag nanostructures due to the non-radiative decay of Ag surface plasmons into phonon modes in the Ag particles (Figure 6.4(c)),[22,23] and (iv) transfer of photons from Ag

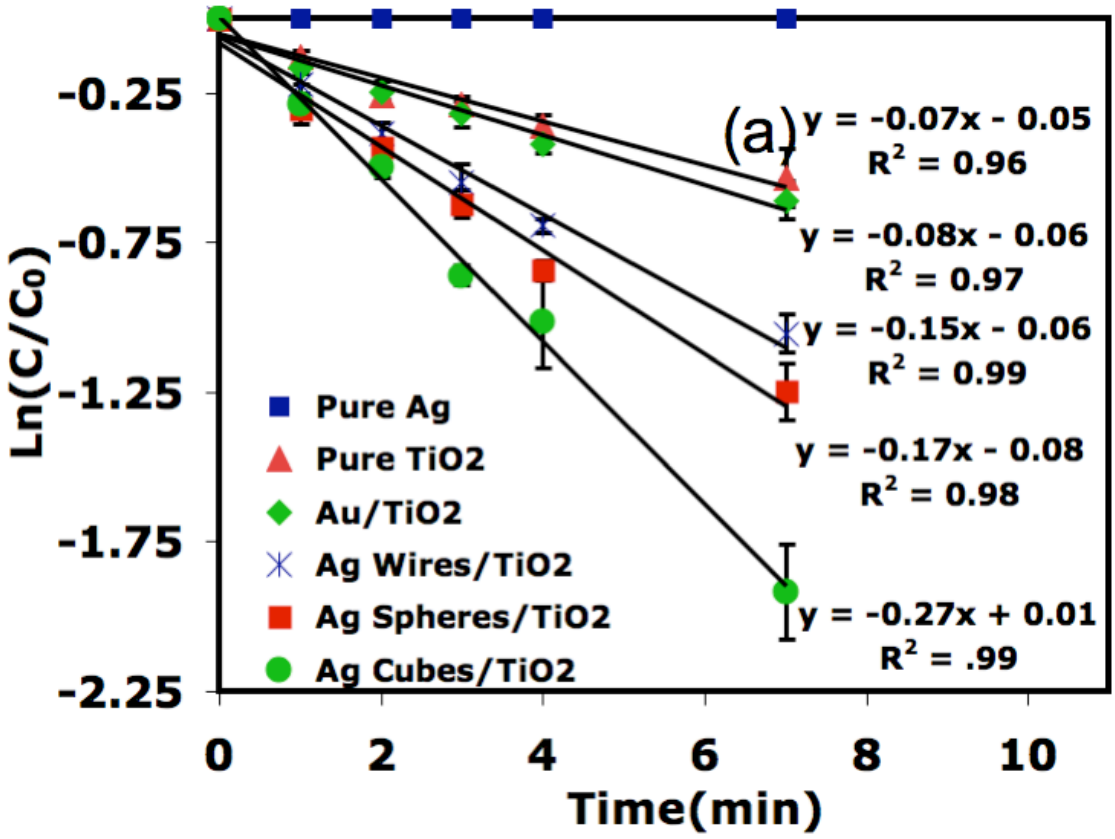

Figure 6.3 Performance of the photocatalysts for methylene blue decomposition. Kinetic data (first order batch reactor analysis) for the decomposition of methylene blue is shown for pure TiO_2, pure Ag nanocubes, 15 wt% composite Ag/TiO_2 photo-catalysts containing Ag spheres, cubes and wires, and an Au/TiO_2 composite photo-catalyst.

nanoparticles to TiO2 via radiative decay of surface plasmon states to excite electrons in TiO2 and increase the concentration of e-/h- pairs (Figure 6.4(d)).[24]

Since the proposed mechanisms, (ii) – (iv), are mediated by Ag surface plasmons it is important to discuss the ways by which surface plasmons could affect the photo-activity of TiO_2. When exposed to UV-vis radiation, nanoparticles of coinage metals (mainly Ag and Au) exhibit large extinction cross-sections. This extinction cross section is the consequence of the formation of surface plasmons. The spectral shape and intensity of the extinction spectra are function of the particle size, shape, and local environment.[1,2,3] The impact of particle shape on the extinctions spectra is illustrated in Figure 6.2(a) where we show the UV-vis extinction spectra, normalized on a per weight basis, for as-synthesized Ag nanowires, nanocubes and nanospheres deposited on SiO_2 substrates. The SEM images of the Ag nanostructures are shown in Figure 6.1(a-c). The excitation and subsequent decay of surface plasmon states is manifested through three resonant processes: (a) non-radiative decay: absorption of photons which excite phonon modes, lattice vibrations, that locally heat the particle, (b) radiative decay: Rayleigh scattering process where photons are concentrated at the surface of the particle and scattered in high intensity in the vicinity of the particle without being degraded into heat, and (c) direct transfer of electrons from plasmon states to surrounding, electron-acceptor medium.[25,26]

6.5.2 Electron Transfer From Semiconductor to Metal

The proposed mechanism labeled (i) is motivated by previous reports[18,19,27] that by impregnating particles of noble metals on TiO2, the lifetime of e^-/h^+ pairs and the

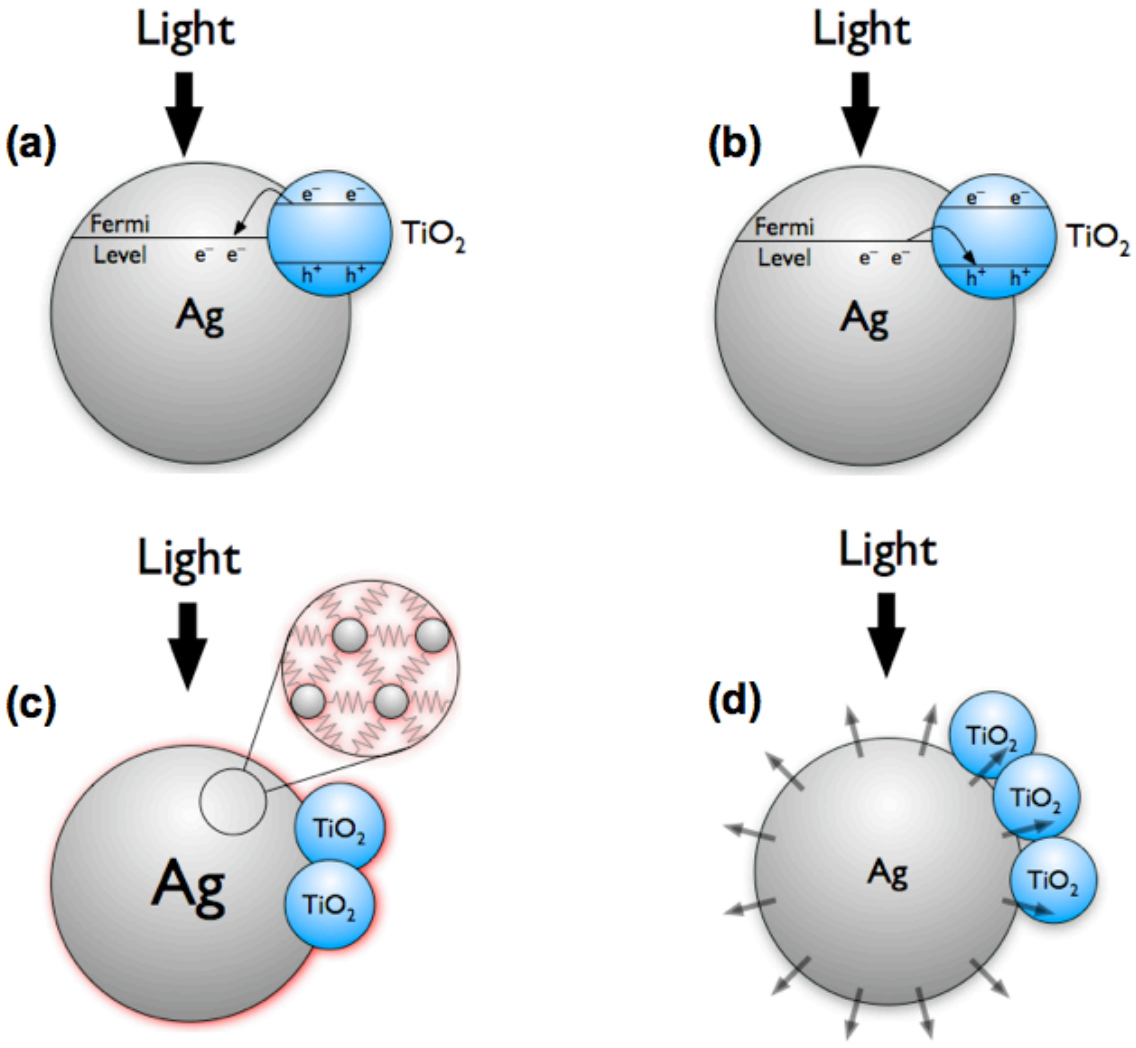

Figure 6.4 Potential mechanisms for photo-catalytic rate enhancement. (a) Charge transfer from TiO_2 to Ag. An excited electron in the TiO_2 conduction band is transferred to the Ag Fermi level. (b) Charge transfer from Ag to TiO_2. Energetic electrons produced due to plasmon excitation transfer to TiO_2. The transfer can occur from Ag to the TiO_2 conduction or valence bands. (c) Plasmon induced nanoparticle heating due to the non-radiative decay of excited plasmons. (d) Intense, plasmon induced, radiative energy transfer from Ag to TiO_2.

photocatalytic reactivity of the system are enhanced. The enhancement in the lifetime of e^-/h^+ pairs is attributed to the transfer of excited electrons from TiO_2 to metal particles.[27] To test this hypothesis we performed MB decomposition measurements using Au/TiO_2 composite materials. In these materials, Au nanoparticles, stabilized by citrate ligands, were deposited in a similar geometric arrangement as Ag nanostructures in the Ag/TiO_2 composites. The Au nanoparticles are spherical in shape with diameters ~30nm and the weight loading was 5% with respect to TiO_2. We choose Au because its electronic structure, characterized by a filled d-band and valance s-band, is similar to Ag. In addition, the work function of Au is larger than Ag suggesting that there should be a larger driving force to transfer electrons from TiO_2 to Au than Ag.[28,29] The results for the decomposition of MB on the Au/TiO_2 sample are shown in Figure 6.3. The figure shows that the Au/TiO_2 samples showed very little enhancement in photocatalytic reactivity compared to pure TiO_2 materials. These measurements suggest that the metal-facilitated separation of charge in the TiO_2 semiconductor particles is not the driving force for the observed Ag-induced enhancement in the photocatalytic reactivity of TiO_2. The insignificant contribution of this mechanism to the rate enhancement is not surprising considering that in our composite systems the direct contact between metallic nanoparticles (Au or Ag) and TiO_2, required for an efficient electron transfer, is limited by the geometric arrangements of the particles (small direct contact area) and the presence of non-conductive polymeric stabilizers on the metallic particles. It is also important to point out that although Au nanoparticles exhibit SPR, the resonant energy is lower that the energy of the source (2.2 eV vs. 3.4 eV) used in the experiment. This indicates that the SPR of Au was not excited during these experiments and any

mechanism involving the interaction of the Au surface plasmon states and TiO_2 is not operational in this system.[1]

6.5.3 Plasmon Induced Electron Transfer From Metal to Semiconductor

The proposed mechanism labeled (ii) above is based on the direct injection of electrons from the excited Ag surface plasmon states into TiO_2. To test whether this mechanism is significant we measured the absorption spectra for Ag/TiO_2 composites illuminated by the 365 nm source as a function of illumination time. It has been shown previously that charged TiO_2 particles exhibit an absorption peak at 680 nm, and that electron deficient Ag nanostructures show red-shifted surface plasmon resonance.[20] Figure 6.5 shows that upon the irradiation of the composite sample in a de-aerated ethanol solution, there was no appearance of the 680 nm TiO_2 band and we observed very little shift in the Ag surface plasmon resonance. The de-aerated solution was used only in this set of experiments to avoid a possible transfer of electrons from conduction band of TiO_2 to O_2. These measurements suggest that there is no significant charge transfer from Ag to TiO_2. The measurements do show a very small amount of charge transfer from TiO_2 to Ag. This can be seen in the difference spectra, showing a broad decrease in extinction (due to loss of electrons in TiO_2) and a small increase where the plasmon resonance peak is. The magnitude of this change is much too small to justify the rate enhancements and is in line with the small increase in activity seen in the Au/TiO_2 case. The lack of significant change in the absorption band of TiO_2 and the plasmon peak of Ag during the course of the *in-situ* UV-vis experiments shows that there is no significant charge transfer in either direction during the photo-catalytic reaction.

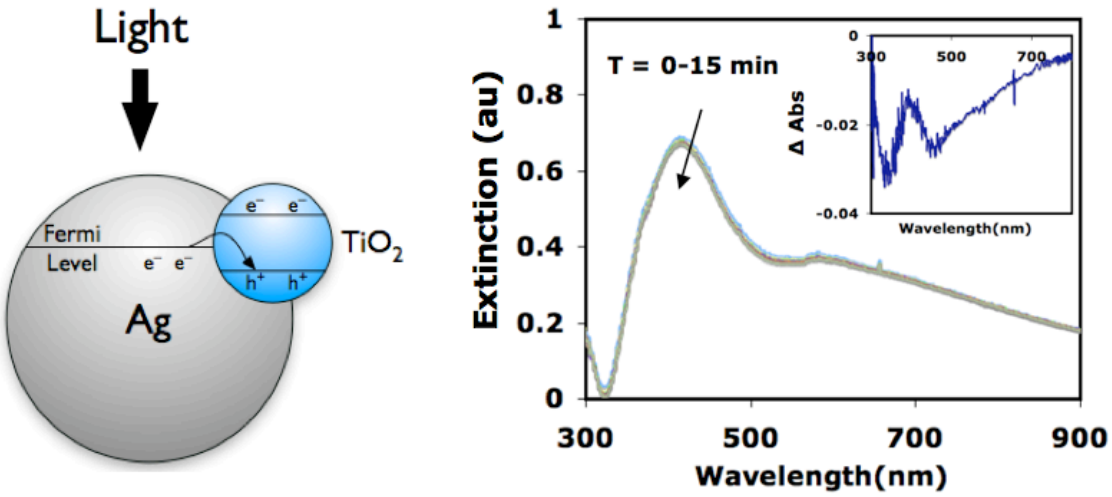

Figure 6.5 Testing the charge transfer mechanism. The change in UV-vis absorbance of Ag nanospheres in a composite Ag/TiO_2 film as a function of the irradiation time is shown. The contribution of TiO_2 to the spectra was subtracted from the composite spectra to obtain the Ag absorbance. The inset shows the difference spectrum, calculated by subtracting the spectrum at T=15 from T = 0 min. The difference shows a very small charge transfer from TiO_2 to Ag, but cannot account for the magnitude of the rate enhancement.

6.5.4 Local Heating Mechanism

We have also hypothesized above, mechanism (iii), that the surface plasmon induced localized heating of Ag nanoparticles can lead to thermo-chemcial degradation of MB on the Ag nanostructures. To test this hypothesis we measured the degradation of MB on illuminated samples that contained only Ag without any TiO_2. The results of these measurements are shown in Figure 6.3. The figure shows that samples containing only Ag nanostructures did not activate the decomposition of MB, therefore indicating that the local Ag heating is not responsible for the degradation of MB. These findings are consistent with previous reports, which showed that local heating of metallic particles is only important for fairly small particles (<30nm diameter).[25,26] Since the Ag particles used in our studies have significantly larger diameters it can be assumed that the local heating of Ag nanostructures is insignificant, and the majority of surface plasmon decay through the radiative Rayleigh scattering process.[30]

Furthermore, a number of experimentally verified models have been developed to model the heating of plasmonic nanoparticles under continuous wave illumination.[31,32,33] The models, in general, allow for a calculation of the steady state nanoparticle temperature increase as a function the light intensity (I_0), the optical properties of the nanoparticle, the size and shape of the nanoparticle, and the thermal conductivity of the surrounding medium (k_∞) as the input parameters. The models assume the nanoparticle temperature is constant throughout the volume. The steady state nanoparticle surface temperature is calculated by considering heat conduction to the surrounding medium, which is kept at a constant temperature (T_∞), Equation 1. Using the parameters from our system, I_0 = 10 mW/cm^2, K_{abs} (absorption efficiency) = 5, r_0= 60 nm, k_∞=.04 W/m/K for

air, we estimate a steady state temperature increase of $1.3*10^{-4}$ K. The small of temperature increase clearly cannot be driving the observed enhancement in photo-catalytic activity in the composite Ag photocatalysts.

$$T = T_{\infty} + \frac{I_0 K_{abs} r_0}{6k_{\infty}} \qquad (1)$$

6.5.5 Radiative Energy Transfer

Based on the analysis above, the proposed mechanisms (i) – (iii) can be ruled out, and it can be inferred that the enhanced photocatalytic activity of Ag/TiO_2 composite systems is based on the plasmon-mediated transfer of energy from Ag nanoparticles to TiO_2 to increase the concentration of e^-/h^+ pairs in the system. The main feature of Ag nanostructures that enables the observed amplifications in the photo-catalytic reactivity of the composite system is their large extinction cross-section (more specifically, the scattering cross-section), which results in an efficient conversion of a source photon flux into e-/h+ pairs in TiO_2.

To further verify the proposed mechanism we have characterized our photo-catalysts using photolumeniscence (PL) emission measurements. In these measurements we have monitored the intensity of the 466 nm TiO_2 emission peak for the composite systems and divided these intensities by the emission intensity of pure TiO_2 at a given excitation wavelength. Figure 6.6 shows that, for TiO_2 mass, the PL emission intensity is higher for the composite systems compared to pure TiO_2 over a tested range of excitation wavelengths. Figure 6.6 also shows that the enhancement in the PL emission intensity tracks very well the UV-vis absorbance of Ag nanostructures used to synthesize

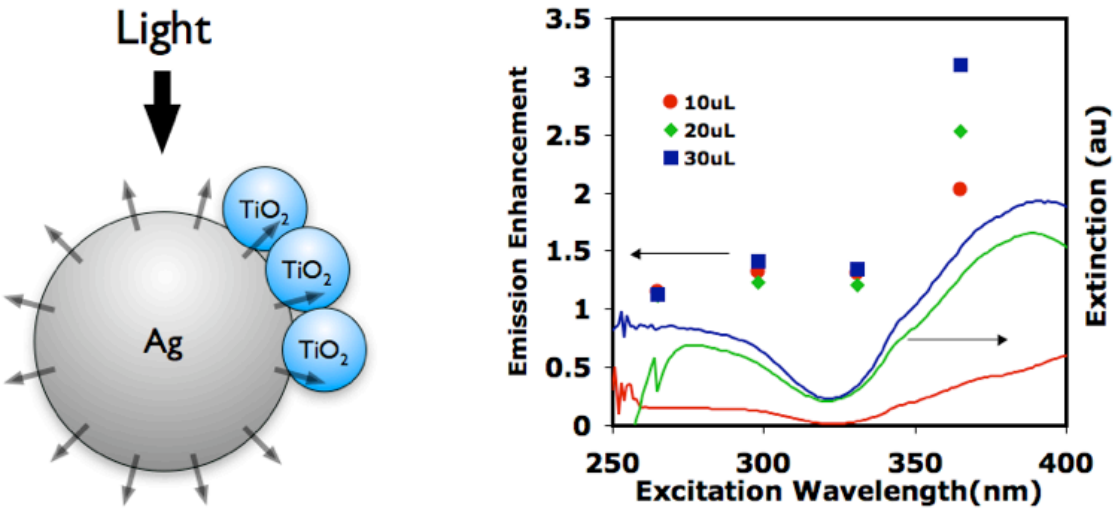

Figure 6.6 Testing the radiative energy transfer mechanism. (Left axis, corresponds to symbols) photoluminescence emission enhancement at the 466nm peak as a function of excitation wavelength for 3 nanosphere/TiO_2 composite systems. The systems contain 3 different Ag nanosphere loadings. Data labels denote the volume of Ag nanoparticle solution deposited on the substrate. (Right axis, corresponds to data lines) Corresponding UV-vis extinction spectra for the Ag particles used to make the composites.

the composite materials. In general we observed that for the excitation wavelengths close to 380 nm, i.e., those excitation wavelengths that had the largest overlap with the Ag surface plasmon resonance, the PL intensity was the largest. As the excitation wavelength was moved away from the surface plasmon resonance peak, the PL enhancement factors decreased. These results indicate that the observed enhanced PL emission from TiO_2 is due to the enhanced absorbance (mediated by Ag surface plasmons) of the composite systems compared to the TiO_2 only system.[34] This is in contrast to previous reports of the enhanced PL emission in Au/CdTe composite systems, which were assigned to the Au surface plasmon mediated enhancement in the emission (not absorption) rates.[35]

The proposed mechanism that the excitation of surface plasmons in Ag is responsible for the enhanced photocatalytic reactivity of the composite systems is further supported by the results in Figure 6.7(a). The figure shows a linear relationship between integrated areas under the extinction spectra (in the region of the UV source, between 362 – 368 nm), which we termed integrated plasmon intensity, for pure Ag samples (the samples contained different concentrations of different Ag nanoshapes with no TiO_2) and the measured MB decomposition rate for the corresponding composite Ag/TiO_2 materials derived from these pure Ag samples. The linear relationship indicates that the rate enhancement can be directly related to the Ag extinction cross-section, which is the consequence of the excitation of surface plasmons.

It is important to note that the integrated plasmon intensities in Figure 6.7(a) were a function of the particle shape. We found that the mass (volume) of Ag nanocubes required to achieve similar plasmon intensities was approximately 50 % compared to the

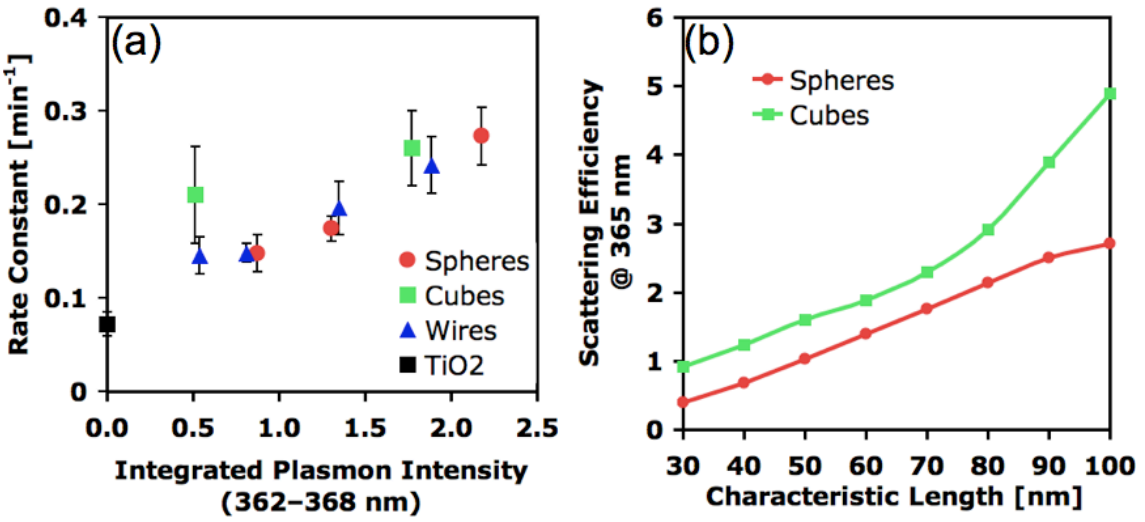

Figure 6.7 Experimental and theoretical evidence that plasmons enhance photocatalytic activity. (a) Rate constants measured for composite systems are plotted as a function of the Ag plasmon intensity at the source wavelength for films containing only Ag particles of different shapes. We found that the concentration of Ag spheres and wires required to achieve a given plasmon intensity was twice as high as the concentration of Ag cubes. (b) Scattering efficiencies calculated at 365 nm using FDTD simulations for Ag cubes and spheres of different sizes.

Ag nanospheres and nanowires. This is consistent with the results in Figure 6.2(a). These observations explain the results in Figure 6.3, showing that the Ag nanocubes offer higher rate enhancements compared to Ag nanospheres and nanowires of similar size for identical Ag mass (volume). The superior rate enhancement of nanocubes can be explained by a higher scattering efficiency of these nanostructures. This is further supported by the calculated scattering efficiencies for Ag nanocubes and nanospheres, shown in Figure 6.7(b). The figure shows that 75 nm nanocubes scatter 365 nm light more efficiently than nanospheres of similar size. The simulations are described in the experimental section.

6.6 Conclusion and Outlook

In conclusion, we showed that efficient plasmonic light concentrators, such as metallic nano-structures of coinage metals, can be employed to enhance the concentration of e^-/h^+ pairs in semiconducting materials and therefore to improve their photocatalytic activity. We show that the enhancement in the activity is dependent on the shape and size of plasmonic metallic nanostructures. By controlling the size and shape of metallic nanostructures it is possible to optimize their extinction cross-section for a given source wavelength, and therefore tune their impact on the photo-catalytic activity of different semiconductors. In this case, non-doped TiO_2 absorbs in the UV region of the spectra and the best scatterers of UV light, and consequently the optimal Ag nano-structures for enhancing photo-catalytic activity of TiO_2, are Ag nanocubes. We believe that similar strategies can be used with semiconducting materials that absorb in the visible region.

This work has been recently extended to show that (a) plasmonic nanoparticles can be added to semiconductor electrodes to significantly enhance the rate of visible light driven photo-electro-chemical water splitting and (b) that the radiative transfer mechanism proposed here can be understood in terms of two combined effects.[36] The first effect, termed far-field scattering, utilizes the Ag nanoparticles as nano-mirrors that effectively increase the path length of photons in the composite material, thereby giving semiconductor particles a larger chance to absorb the photons. The second effect, termed near field electromagnetic mechanism, takes advantage of the strong electromagnetic fields at the nanoparticle surface to selectively create large concentration of e^-/h^+ pairs at the semiconductor surface. This mechanism serves to increase the concentration of e^-/h^+ pairs in the semiconductor and selectively create the e^-/h^+ pairs at the semiconductor surface, where recombination rates are significantly diminished. This work highlights the utility of plasmon nanostructures for enhancing semiconductor photo-catalysis.

6.7 References

[1] S. Link, M.A. El-Sayed, *J. Phys. Chem. B,* **103**, 4212, 1999.

[2] A. Liebsch, *Phys. Rev. B: Condens. Matter Mater. Phys.,* **48**, 11317, 1993.

[3] K.L. Kelly, E. Coronado, L.L. Zhao, G.C. Schatz, *J. Phys. Chem. B*, **107**, 668, 2003.

[4] P. Christopher, D. B. Ingram, S. Linic, *J. Phys. Chem. C*, **114**, 9173, 2010.

[5] M.R. Hoffman, S.T. Martin, W. Choi, D.W. Bahnemann, *Chem. Rev.*, 95, 69-96, 1995.

[6] Z. Zou, J. Ye, K. Sayama, H. Arakawa, *Nature,* **414**, 625, 2001.

[7] A. Mills, S. Le Hunt, *J. Photochem. Photobio., A,* **108**, 1, 1997.

[8] A.L. Linsebiger, G. Lu, J.T. Yates, *Chem. Rev.,* **95**, 735, 1995.

[9] J. Wang, *et. al., J. Am. Chem. Soc.*, **131**, 12290, 2009.

[10] T. Lindgren, *et al. Sol. Energy Mater. Sol. Cell* **, 84**, 145, 2004.

[11] A. Houas, *et. al., Appl. Catal., B* **, 31**, 145, 2001.

[12] S.H. Im, Y.T. Lee, B. Wiley, Y. Xia, *Angew. Chem. Int. Ed.,* **44**, 2154, 2005.

[13] P. Christopher, S. Linic, *ChemCatChem*, **2**, 78, 2010.

[14] A. Taflove, S.C. Hagness, Computational Electrodynamics: The Finite-Difference Time-Domain Method, 3rd. ed.; Artech House, Inc.: Norwood, MA, 2005.

[15] W. Ashcroft, N.D. Mermin, *Solid State Physics*, Brooks Cole, 1976.

[16] E.D. Palik, ed., *Handbook of Optical Constants of Solids*, Academic Press: San Diego, 1985.

[17] J.M. McMahon, *et. al., J. Phys. Chem. C,* **113**, 2731, 2009.

[18] V. Subramanian, E.E. Wolf, P.V. Kamat, *J. Am. Chem. Soc.,* **126**, 4943, 2004.

[19] T. Hirakawa, P.V. Kamat, *J. Am. Chem. Soc.,* **127**, 3928, 2005.

[20] Y. Tian, T. Tatsuma, *J. Am. Chem. Soc.*, **127**, 7632, 2005.

[21] K. Yu, Y. Tian, T. Tatsuma,, *Phys. Chem. Chem. Phys.*, **8**, 5417, 2006.

[22] C. Yen, M.A. El-Sayed, *J. Phys. Chem. C,* **113**, 19585, 2009.

[23] J.R. Adleman, D.A. Boyd, D.G. Goodwin, D. Psaltis, *Nano Lett.*, **9**, 4417, 2009.

[24] H. Awazu, *et. al., J. Am. Chem. Soc.,***130**, 1676, 2008.

[25] L. Brus, *Acc. Chem. Res.,* **41**, 1742, 2008.

[26] P.K. Jain, X. Huang, I.H. El-Sayed, M.A. El-Sayed, *Acc. Chem. Res.***, 41**, 1578, 2008.

[27] J.T. Yates, *Surf. Sci.*, **603**, 1605, 2009.

[28] B. Hammer, J.K. Norskov, *Nature*, **376**, 238, 1995.

[29] A. Ruban, B. Hammer, P. Stoltze, H.L. Skriver, J.K. Nørskov, *J. Mol. Catal. A: Chem.*, **115**, 421, 1997.

[30] D.D. Evanoff, G. Chumanov, *ChemPhysChem*, **6**, 1221, 2005.

[31] V.K. Pustovalov, *Chem. Phys.*, **308**, 103, 2005.

[32] G. Baffou, R. Quidant, F.J. Garcia de Abajo, *ACS Nano*, **4**, 709, 2010.

[33] A.O. Govorov, *et al. Nanoscale Res. Lett.*, **1**, 84, 2006.

[34] J. Lee, *et. al., Angew. Chem. Int. Ed.,* **45**, 4819, 2006.

[35] J. Lee, A.O. Govorov, J. Dulka, N.A. Kotov, *Nano Lett.*, **4**, 2323, 2004.

[36] D.B. Ingram, S. Linic, *J. Am. Chem. Soc.,* **133**, 5202, 2011.

Chapter 7

Visible Light Enhanced Catalytic Oxidation Reactions on Plasmonic Ag Nanostructures

7.1 Summary

Catalysis plays a critical role in chemical conversion, energy production and pollution mitigation. High activation barriers associated with rate-limiting elementary steps require most commercial heterogeneous catalytic reactions to be run at relatively high temperatures. High operating temperatures compromise energy efficiencies of catalytic processes and long-term stability of catalysts. We show that plasmonic nanostructures of silver can concurrently use low intensity visible light (on the order of solar intensity) and thermal energy to drive catalytic oxidation (ethylene epoxidation, CO oxidation and selective NH_3 oxidation) reactions at lower temperatures than their conventional counterparts that use only thermal stimulus. Based on kinetic isotope experiments and density functional calculations, we postulate that excited plasmons on the Ag surface act to populate O_2 anti-bonding orbitals, forming a transient negative ion state, thereby facilitating the rate-limiting O_2 dissociation reaction. The results open avenues to the design of more energy efficient and robust catalytic processes.

7.2 Introduction

In the previous chapters it was shown that Ag nanoparticles of well controlled sizes and shapes possess excellent catalytic properties and strong interactions with visible photons through the excitation of surface plasmons. These findings raise the question of whether plasmonic nanostructures can act directly as photocatalytic materials? As discussed in the previous section, photocatalytic materials are exclusively based on semiconductors. Metallic surfaces typically have very low photocatalytic efficiency due the lack of band gap and short lifetimes of energetic charge carriers. We show in this chapter that plasmonic nanoparticles can efficiently couple thermal energy and visible photon flux (of solar intensity) to efficiently drive important chemical reactions through a photocatalytic mechanism.

The rates of heterogeneous catalytic reactions are usually limited by one elementary chemical step, referred to as the rate-limiting step. For example, the rates of partial oxidation reactions on noble metals (Ag and Au) are typically limited by the rate of molecular oxygen dissociation on the surface of metal catalysts.[1,2] The large activation barrier associated with the rate-limiting step results in processes that are run at relatively high temperatures to achieve reasonable product yields. High operating temperatures have a number of negative side effects. First, the processes are characterized by low energy efficiency since significant input of thermal energy is used to run chemical transformations that are inherently exothermic. Second, high operating temperatures compromise the long-term stability of catalysts.[3] Third, for many partial oxidation reactions higher operating temperatures decrease the selectivity to the desired products since these products are easily thermally activated on the catalyst.[2,4,5]

All commercial heterogeneous catalytic reactions are driven by thermal energy. Efforts to lower operating temperatures have mainly centered on the design of special catalytic sites that can activate the rate-limiting step with lower activation barriers.[6,7,8] This strategy has had limited success since the phase space of viable catalytic sites is restricted by their inherent lack of thermal stability. Also, catalytic sites that can thermally activate reactants at lower temperature almost always interact with adsorbates more strongly and are therefore more easily poisoned by the adsorbates.[9]

Herein, we show that plasmonic Ag nanostructures, characterized by excellent absorption of visible light through the creation of resonant surface plasmons,[10,11] can concurrently utilize thermal energy and a low intensity photon flux (on the order of solar intensity) to drive catalytic oxidation reactions at significantly lower temperatures than those associated with conventional thermal processes. Our studies indicate that energetic electrons, formed through the excitation of surface plasmons on illuminated Ag nanoparticles, are transferred from Ag to adsorbed molecular O_2 thereby inducing nuclear motion along the O_2 dissociation reaction coordinate and allowing for the activation of the O-O bond at lower temperatures in a photo-thermal (electron-phonon driven) elementary step. The findings are important since: (i) It is demonstrated for the first time that metallic nanostructures can efficiently couple thermal energy and low intensity visible photons to drive commercially important catalytic reactions,(ii) The presented results open new avenues towards the design of more energy efficient catalytic processes where a significant fraction of energy input is provided in the form of sunlight, (iii) The results suggest that since the reactions can be operated at lower temperatures, the long-term stability of catalysts and the product selectivity could be potentially enhanced.

Previous reports of photo-induced chemical transformations on plasmonic nanoparticles have been limited to non-catalytic growth of anisotropic Ag nanostructures through the plasmon-mediated reduction of Ag^{+} ions,[12,13] localized plasmon-mediated heating of metals under intense laser illumination enhancing the rates of thermo-catalytic reactions,[14] and plasmon-mediated increase in the rates of charge carrier formation in semiconductors and molecular photo-catalysts in the neighborhood of plasmonic structures, increasing the rates of photo-chemical transformations on these materials.[11,15,16] In addition, much of our understanding of photochemical processes at metal surfaces has been derived from work on well defined single crystal surfaces.[17,18,19,20,21,22] These studies have been limited to photoinduced desorption and dissociation events, in general exhibiting low reaction rates and requiring long exposure times to induce significant photoactivity in response to continuous wave photon illumination.[23,24,25] The defining feature of plasmonic nanostructures, used in our studies, making them potentially very useful in the field of photo-chemical conversion is their ability to efficiently concentrate the energy of a photon flux in a very small volume at their surface and to transfer this energy in the form of energetic electrons to adsorbed molecules. In practical terms, this means that low intensity continuous light (similar to solar intensity) can couple with thermal energy to drive photo-chemical transformations on metallic catalysts at appreciable rates.

7.3 Experimental Methods

7.3.1 Ag Nanoparticle Synthesis and Catalyst Preparation

5 mL Ethylene Glycol (J.T. Baker item 9300. Purity is very important. Only lots with Cl concentration below 0.1 PPM and Fe concentration below 0.01 PPM should be used in this synthesis) and a magnetic stir bar are added to a 20 mL vial and submerged in an oil bath heated to 140-145^{0}C on a stirring hotplate. The cap to the vial should be loosely placed on top to allow boiling off of vapors from any contaminant solvent. Allow 1 hr. for heating. After 1 hr of heating, 3 other solutions should be prepared. The first solution is 6 mL of 0.1M $AgNO_3$ (99% purity, Sigma Aldrich cat. No. 209139) in ethylene glycol. The second solution is 0.15M (in terms of repeating unit) Polyvinylpyrrolidone (PVP) (55,000 M.W. Sigma Aldrich cat. No. 856568) in 6 mL ethylene glycol, once again the solution should be shaken into solution. Lastly a stock solution of 30mM HCl in ethylene glycol should be prepared and can be used up to a month for separate synthesis. 100 μL of the 30mM HCl solution is added to the hot ethylene glycol. Allow 5-10 minutes for this solution to mix. 3 mL of $AgNO_3$ and PVP solutions are added to the heated vial using a syringe pump at a rate of 0.75 mL/min. At this point the cap should be loosely placed back on the vial. This solution should then be allowed to react for a period of about 24 hrs. After 24 hours the cap on the vial can be tightened such that the vial becomes airtight. This procedure produces cubes of ~60-70nm edge length. The cubes were washed by centrifugation in acetone 5 times and re-dispersed in 5 mL of ethanol.

100 mg of alpha-Al_2O_3 was added to the Ag nanoparticle (0.025g of Ag) solution, and sonicated for 1 hr. The solution was dried, and all Ag nanoparticles adsorbed to the Al_2O_3 surface. This produced a 20% wt Ag nanocube on Al_2O_3 catalyst. The alpha-

Al_2O_3 (Alfa Aesar # 42571) support is 5-6 m^2/g, which resulted in about 20% surface coverage of Ag nanocubes on the Al_2O_3 Support.

7.3.2 Reactor Setup

The reactions were carried out in a vertically oriented temperature-controlled packed bed flow reactor with a 1 cm^2 SiO_2 window to allow visible light illumination. The catalyst bed was 3 mm deep consisting of a 2.5 mm layer of inert SiO_2 particles with an additional 0.5 mm layer of catalyst deposited on top of the SiO_2. The catalyst was pretreated in 20 standard cubic centimeters (sccm) O_2 and 60 sccm N_2 for 2 hours at 220 ^oC at atmospheric pressure prior to starting any of the reactions.

After the pre-treatment period, for ethylene epoxidation, 20 sccm of ethylene was introduced to the catalyst along with 20 sccm O_2 and 60 sccm N_2 and the reaction was allowed to reach steady state at 220 ^oC overnight. After this line-out period the temperature was varied to examine the temperature dependent thermal and photothermal rate for all 3 reactions. At a given temperature the catalyst was allowed 15 minutes to reach steady state under dark conditions, followed by 15 minutes of visible light illumination, followed by 15 minutes in the dark to assure that the rate returned back to the initial value obtained in the dark. All catalysts were run in the differential conversion regime. The differential setup ensures that the reaction is run at low conversion, far from equilibrium, so that the inherent rate of forward reactions can be rigorously measured.

All products were quantified online using quadrupole mass spectrometry (MS) and gas chromatography (GC). Both analyses produced consistent results for activity and selectivity for all reactions. The rates reported in the manuscript were calculated using the

rate of product formation. The GC used was a Varian CP 3800 equipped with 2 TCD's and an FID detector. The MS is an Extorr XT200 operating at 10^{-6} Torr.

Temperature dependent reaction rate, selectivity and enhancement measurements were obtained by following the procedure outlined above over a range of temperatures. The enhancement is calculated as the rate under visible light illumination divided by the pure thermocatalytic rate with no illumination. The visible light source is a Dolan-Jenner Fiber-Lite 180 halogen light that produces 250 mW/cm^2 at the catalyst surface at maximum intensity.

For CO oxidation, the procedure is identical to ethylene epoxidation, after the pre-treatment 20 sccm of CO was fed to the reactor and allowed to reach steady state over night. The temperature was then varied and the products were monitored. The rate enhancements reported in the manuscript were calculated by monitoring rate of CO consumption. Similarly for NH_3 oxidation, 20 sccm of NH_3 was introduced following the pretreatment and the system was allowed overnight to reach steady state. The products, N_2, N_2O, NO, NO_2 were monitored online.

7.3.3 Impact of Light Intensity and Wavelength

The experiments were carried out at constant temperatures. The source intensity was calibrated using a CCD camera and a UV meter and varied by controlling the power to the source. At a given source intensity the system was allowed 15 minutes to reach steady state, following this 5 minutes of steady-state data was averaged for the intensity dependent rate measurements. Wavelength dependent studies were performed using a series of 7 long pass filters, Edmund Optics NT49-039. Similar to the intensity studies the

system was allowed 15 minutes to reach steady state with each filter and 5 minutes of steady state data was used to calculate the rate.

7.3.4 Isotopic Labeling Experiments

The measurements were performed at constant temperatures, using O_2^{18} (99% Sigma Aldrich 602892). The gas composition was 5 sccm O_2, 20 sccm ethylene, 75 sccm N_2. The kinetic isotope effect (KIE) was calculated by comparing the reaction rates with O_2^{16} and O_2^{18} reactants. Steady state conditions were reached 15 minutes after switching from O_2^{16} to O_2^{18}.

7.3.5 Spectroscopic Characterization

X-ray photoelectron spectroscopy (XPS) studies were performed using a Kratos Axis Ultra XPS and a monochromatic Al source. Peak positions were calibrated based on a C1s standard. Diffuse reflection UV-vis extinction spectra were recorded using a ThermoScientific Evolution 300 and the Harris Praying Mantis diffuse reflectance accessory. FTIR spectra were collected using ThermoScientific Nicolet 6700 and the Harris Praying Mantis diffuse reflectance accessory. Raman spectra were recorded using a Lambda Solutions Dimension-P1, with a 532 nm laser.

The activated sample was initially treated with 60 sccm N2 and 20 sccm O2 for 2 hours at 230 C, followed by 60 sccm N2, 20 sccm O2 and 20 sccm ethylene for 12 hours. The used sample was pretreated using the same procedure as the activated sample but was left on stream under the reaction conditions for 50 hrs.

7.4 Theoretical Methods

Density functional theory calculations were performed using the GPAW code, a real-space grid-based DFT implementation with the projector-augmented wave method.[26] The exchange-correlation interaction was approximated using the revised Perdew-Burke-Ernzerhof (RPBE) functional. The Ag(100) surface was modeled by a 2×2×3 slab with 10 Å of vacuum space. Oxygen molecule was adsorbed parallel to the Ag-Ag bridge, which was found to be most stable adsorption configuration of the O_2/Ag(100) system. The O_2 adsorbate and top two layers of the slab were allowed to relax until the force on all atoms was converged to less than .05 eV/Å.

The ground state and the excited state potential energy surface of O_2 has been mapped out in terms of the internal stretch of O-O bond using 18 irreducible k-points and a grid spacing of 0.2 Å. The linear-expansion Delta Self-Consistent Field (ΔSCF-DFT) method implemented in GPAW has been used to calculate the energetic of the electron excitation from the Fermi level to the O_2 $2\pi^*$.[27,28]

7.5 Experimental Results

7.5.1 Catalytic System

We focus on the commercially important partial oxidation (epoxidation) of ethylene to form ethylene oxide. In 2008, ~ $ 20 billion worth of ethylene oxide was produced in this process, making it the highest value heterogeneous catalytic process where selectivity – the competing undesired products are CO_2 and H_2O – is the crucial descriptor of catalytic performance (ICIS News, *Ethylene Oxide (EO) Uses and Market Data*, http://www.icis.com/v2/chemicals/9075772/ethylene-oxide/uses.html). We also

examined the oxidation of CO to CO_2 and the selective oxidation of NH_3 to N_2 on identical Ag catalysts. These are important reactions for the reduction of automotive and industrial pollution and employ expensive Pt-group catalysts due to the difficulty of activating O_2 over cheaper Ag catalysts at low temperatures.[29,30] The reactions were performed in a vertically oriented reactor that allows both temperature control and catalyst illumination, Figure 7.1(a). We used a visible light source with a total maximum intensity of ~ 250 mW/cm^2 (2-3 times solar intensity) at the entrance of the catalyst bed and maximum spectral intensity at ~2.1 eV (590 nm) Figure 7.1(b). We chose a source with almost no UV radiation to remove the possibility of directly exciting interband transitions in Ag, which occurs at energies about ~3.8 eV.[31] The thickness of the catalyst bed was sufficient to insure a complete absorption of the photon flux, i.e., the system is operated in a light limited regime and the rates of the photo-thermal reactions reported below are a lower bound of what is expected if the reactions are run in an excess of photons. Thermal (no light) and photo-thermal (light on) rate measurements were carried out in a differential reactor setup in the regime limited by the reaction kinetics (i.e., without reactant transport limitations) under steady state conditions.

The catalysts contained Ag nanocubes of ~ 60 nm edge length supported on α-Al_2O_3 particles, Figures 7.1(c) and (d). The amount of Ag was ~ 20 % by weight with respect to the oxide support. We use cubic nanostructures since it has been shown previously that cubes are more selective in ethylene epoxidation than nanospheres and nanowires.[32,33] In addition, cubic nanostructures exhibit higher plasmon intensity than spheres and nanowires.[11] The size of the catalytic particles was chosen based on a compromise between catalytic performance (larger nanocubes are more selective

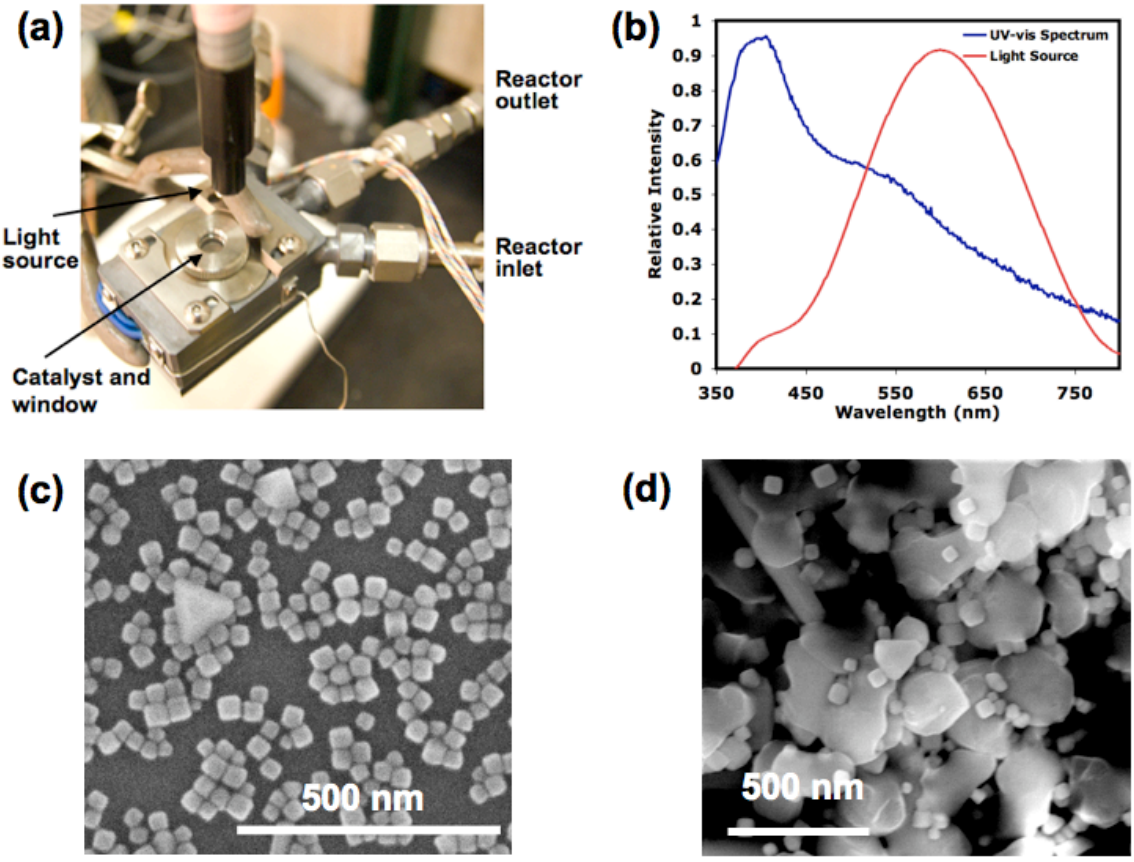

Figure 7.1 Photothermal ethylene epoxidation setup. (a) A photograph of the Harrick reactor used in these studies, showing the gas inlet and outlet, the catalyst bed and the fiber-optic light probe. (b) Overlap between the visible light source and the UV-vis extinction spectrum of the Ag nanocubes on Al_2O_3 support. (c) SEM image of the Ag nanocubes used in this study on an Si wafer. Scale bar is 500 nm. (d) SEM image of the Ag nanocubes on the Al_2O_3 support.

catalysts[32]), optical properties (UV-vis extinction cross-section[10]), and relatively high surface-to-volume ratio. The effect of particle size on plasmon resonance and catalytic properties is discussed in Chapter 3. We have also tested the photocatalytic properties of nanocubes with edge length ranging from 40-100 nm, establishing that these particles also exhibit significant light induced rate enhancement.

7.5.2 *Effect of Illumination on Catalytic Activity and Selectivity*

Figure 7.2(a) shows the steady-state ethylene epoxidation rate at 450 K and atmospheric pressure, with and without visible light illumination. The measured thermal rates (light off) were consistent with previously reported rates on supported Ag catalysts.[34,35,36] For example, at 430 K we measure a rate of 0.4 μmol/gcat/s compared to 0.28 μmol/gcat/s.[34] Figure 7.2(a) shows that as the light is turned on (250 mW/cm^2), the steady-state reaction rate increases ~ 4 fold compared to the thermal process (no light). It is also shown that this performance is fully reversible with the reaction rate responding instantaneously (within the temporal resolution of our system) to the introduction and removal of the light flux.

Figure 7.2(b) shows the measured reaction rate in the thermal (no light) and photo-thermal (light on) processes as a function of operating temperature. The figure also shows the rate enhancement, calculated as the photo-thermal rate divided by the thermal rate, as a function of temperature. The rate enhancement decreases as a function of temperature from ~ 8-fold at lower temperatures to ~ 3-fold at higher temperatures. Figure 7.2(c) shows that the selectivity to ethylene oxide for thermal and photo-thermal processes is statistically identical at a constant rate. Similar measurements were

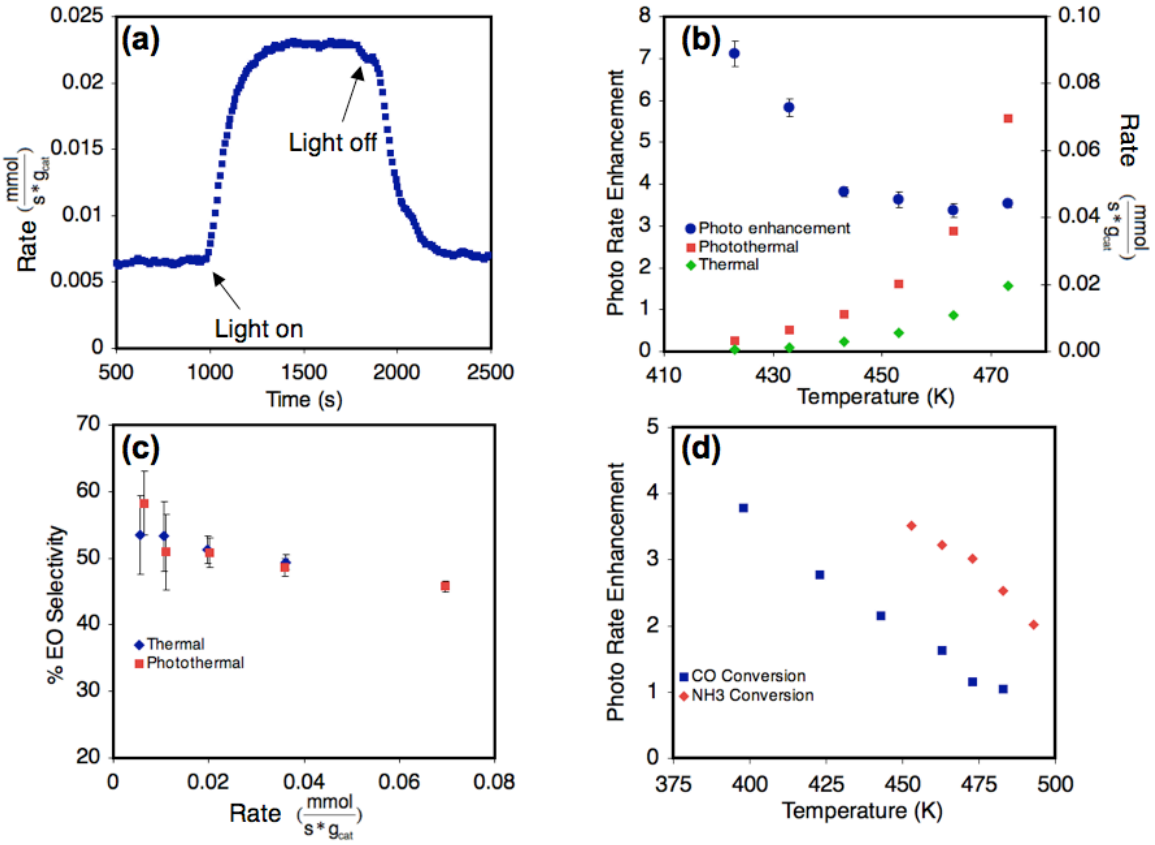

Figure 7.2 Plasmon enhanced oxidation reactions. (a) The rate of ethylene epoxidation at 450 K in the dark and with visible illumination. A significant enhancement in the rate due to visible light illumination is observed. (b) (Left Axis, blue spheres) Rate enhancement, calculated by dividing the rate of photo-thermal by the rate of thermal process, as a function of temperature. (Right axis) black triangles show the rate of thermal ethylene epoxidation and red squares show the rate of photo-thermal epoxidation as a function of temperature. (c) Selectivity to EO for the thermal and photo-thermal processes as a function of reaction rate. The two processes show identical selectivity at a given rate. (d) Rate enhancements, calculated by dividing the rate of photo-thermal by the rate of the pure thermal process, for CO and NH_3 oxidation as a function of temperature. Error bars in the plots represent the standard deviation of the systematic errors in the collection of mass spectrometer data.

performed for CO and NH_3 oxidation reactions on identical Ag catalysts. Figure 7.2(d) shows that the visible light-induced rate enhancements in these reactions were similar to those measured in ethylene epoxidation. Overall, Figure 7.2 shows that the interaction of Ag nanoparticle catalysts with visible light results in a significant increase in the rates of the oxidation reactions on Ag. We observe that illuminated Ag nanoparticle catalysts achieve reaction rates (and the yield of the desired product) comparable to those obtained on the same catalysts operated with only thermal energy input (light off) at up to ~ 40 K lower temperatures. We note that this decrease in operating temperature has a profound effect on catalyst stability.[37] A reduction in operating temperature of only 25 K (representative of typical results) should increase catalyst lifetime by ~10-fold for a photo-thermal compared to a thermal process.

7.5.3 Potential Mechanisms of Photocatalytic Activity

The critical feature of Ag nanostructures that makes them useful in photo-catalysis is that they interact strongly with visible photons through the resonant creation of surface plasmons, see chapter 3.[38,39] Figure 7.3(a) shows the UV-vis extinction spectra for a dilute solution of Ag nanocubes in water. The shape of the extinction spectrum indicates a uniform distribution of particle shape and size. Figure 7.3(a) also shows the diffuse reflectance UV-vis extinction spectra for the same nanostructures deposited on the α-Al_2O_3 support in air, i.e., the catalytically active form of Ag. The spectral broadening and the change in the position of the plasmon resonance peak are attributed to the dense packing of Ag nanocubes on the support and different dielectric constants of water and air.[40] In Figure 7.3(b) we compare the extinction spectra of fresh, activated and

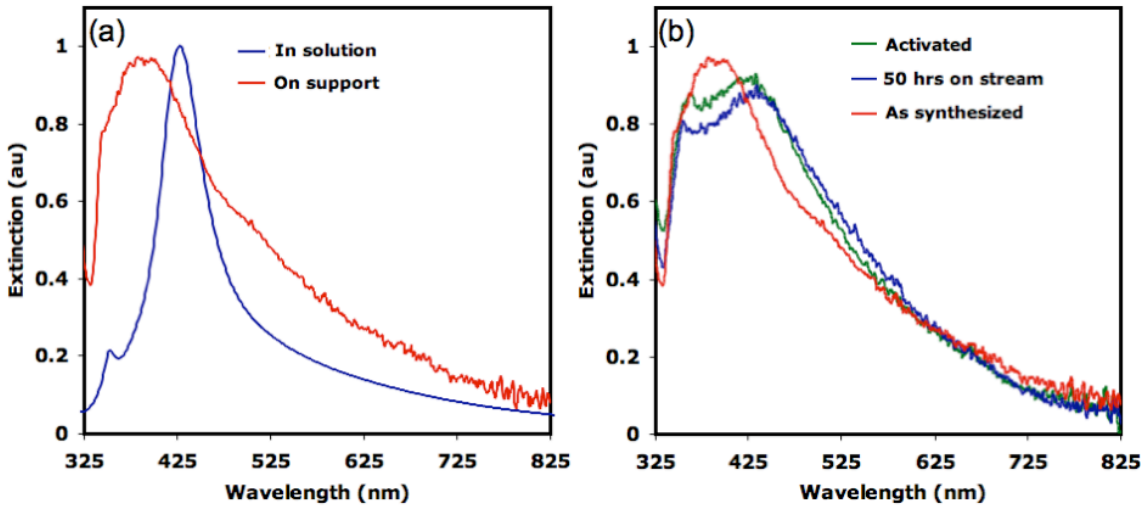

Figure 7.3 Optical properties of Ag nanocubes. (a) Transmission UV-vis extinction spectra of a dilute solution of Ag nanocubes in water and diffuse reflectance UV-vis extinction spectrum of the Ag nanocubes deposited on the Al_2O_3 support in air. The spectra show the strong resonant interaction between Ag nanoparticles and photons in the UV and visible region. (b) Diffuse reflectance UV-vis extinction spectra of Ag nanocubes on Al_2O_3 support for the as-synthesized, activated (after 12 hrs on stream) and used (after 50 hrs on stream) catalysts. Only minor changes in the shape and intensity of the plasmon resonance after 50 hours on stream are observed.

used Ag catalysts. The figure shows that the catalysts exhibit a fairly stable plasmonic activity for 50 hours on stream. Small changes in the shape of the plasmon resonance spectrum of activated and used catalyst are attributed to variations of the local dielectric function due to the removal of the stabilizer (used to control particle growth during synthesis), particle agglomeration and the deposition of carbonaceous organic residue during the course of the reaction.[32] It is also important to note that X-ray photoelectron spectroscopy (XPS) surface analysis as well as Raman and infra-red vibrational spectroscopies on as-prepared, activated, and used catalysts showed that the functioning Ag catalysts are in the metallic state, with no evidence of the formation of Ag oxide, see Figure 7.4.[41,42]

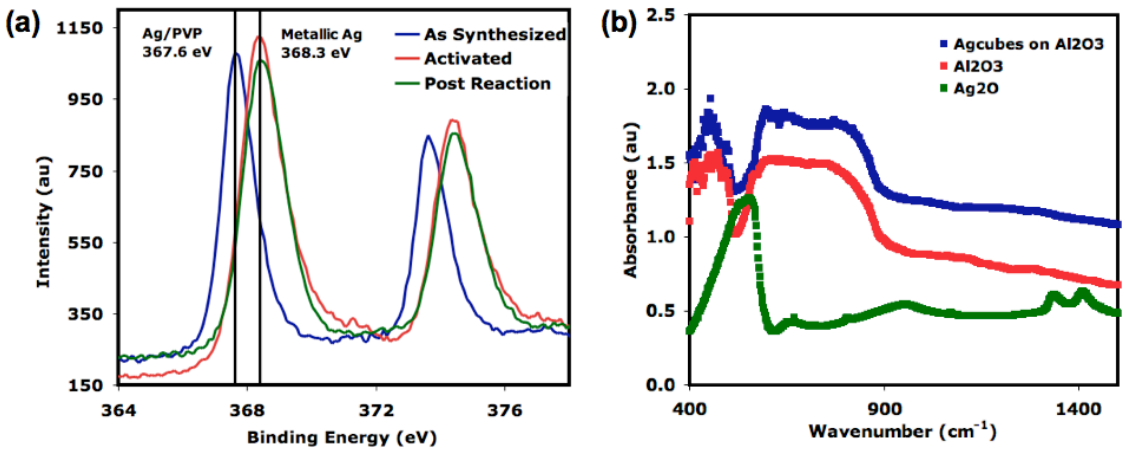

Figure 7.4 Spectroscopic characterization of catalysts. (a) Ag3d core-level spectra from Ag nanocubes on Al_2O_3 support for the as-synthesized, activated (after 12 hrs on stream) and used (after 50 hrs on stream) catalysts. The Ag XPS spectrum for as-synthesized catalysts show peaks characteristic of Ag nanostructures decorated by organic PVP stabilizer (this is typical for the nanostructures grown using a polyol process). The Ag XPS spectra of activated and used catalysts exhibit metallic characteristics. (b) Diffuse reflectance FTIR spectra shows that the used catalyst does not exhibit vibrational modes associated with Ag_2O (mainly the 535 and 1400 cm^{-1} modes).

It has been shown that in an inert environment the excitation of surface plasmons is accompanied by a number of processes including, intense radiative scattering of resonant photons, or the formation of energetic charge carriers (basically energetic electrons).[38,39] In an inert environment, the energetic electrons relax by locally heating the nanostructure. On the other hand, in reactive environments (i.e., the environment probed herein), the surface plasmons could also interact with adsorbates on the surface of the nanostructure by promoting the transfer of energetic electrons to the unoccupied adsorbate states, either directly through the process of chemical interface damping or indirectly via the decay of plasmons into energetic electrons followed by the scattering of these electrons off unpopulated adsorbate states.[22,43] All above-mentioned plasmon relaxation processes have the potential to induce the photo-activity. Intense photon fields could induce direct photo-excitation of adsorbates changing the rates of reaction through uncatalyzed photo-reactions. Local heating of nanoparticles would increase the reaction rate due to the Arrhenius dependence of rate constants on temperature. The transfer of energetic electrons to adsorbates leads to electron-induced surface reactions increasing the overall reaction rates. We discuss below a number of studies establishing that the transfer of energetic electrons to adsorbates is responsible for the observed enhancement in the rates of oxidation reactions on Ag.

7.5.4 Impact of Wavelength on Reaction Rates

Figure 7.5(a) shows normalized photo-rate (constant temperature) as a function of long pass filter wavelength. The long pass filters remove photons with wavelengths below the filter threshold, Figure 7.5(b). The normalized plasmon intensity (a

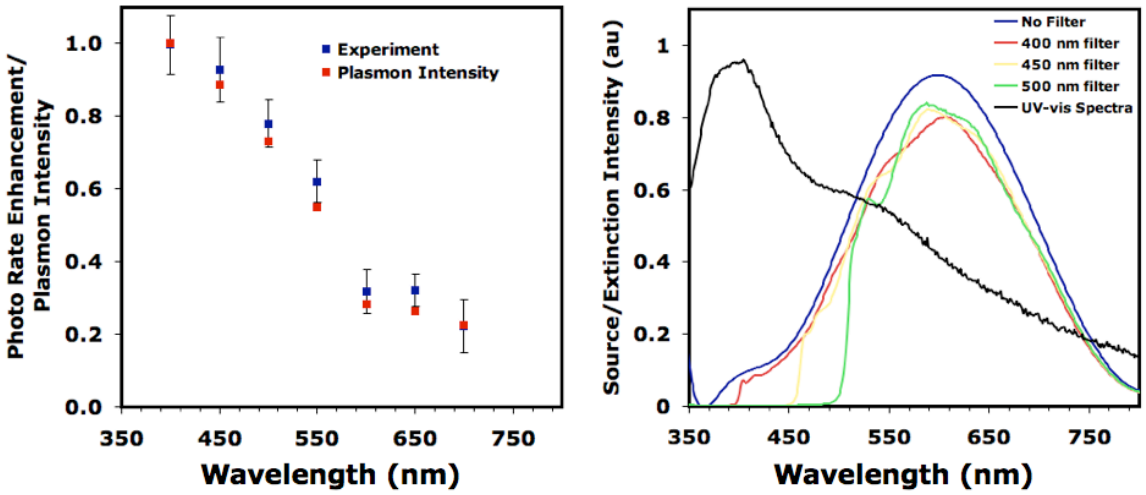

Figure 7.5 Wavelength dependent photothermal ethylene epoxidation. (a) Blue squares represent normalized photo-rate as a function of filter cutoff wavelength measured at T = 470 K. The photo-rate was calculated by subtracting the thermal rate (light off) from the photo-thermal rate (light on) for each filter cutoff wavelength. The photo-rate at each cutoff filter wavelength was normalized by the photo-rate with no filter. Red squares represent the normalized total plasmon intensity as a function of photon cutoff filter wavelength (see text). The figure shows a linear mapping between the normalized photo-rate and total plasmon intensity, indicating that the photoactivity is driven by plasmon excitation. Error bars in the plots represent the standard deviation of the systematic errors in the collection of mass spectrometer data. (b) Spectrum of the light source with no filter, and 400, 450 and 450 nm filters.

measure of the number of excited surface plasmon states) is also shown. This was calculated by multiplying the measured wavelength-dependent source intensity (for each long pass filter, Figure 7.5(b)) by the measured wavelength-dependent extinction spectrum (Figure 7.1(b)) and integrating the product over the wavelength, Equation 1. For example, Figure 7.1(b) shows the overlap between the broadband source (no filters used) and the plasmon resonance spectra as a function of wavelength. By multiplying these curves together and integrating the resulting function over wavelength the plasmon intensity is calculated. The plasmon intensity was normalized to 1 for the source with no filter.

$$\text{plasmon intensity} = \int_{350nm}^{750nm} \text{Extinction spectrum}(\lambda) * \text{Source Intensity}(\lambda)\, d\lambda \qquad (1)$$

The linear mapping between the measured photo rate and the calculated plasmon intensity indicates that the excitation of surface plasmons is responsible for the observed photo-enhancement, and that the plasmons in this energy window can efficiently interact with adsorbates (the mechanisms of energy transfer from plasmons to adsorbates is further discussed below).

7.5.5 Impact of Source Intensity on Photocatalytic Activity

The dependence of the photo-rate on the source intensity was measured by modulating the source intensity between 0 and 250 mW/cm^2. Figure 7.6 shows that there is a linear dependence of the photo-induced rate on the source intensity. This linear dependence is a clear signature of an electron-driven chemical process.[44,45] To illustrate this point, we developed a model to capture the effect of source intensity on the photo-rate in a plasmon heating based mechanism, this is also shown in Figure 7.6. Previous

theoretical and experimental results from literature show that the nanoparticle temperature increases linearly with source intensity for plasmon based heating, equation 2. The rate of thermo-catalytic reactions is known to be proportional to the Arrhenius relation, displaying an exponential dependence of rate on reaction temperature, equation 3. We experimentally measured the E_a of the pure thermal process to be 85 kJ/mol. The experimentally observed rate enhancement at these conditions (T = 450 K), due to illumination with the visible source (250 mW/cm^2), was 2.7. Using the measured E_a and rate enhancement, a temperature increase of 21 K is required to explain the experimental data. The model prediction in Figure 7.6 was obtained by assuming a 21 K increase in temperature at the maximum intensity, 250 mW/cm^2, and assuming a linear increase in temperature with increasing source intensity. The pre-exponenial factor, A, was adjusted such that the rate accurately predicted the experimental rate of the purely thermal process (source intensity = 0). Equation 4 shows the model used to calculate the rate through a

$$\Delta T_{plasmons} = c * I_0 \qquad (2)$$

$$Rate = A * \exp(\frac{-E_a}{RT}) \qquad (3)$$

$$Rate(I_0) = A * \exp(\frac{-E_a}{R(T + c * I_0)}) \qquad (4)$$

plasmonic heating mechanism. $\Delta T_{plasmons}$ is the change in temperature due to plasmonic heating, c is a proportionality constant, and I_0 is the light intensity. The plasmon heating model predicts an exponential dependence of photo rate on temperature, conclusively showing that plasmon heating cannot be responsible for the observed linear dependence of photoactivity on source intensity.

The results in Figures 7.5 and 7.6 clearly show that plasmons are responsible for the observed photoactivity through a first order electron driven process.

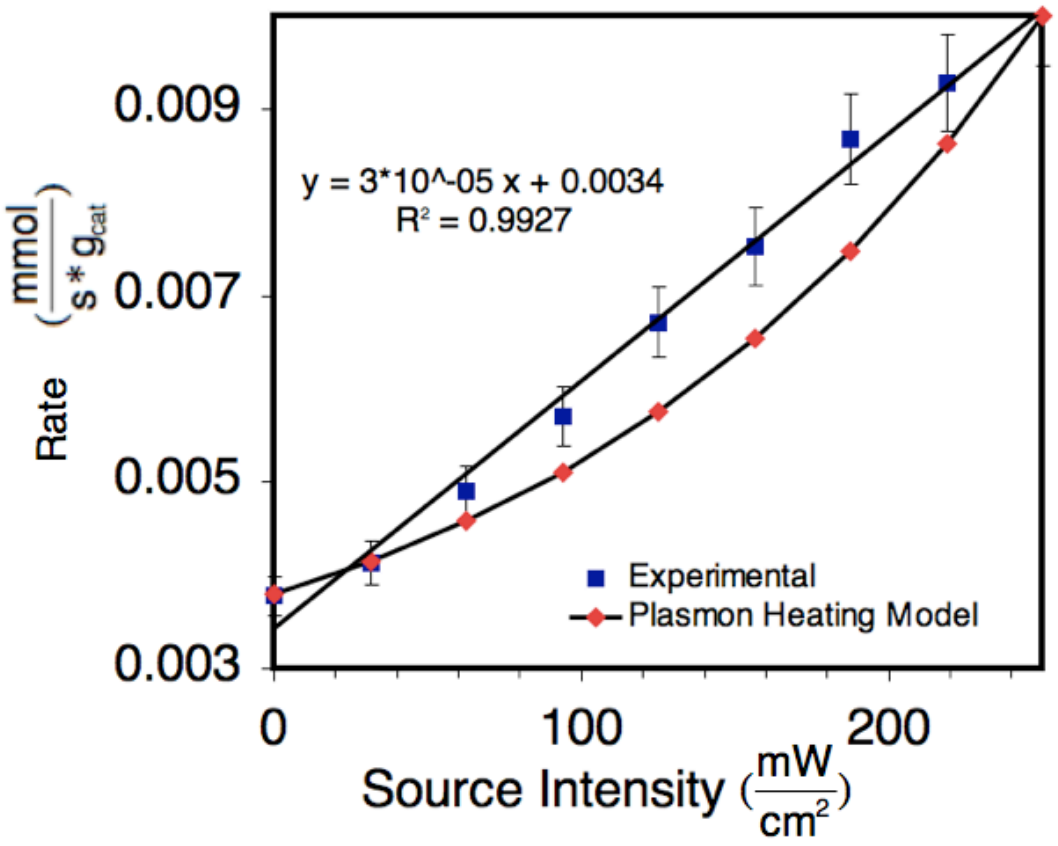

Figure 7.6 Intensity dependent photocatalytic rate. The rate of photothermal (light on) ethylene epoxidation as a function of source intensity. Blue squares are experimental rates and red diamonds are the Arrhenius rates calculated assuming a linear dependence of the light intensity and local nanoparticle temperature (see text).

7.5.6 Isotopic Labeling Studies

Since it has been shown previously that for the oxidation reactions on Ag discussed herein, the dissociation of molecular O_2 on Ag to form adsorbed atomic O controls the reaction rates,[46,47] we hypothesized that energetic electrons accelerate this elementary step. To test this hypothesis we performed kinetic isotope studies comparing the steady-state rates of ethylene epoxidation using unlabeled (O_2^{16}) and labeled (O_2^{18}) oxygen. It has been shown previously that electron-driven elementary surface reactions on metals exhibit larger kinetic isotope effects ($RateO^{16}/RateO^{18}$) than thermal, phonon-driven reactions.[48,49,50] The steady-state rates of the photo-thermal ethylene epoxidation reaction (light on) measured under identical conditions (T = 450 K) using O_2^{18} and O_2^{16} reactants are shown in Figure 7.7. The figure shows that at steady state, the kinetic isotope effect for the photothermal process is 1.19 ± 0.01. In comparison, we measured a kinetic isotope effect of 1.06 ± 0.02 for the thermal (light off) process. The significantly larger kinetic isotope effect for the photo-thermal process, compared to the thermal process, is another signature of an electron driven process.

In addition it is important to note that the thermal kinetic isotope effect is fully consistent with the hypothesis that the activation of O_2 controls the overall reaction rate. In a pure thermal kinetic isotope experiment, where the concentration of O_2^{16} and O_2^{18} are identical, the magnitude of the KIE can be calculated by comparing the rate constants associated with the 2 reactants, equation 5. The difference in the E_a due to isotopic labeling is due only to the change in the zero point energies for the reactant and transition state (involved in the rate limiting step) when moving from O_2^{16} to O_2^{18}. The result of this is that the KIE can be calculated by knowing only the change in the vibrational

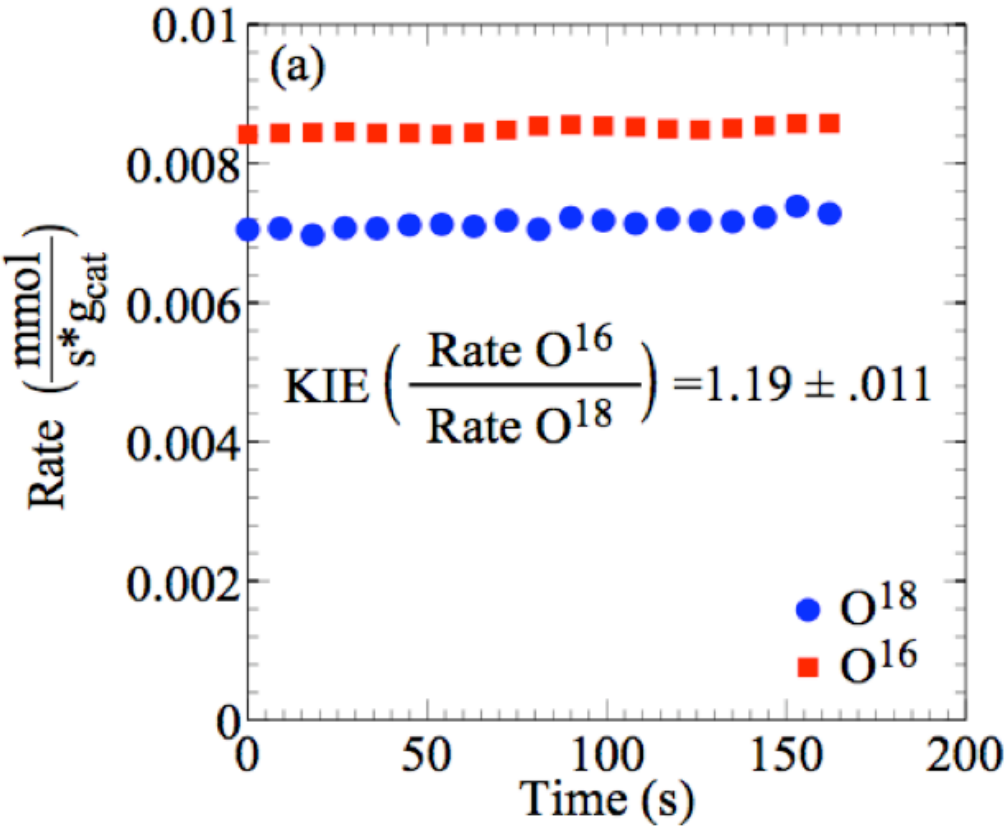

Figure 7.7 Isotope effect in photothermal process. Steady state rate for photo-thermal reaction (light on) measured at T = 450 K for O_2^{16} and O_2^{18} reactants. A large kinetic isotope effect is observed for the photo-thermal process.

frequency of the species involved in the rate-limiting step, equation 6. This means that for different rate limiting steps, if the magnitude of the shift in the vibrational frequency (due to isotopic labeling) is significantly different, then the KIE for each step will be significantly different.

$$KIE = \frac{rate_{O_2^{16}}}{rate_{O_2^{18}}} = \frac{k_{O_2^{16}}[O_2^{16}]}{k_{O_2^{16}}[O_2^{18}]} = \frac{k_{O_2^{16}}}{k_{O_2^{16}}} = \exp(\frac{-(E_{a,O_2^{16}} - E_{a,O_2^{18}})}{k_B T}) \qquad (5)$$

$$KIE = \exp(\frac{-(E_{a,O_2^{16}} - E_{a,O_2^{18}})}{k_B T}) = \exp(\frac{-\frac{1}{2}h(\nu_{O_2^{18}} - \nu_{O_2^{16}})}{k_B T}) \qquad (6)$$

In the context of ethylene epoxidation, we compared the 2 steps that have been suggested to significantly control rate, O—O dissociation and Ag—O bond breaking.[47] Previous electron energy loss spectroscopy measurements have shown that the vibrational frequency associated with the reaction coordinate for the dissociation of molecular O_2 on Ag(100) shifts from 0.084 to 0.080 eV when going from O_2^{16} to O_2^{18}.[51] Similar measurements examining the shift in the Ag—O vibrational frequency show a shift from 0.034 to 0.033 eV when going from O_2^{16} to O_2^{18}.[52] Using equation 6, T = 450 K, and the known shifts in vibrational frequencies, we find that if the rate limiting step for epoxidation is dissociation of molecular O_2 a KIE of 1.053 is expected, whereas if Ag—O bond breaking is the rate limiting step a KIE of 1.013 is expected. By comparing these predictions to the measured value for the pure thermal KIE of 1.06 ± .02 we show conclusively that under our experimental conditions, O_2 dissociation controls the overall rate. This gives us confidence that we can examine the population of the O_2 $2\pi^*$ state by

excited electrons to understand the mechanism of plasmon assisted oxidation reactions on Ag.

7.6 Theoretical Results

The linear dependence of the photo-induced reaction rate on the source intensity Figure 7.6, as well as the large kinetic isotope effect Figure 7.7 indicate that energetic electrons increase the overall reaction rate through a first-order electron-assisted O_2 dissociation process. In the context of the reactions studied herein we suggest that the transfer of an energetic electron from Ag to the antibonding O-O $2\pi^*$ state of molecular O_2 adsorbed on Ag results in the formation of an O_2^- ion (an O_2 molecule with an extra e^- in the $2\pi^*$ state) and facilitates the O_2 dissociation step. DFT calculations show that this antibonding orbital is only partially occupied in the electronic ground state of O_2 adsorbed on Ag, effectively keeping O_2 in the undissociated molecular state at low temperatures. This is illustrated in Figure 7.8(a) where we show the ground state molecular density of states projected on O_2 adsorbed on the Ag(100) surface (this is the dominant surface facet on Ag nanocube catalysts).[32]

To further explore the process of electron transfer from Ag to the O_2 $2\pi^*$ antibonding orbital, in Figure 7.8(b) we show the potential energy surfaces for O_2 and O_2^- (where an e^- was removed from the Fermi level of Ag and placed in the O_2 $2\pi^*$ state) adsorbed on Ag(100). The potential energy surface for ground state O_2 on Ag(100) was calculated using DFT. The potential energy surface for O_2^- on Ag(100) was calculated using linear expansion delta self-consistent field extension of DFT (ΔSCF-DFT). The approach has been used earlier to study electron-driven processes on metals.[27,28] It has

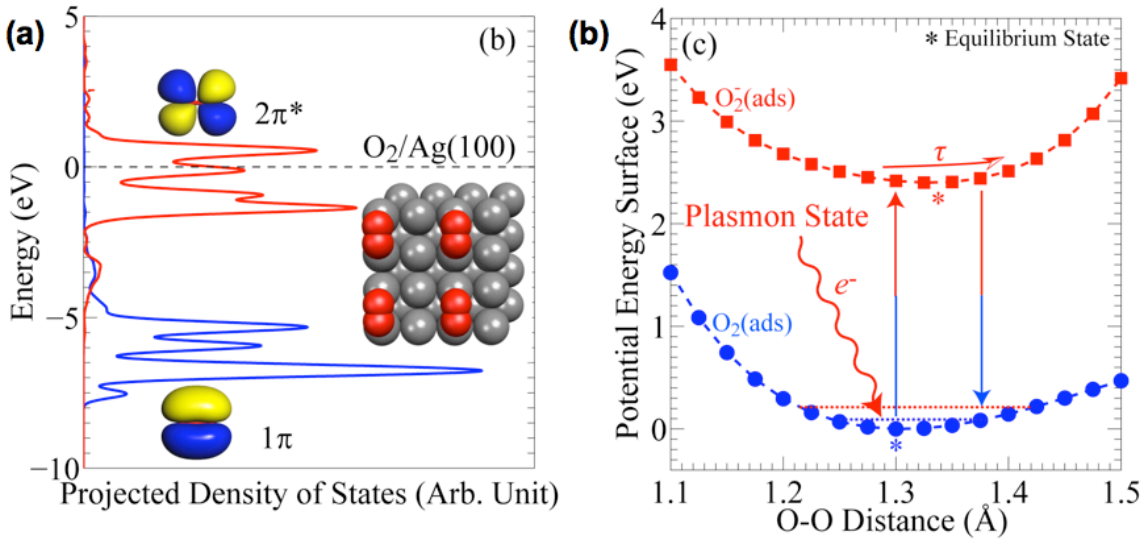

Figure 7.8 Theoretical analysis of photocatalytic O_2 dissociation on Ag. (a) Molecular density of states projected on O_2 adsorbed in the lowest energy configuration on the Ag(100) surface calculated using density functional theory. The Fermi level is depicted by the horizontal line at Energy = 0 eV. Inserts show the 1π bonding and 2π* antibonding orbital of adsorbed O_2. The inset shows the model system used in the calculations, the red spheres are oxygen atoms and gray spheres are silver atoms. (b) Density functional theory calculated potential energy surface for O_2 and O_2^- on Ag(100). Excitation of Ag surface plasmons allows for the transfer of an excited electron to O_2 forming O_2^-. The O_2 becomes negatively charged and nuclear motion is induced along the O_2^- potential energy surface.

been found to accurately reproduce experimentally measured inverse photo-emission spectroscopy data for molecules chemisorbed on metallic surfaces. [27,28]

There are a number of important results of the calculations shown in Figure 7.8(b). First, it is shown that the energy required to populate the antibonding orbital of O_2 adsorbed on Ag is ~ 2.4 eV. This is the vertical energy difference between the charged O_2^- state potential energy surface (with an extra electron occupying the anti-bonding O-O $2\pi^*$ state) and the minimum of the ground state potential energy surface (O_2 on Ag(100)). This is not equal to the energy of antibonding orbital in the ground state calculation; the significant final state-effect causes the energy to be substantially different. This energy matches well the energy of Ag surface plasmons and consequently the energy of energetic electrons formed in the process of plasmon excitation on the Ag nanostructures (see Figure 7.3(a)), implying that an efficient resonant electron transfer to the antibonding state is possible. The calculations in Figure 7.8(b) also allow us to postulate the underlying mechanism that governs the observed light-induced rate enhancement. When energetic electrons are scattered into the antibonding orbital of adsorbed O_2, the O-O bond is stretched, i.e., the lowest energy configuration for the charged O_2^- state is characterized by a larger O-O bond distance. We note that previous measurements showed that the lifetime of excited molecules on metal surfaces is ~5-10 fs,[53,54] which is sufficient to induce nuclear motion along the O-O bond in response to the population of the O_2 $2\pi^*$ orbital, but likely not sufficient to induce dissociation while the O_2 is on the excited state potential energy surface. The decay of the electron back to the metal results in the collapse of O_2 into a vibrationally excited state on the ground state potential energy surface. Essentially, the process of electron transfer to the anibonding orbital and back-

transfer to the metal deposits energy into the O-O vibrational mode. It has been shown previously that the average time required for vibrationally excited adsorbates to dissipate vibrational energy on metal surfaces is typically on the order of picoseconds.[55] Since the oscillation time for the vibration of adsorbed O_2 is ~ 50 fs, it is reasonable to assume that the molecule has enough time to react before this vibrational energy is dissipated. The net effect of the light-induced electron transfer process is that the O_2 adsorbate is activated at a reduced temperature as compared to thermal (light off) process, see Figure 7.9. Finally, the two potential energy surfaces in Figure 7.8(b) can also help us understand the observed kinetic isotope effect. The excited electron spends equal time on both O_2 isotopes. Due to the difference in the mass of the two isotopes, the O^{16} isotope is accelerated more than the O^{18} isotope on the excited O_2^- potential energy surface and therefore the O^{16}-O^{16} bond is stretched further than the O^{18}-O^{18} bond. Because the electron excitation induces a larger elongation of the O^{16}-O^{16} bond compared to O^{18}-O^{18}, when the electron decays into the Ag substrate and O_2 returns to the ground state potential energy surface, the vibrational energy associated with $O_2{}^{16}$ isotope is larger and therefore it is easier to activate $O_2{}^{16}$ than $O_2{}^{18}$.

7.7 Conclusions and Outlook

In conclusion, our work demonstrates that metallic Ag nanostructures, characterized by the resonant formation of surface plasmons, can yield chemically useful energetic electrons when irradiated with continuous wave low intensity visible light. These electrons can be used in tandem with thermal energy to drive commercially relevant catalytic chemical transformations at viable rates, through combined phonon-

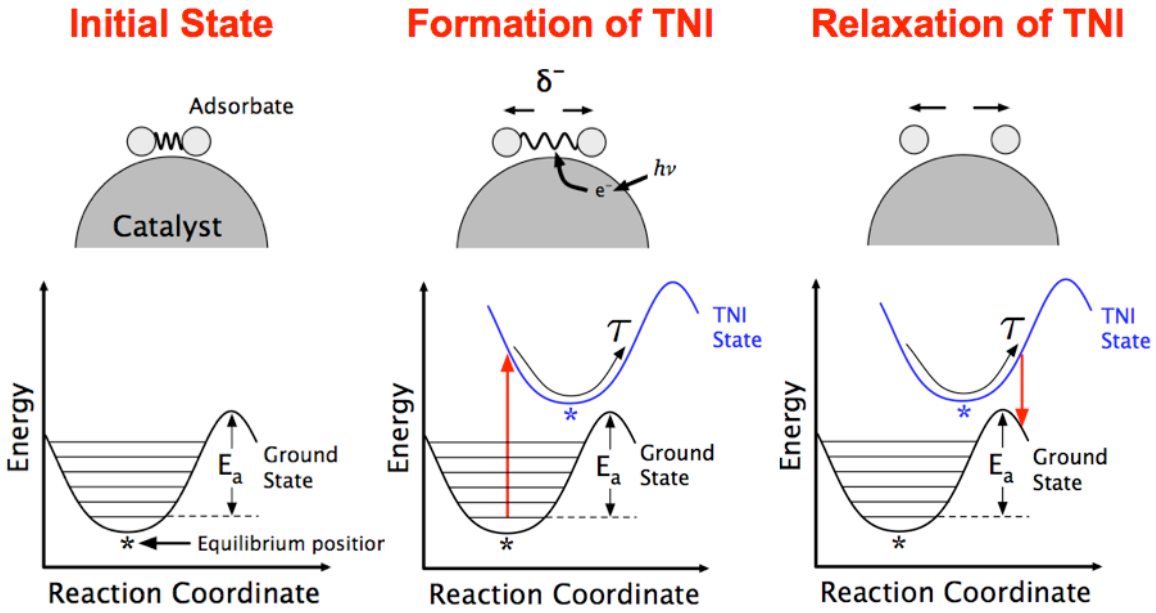

Figure 7.9 Mechanism of photothermal O_2 dissociation. Step 1: The adsorbate is initially on its ground state potential energy surface. Step 2: The electron scattering process produces a transient negative ion (TNI). The adsorbate travels on the TNI potential energy surface, gaining energy along the reaction coordinate. Step 3: After a short lifetime, τ, the electron decays back to the metal Fermi level and the adsorbate returns to the ground state potential energy surface with increased vibrational energy. If the energy transfer is sufficient to overcome the activation barrier, the reaction will occur.

electron driven elementary steps, at significantly reduced temperatures compared to pure thermal processes. The resonant nature of electron transfer to adsorbate antibonding orbitals suggests that by tuning the energy of the excited plasmons (controlling nanoparticle size and shape), these materials might be able to selectively activate targeted chemical transformations. We anticipate that the observations are not unique to Ag, and any other metal that support intense plasmons (e.g., Au, Pt, Pd) should exhibit similar behavior under resonance conditions.[56,57]

There are a few issues raised by the studies that deserve further attention. For example, we showed that in the temperature and light intensity regimes probed herein, there was a minimum temperature required to achieve appreciable rates. One effect of the thermal bath is to push vibrationally excited O_2 molecules over the dissociation activation barrier in the rate limiting elementary step, Figure 7.9. In addition, the thermal bath could also play a role in activating elementary steps subsequent to the activation of O_2, i.e., the steps associated with the product formation and removal that might require exclusively thermal activation. These steps will become more relevant at kinetic regimes that are not dominated by the dissociation of O_2, mainly at lower temperatures. Also, recent theoretical contributions have showed that the probability of the transfer of an energetic electron to an adsorbate is higher for vibrational excited adsorbates compared to those in the ground state. At high temperatures where thermal energy is sufficient to induce a significant population of vibrationally excited states, this effect will play a role in the electron transfer process.[48] Another issue is related to the nature of electron transfer from plasmonic nanostructures to adsorbates. While our studies showed that surface plasmons are responsible for the transfer of energetic electrons from metal to the

adsorbate, further mechanistic analysis is required to address whether this process is mediated by the formation of energetic electrons on the metal surface and their subsequent transfer to the adsorbate, or it is a consequence of the direct interaction of surface plasmons with adsorbates.[22,39] Finally, it is also important to note that the interaction of excited plasmons with adsorbates will be affected by the spatially non-homogeneous distribution of plasmons on the Ag nanostructures. In this regard, "hot spots" (regions with highly intense plasmon fields between multiple plasmonic partices) might play the critical role.

7.8 References

[1] B. Hammer, J.K. Nørskov, *Nature*, **376**, 238, 1995.

[2] A. Wittstock, V. Zielasek, J. Biener, C.M. Friend, M. Baumer, *Science*, **327**, 319, 2010.

[3] C.T. Campbell, S.C. Parker, D.E. Starr, *Science,* **298**, 811, 2002.

[4] Y. Lei, *et al., Science*, **328**, 224, 2010.

[5] J. Lu, *et al., J. Catal.*, **232**, 85, 2005.

[6] N. Tian, Z. Zhou, S. Sun, Y. Ding, Z.L. Wang, *Science,* **316** ,732, 2007.

[7] M. Chen, D. Kumar, C.W. Yi, D.W. Goodman, *Science,* **310**, 291, 2005.

[8] F. Studt, F. Abild-Pedersen, T. Bligaard, R.Z. Sørensen, C.H. Christensen, J.K. Nørskov, *Science*, **320**, 1320, 2008.

[9] P. Sabatier, *Berichte der Deutschen Chem. Gesellschaft* **44,** 1984, 1911.

[10] S. Link, M.A. El-Sayed, *J. Phys. Chem. B*, **103**, 4214, 1999.

[11] P. Christopher, D.B. Ingram, S. Linic, *J. Phys. Chem. C,* **114**, 9173, 2010.

[12] R. Jin, *et al., Science*, **294**, 1901, 2001.

[13] R. Jin, *et al., Nature,* **425**, 487, 2003.

[14] J.R. Adleman, D.A. Boyd, D.G. Goodwin, D. Psaltis, *Nano Lett.* **9**, 4417, 2009.

[15] D.B. Ingram, S. Linic, *J. Am. Chem. Soc.,* **133**, 5202, 2011.

[16] H. Awazu, *et al., J. Am. Chem. Soc.*, **130**, 1676, 2008.

[17] *Laser Spectroscopy and Photochemistry on Metal Surfaces;*H.-L. Dai, W. Ho, Eds.; World Scientific: Singapore, 1995.

[18] S.A. Buntin, L.J. Richter, R.R. Cavanagh, D.S. King, *Phys. Rev. Lett.,* **61,** 1321, 1988.

[19] J.A. Prybyla, T.F. Heinz, J.A. Misewich, M.M.T. Loy, J.H. Glownia, *Phys. Rev. Lett.*, **64**, 1537, 1990.

[20] J.W. Gadzuk, *Phys. Rev. Lett.*, **76**, 4234, 1996.

[21] T.-H. Her, R.J. Finlay, C. Wu, E. Mazur, *J. Chem. Phys.*, **108**, 8595, 1998.

[22] D. Mulugeta, K.H. Kim, K. Watanabe, D. Menzel, **101**, 146103, 2008.

[23] S.R. Hatch, X.-Y. Zhu, J.M. White, A. Campion, *J. Phys. Chem.,* **95**, 1759, 1991.

[24] S.K. So, R. Franchy, W. Ho, *J. Chem. Phys.,* **95**, 1385, 1991.

[25] W.D. Mieher, W. Ho, *J. Chem. Phys.*, **99**, 9279, 1993.

[26] J.J. Mortensen, L.B. Hansen, K.W. Jacobsen, *Phys. Rev. B,* **71**, 035109, 2005.

[27] J. Gavnholt, T. Olsen, M. Engelund, J. Shiøtz, *Phys. Rev. B*, **78**, 075441, 2008.

[28] T. Olsen, J. Gavnholt, J. Schiøtz, *Phys. Rev. B,* **79**, 035403, 2009.

[29] Z. Qu, M. Cheng, W. Huang, X., Bao, *J. Catal.*, **229**, 446, 2005.

[30] L. Gang, B.G. Anderson, J. van Grondelle, R.A. van Santen, *Appl. Catal. B*, **40**, 101, 2003.

[31] S.K. So, R. Franchy, W. Ho, *J. Chem. Phys.,* **95**, 1385, 1991.

[32] P. Christopher, S. Linic, *ChemCatChem*, **2**, 78, 2010.

[33] P. Christopher, S. Linic,. *J. Am. Chem. Soc.*, **130**, 11264, 2008.

[34] D.W. Park, G. Gau, *J. Catal.*, **105**, 81, 1987.

[35] A. Gavriilidis, A. Varma, *AICHE Journal*, **38**, 291, 1992.

[36] C.T. Campbell, M.T. Paffett, *Surface Science*, **139**, 396, 1984.

[37] P. Wynblatt, N. Gjostein, *Acta Metallurgica,* **24**, 1165-1174, 1976.

[38] L. Brus, *Acc. Chem. Res.,* **41**, 1742, 2008.

[39] P.K. Jain, X. Huang, I.H. El-Sayed, M.A. El-Sayed, *Acc. Chem. Res.*, **41**, 1578, 2008.

[40] E. Prodan, C. Radloff, N.J. Halas, P. Norlander, *Science*, **302**, 419, 2003.

[41] V.I. Bukhtiyarov, *et al. Phys. Rev. B*, **67**, 235422, 2003.

[42] V.I. Bukhtiyarov, *et al. J. Catal.,* **238**, 260, 2006.

[43] K. Watanabe, D. Menzel, N. Nilius, H.J. Freund, *Chem. Rev.*, **106**, 4301, 2006.

[44] J.M. Herrmann, *Catal. Today*, **53**, 115, 1999.

[45] Z. Zhang, J.T. Yates, *J. Phys. Chem. C*, **114**, 3098, 2010.

[46] C. Stegelmann, N.C. Schiødt, C.T. Campbell, P. Stolze, *J. Catal.*, **221**, 630, 2004.

[47] S. Linic, M.A. Barteau, *J. Catal.,* **214**, 200, 2003.

[48] M. Bonn, *et al., Science*, **285**, 1042, 1999.

[49] S. Funk, *et. al., J. Chem. Phys.*, **112**, 9888, 2000.

[50] D.N. Denzler, C. Frischkorn, C. Hess, M. Wolf, G. Ertl, *Phys. Rev. Lett.*, **91**, 226102, 2003.

[51] L. Vattuone, P. Gambardella, U. Valbusa, M. Rocca, *Surf. Sci.*, **377**, 671, 1997.

[52] F. Buatier de Mongeot, A. Cupolillo, M. Rocca, U. Valbusa, *Chem. Phys. Lett.*, **302**, 302, 1999.

[53] L. Bartels, *et. al., Phys. Rev. Lett.*, **80**, 2004, 1998.

[54] J.A. Misewich, T.F. Heinz, D.M. Newns, *Phys. Rev. Lett.*, **68**, 3737, 1992.

[55] J.D. Beckerle, *et al. Phys. Rev. Lett.*, **64**, 2090, 1990.

[56] C. Langhammer, Z. Yuan, I. Zoric, B. Kasemo, *Nano Lett.,* **6**, 833, 2006.

[57] C. Langhammer, B. Kasemo, I. Zoric, *J. Chem. Phys.,* **126**, 194702, 2007.

Chapter 8

Plasmon Driven Multi-Electron Photocatalytic Processes

8.1 Summary

In this Chapter we show that the excitation of surface plasmons on Ag nanostructures under ethylene epoxidation conditions, by relatively low intensity visible photon illumination (300-1000 mW/cm^2), results in a highly efficient multi-electron driven photocatalytic process. This shows the first observation of a regime shift from linear to non-linear dependence of photo-rate on intensity, driven by a low intensity continuous wave source. In addition, the excellent thermo-catalytic features of metallic nanoparticles allow for an effective coupling of thermal and photonic stimuli to produce a previously unreported exponential dependence of photocatalytic quantum efficiency on operating temperature. We provide a first-principles based model, which captures the effect of intensity and temperature on the process efficiency.

8.2 Introduction

The utilization of solar energy for driving chemical reactions has relied primarily on the development on photocatalytic semiconductor materials that efficiently convert solar energy into energetic charge carriers (electron/hole pairs) that drive surface chemical reactions.[1,2] Semiconductor photocatalysts exhibit low rates and limited versatility for photocatalytic reactions due to the diffuse nature of the solar photon flux, large band gaps associated with photocatalytcially active materials, and poor inherent surface catalytic properties. Many approaches have been utilized to combat these inherent limitations. Band gap engineering of semiconductors to enhance the efficiency of visible light absorption has received significant attention, but the development of materials that can interact with a majority of the solar spectrum is still limited.[3,4] Composite metal/semiconductor photocatalysts have also been developed in attempt to utilize the excellent catalytic properties of metallic nanoparticles in tandem with the light absorption properties of the semiconductor.[5] In Chapter 6 we introduced another approach of utilizing plasmonic nanoparticles to concentrate light at semiconductor surfaces.[6,7,8] While these approaches have enjoyed some success, state-of-the art photocatalytic materials still exhibit prohibitively low catalytic rates and very limited variety of possible chemical transofmrations, for the development of viable commercial photocatalytic processes.

As opposed to semiconductor surfaces, metallic surfaces have exclusively been used as thermocatalysts. Metal particles are extremely versatile in their ability to catalyze important industrial chemical reactions, but due to their electronic structure (lack of a band gap) have not been applied directly as photocatalysts.[9] Photocatalytic processes on

extended metal surfaces are extremely inefficient due to low rates of photo-induced energetic charge carrier production and very short energetic charge carrier lifetimes.[10] When confined to nanometer scales, coinage metals exhibit strong interactions with photons in the UV and visible region through the excitation of surface plasmons, which are not observed on extended metal surfaces.[11,12] A major consequence of the excitation of surface plasmons is formation of strong electromagnetic fields near the nanoparticls surface that enhance the strength of an incoming field many orders of magnitude. In Chapter 7 we exploited the enhanced interaction of visible light with Ag nanoparticles to show that the rate of catalytic oxidation reactions on Ag nanostructures were significantly enhanced when the catalyst illuminated with low intensity (<250 mW/cm^2) visible light.[13] Based on a linear dependence of the photocatalytic rate on source intensity, an enhanced kinetic isotope effect and density functional theory calculations it was proposed that the photo-induced rate enhancement was a consequence of a single electron process. The molecular mechanism proposed involved the scattering of energetic electrons, created due to the excitation of surface plasmons, from partially unpopulated $2pi^*$ states of adsorbed O_2 on Ag surface, thereby accelerating the rate limiting O_2 dissociation step, resulting in an overall enhancement in the rate of the studied oxidation reactions.

In this Chapter we show that the excitation of surface plasmons on Ag nanostructures by relatively low intensity visible photon illumination (300-1000 mW/cm^2) results in a highly efficient multi-electron driven photocatalytic process. This shows the first observation of a regime shift from linear to non-linear dependence of photo-rate on intensity, driven by a low intensity continuous wave source. In addition, the excellent thermo-catalytic features of metallic nanoparticles allow for an effective

coupling of thermal and photonic stimuli to produce a previously unreported exponential dependence of photocatalytic quantum efficiency on operating temperature. We provide a first-principles based model, which captures the effect of intensity and temperature on the process efficiency. By comparing the experimental and theoretical results, we conclude that the intense near-field light concentration induced by the excitation of surface plasmons plays a crucial role in allowing the highly efficient multi-electron process at low source intensity.

8.3 Experimental and Theoretical Methods

8.3.1 Ag Nanoparticle Synthesis and Catalyst Preparation

5 mL Ethylene Glycol (J.T. Baker item 9300. Purity is very important. Only lots with Cl concentration below 0.1 PPM and Fe concentration below 0.01 PPM should be used in this synthesis) and a magnetic stir bar are added to a 20 mL vial and submerged in an oil bath heated to 140-145^{0}C on a stirring hotplate. The cap to the vial should be loosely placed on top to allow boiling off of vapors from any contaminant solvent. Allow 1 hr. for heating. After 1 hr of heating, 3 other solutions should be prepared. The first solution is 6 mL of 0.1M $AgNO_3$ (99% purity, Sigma Aldrich cat. No. 209139) in ethylene glycol. The second solution is 0.15M (in terms of repeating unit) Polyvinylpyrrolidone (PVP) (55,000 M.W. Sigma Aldrich cat. No. 856568) in 6 mL ethylene glycol, once again the solution should be shaken into solution. Lastly a stock solution of 30mM HCl in ethylene glycol should be prepared and can be used up to a month for separate synthesis. 100 μL of the 30mM HCl solution is added to the hot ethylene glycol. Allow 5-10 minutes for this solution to mix. 3 mL of $AgNO_3$ and PVP

solutions are added to the heated vial using a syringe pump at a rate of 0.75 mL/min. At this point the cap should be loosely placed back on the vial. This solution should then be allowed to react for a period of about 24 hrs. After 24 hours the cap on the vial can be tightened such that the vial becomes airtight. This procedure produces cubes of ~60-70nm edge length. The cubes were washed by centrifugation in acetone 5 times and re-dispersed in 5 mL of ethanol.

100 mg of alpha-Al_2O_3 was added to the Ag nanoparticle (0.025g of Ag) solution, and sonicated for 1 hr. The solution was dried, and all Ag nanoparticles adsorbed to the Al_2O_3 surface. This produced a 20% wt Ag nanocube on Al_2O_3 catalyst. The alpha-Al_2O_3 (Alfa Aesar # 42571) support is 5-6 m^2/g, which resulted in about 20% surface coverage of Ag nanocubes on the Al_2O_3 Support.

8.3.2 Reactor Setup

The reactions were carried out in a vertically oriented temperature-controlled packed bed flow reactor with a 1 cm^2 SiO_2 window to allow visible light illumination. The catalyst bed was 3 mm deep consisting of a 2.5 mm layer of inert SiO_2 particles with an additional 0.5 mm layer of catalyst deposited on top of the SiO_2. The catalyst was pretreated in 20 standard cubic centimeters (sccm) O_2 and 60 sccm N_2 for 2 hours at 220 ^oC at atmospheric pressure prior to starting any of the reactions. After the pre-treatment period 20 sccm of ethylene was introduced to the catalyst along with 20 sccm O_2 and 60 sccm N_2 and the reaction was allowed to reach steady state at 220 ^oC overnight. All products were quantified online using quadrupole mass spectrometry (MS) and gas chromatography (GC). Both analyses produced consistent results for activity and

selectivity for all reactions. The rates reported in the manuscript were calculated using the rate of product formation. The GC used is a Varian CP 3800 equipped with 2 TCD's and an FID detector. The MS is an Extorr XT200 operating at 10^{-6} Torr. The visible light source is a Dolan-Jenner Fiber-Lite 180 halogen light that produces 1000 mW/cm^2 at the catalyst surface at maximum intensity. The intensity was varied by manipulating the power provided to the light source and was calibrated using a UV intensity meter and an Avantes 2048 CCD spectrophotometer.

8.3.3 Isotopic Labeling Experiments

The measurements were performed at constant temperatures, using O_2^{18} (99% Sigma Aldrich 602892). The gas composition was 10 sccm O_2, 20 sccm ethylene, 70 sccm N_2. The kinetic isotope effect (KIE) was calculated by comparing the reaction rates with O_2^{16} and O_2^{18} reactants. Steady state conditions were reached 15 minutes after switching from O_2^{16} to O_2^{18}. The conditions were chosen such that the KIE across the linear and non-linear regimes could be probed, and the temperature was varied such that the rate with O_2^{16} was constant for all conditions.

8.3.4 Theoretical Methods

Density functional theory calculations were performed using the GPAW code, a real-space grid-based DFT implementation with the projector-augmented wave method.[14] The exchange-correlation interaction was approximated using the revised Perdew-Burke-Ernzerhof (RPBE) functional. The Ag(100) surface was modeled by a 2×2×3 slab with 10 Å of vacuum space. Oxygen molecule was adsorbed parallel to the Ag-Ag bridge, which

was found to be most stable adsorption configuration of the O_2/Ag(100) system. The O_2 adsorbate and top two layers of the slab were allowed to relax until the force on all atoms was converged to less than .05 eV/Å.

The ground state and the excited state potential energy surface of O_2 has been mapped out in terms of the internal stretch of O-O bond using 18 irreducible k-points and a grid spacing of 0.2 Å. The linear-expansion Delta Self-Consistent Field (ΔSCF-DFT) method implemented in GPAW has been used to calculate the energetic of the electron excitation from the Fermi level to the O_2 $2\pi^*$.[15,16]

8.4 Experimental Results

8.4.1 Observation of Regime Transition

The experiments utilize a well-defined system of ethylene epoxidation, which is a crucial industrial process that is performed exclusively over heterogeneous Ag catalysts, and has been discussed in detail in Chapters 4,5 and 7.[13,17,18] The catalyst used in these studies was a 20% wt loading of 75 nm edge-length Ag nanocubes on alpha-Al_2O_3 support particles. Reactions were carried out in a vertically oriented packed-bed reactor that allowed for catalyst illumination and control of the bed temperature. All products were monitored on stream using a gas chromatograph and mass spectrometer. The reactor setup and catalysts were identical to those described in Chapter 7. The catalyst was illuminated using a broadband visible light source, with peak intensity at 590 nm, a minimum wavelength of 380 nm, and a variable intensity between 75 and 920 mW/cm^2.

Figure 8.1(a) shows the rate of photocatalytic ethylene epoxidation as a function of source intensity, at various temperatures. The photocatalytic rate is defined as the rate of the photo-thermal process (light and heat) minus the rate of the pure thermal process.

The figure shows that regardless of operating temperature the photocatalytic rate dependence on intensity exhibits superlinear, power-law behavior above ~300 mW/cm^2 (ie. Rate $\propto$ Intensity ^{n}, with n >1). Figure 8.1(b) shows the measured power law exponent as a function of temperature and intensity. The figure shows constant first order power law behavior at low intensity, <300 mW/cm^2, followed by a sharp increase in the measured intensity as the regime shift begins. At the lowest temperatures (373 and 398 K) and highest intensity (920 mW/cm^2) the magnitude of the power law exponent reaches a maximum value of n = 3.5. The rate of ethylene epoxidation at 373 K is enhanced ~100 fold, compared to the pure thermal rate, when illuminated with a source intensity of 920 mW/cm^2. As a result of this huge rate enhancement from catalyst illumination the operating temperature of the catalyst can be reduced 100 K, compared to the pure thermal process, while still maintaining the same ethylene oxide production rate.

Figure 8.1(c) shows the quantum efficiencies (QE) calculated from the data shown in Figure 8.1(a). QE is defined as the rate of ethylene oxide production in the photocatalytic process divided by the rate of photon impingement on the sample. The figure shows that in the linear regime (ie. < 300 mW/cm^2) the measured quantum efficiency is constant at all temperatures. The onset of the transition to the super linear regime is accompanied by an increase in the QE, this is a characteristic signature of a multi-electron driven process.[19] The QE reaches a maximum value of 61% at high temperature and source intensity (T = 473 K, I =355 mW/cm^2). The reported QE's are extremely high compared to typically reported QE's for photocatalytic process on metal surfaces driven by visible photons.[20,21] Figure 8.1(a)-(c) show plasmonic Ag nanostructures

exhibit a regime transition from a linear to superlinear catalytic process for producing ethylene oxide with a low intensity continuous wave illumination source.

Previous surface science experiments utilizing femtosecond laser excitation sources to induce chemical transformations at surfaces have shown an enhanced kinetic isotope effect, compared to a pure thermal process, is a defining signature of an electron driven process.[22,23] We performed steady state kinetic isotope studies, by measuring the change in the reaction rate when switching from O_2^{16} to O_2^{18}. The steady-state KIE were measured at four different intensities and for the pure thermal process. The temperatures were chosen such that the rate using O_2^{16} was identical for the thermal and photothermal reactions; that is as the intensity was increased, the temperature was decreased to keep a constant rate for all conditions. Figure 8.1(d) shows the measured KIE as a function of source intensity. In addition the KIE reported in chapter 7, at I= 250 mW/cm^2 and T = 450 K, is also shown.[13] The plots shows that the KIE continues to increase, over the previously measured value in the linear regime, reaching a maximum measured value of 1.49 +-0.09 at I =800 mW/cm^2. The correlation between the KIE and the source intensity is direct evidence that the super-linear photo-catalytic reaction is an electron driven catalytic process.

The only previous observation of a regime transition from a linear to super-linear photocatalytic process on a metal surface, was reported for the electron driven desorption of O_2 from a Pt(111) single crystal using an extremely intense femtosecond laser.[19] Any attempts to induce electron-driven desorption or dissociation of adsorbates on metal surfaces with a less intense photon flux, than provided by a femtosecond laser, has resulted in a linear dependence of yield on intensity. The regime transition from a linear

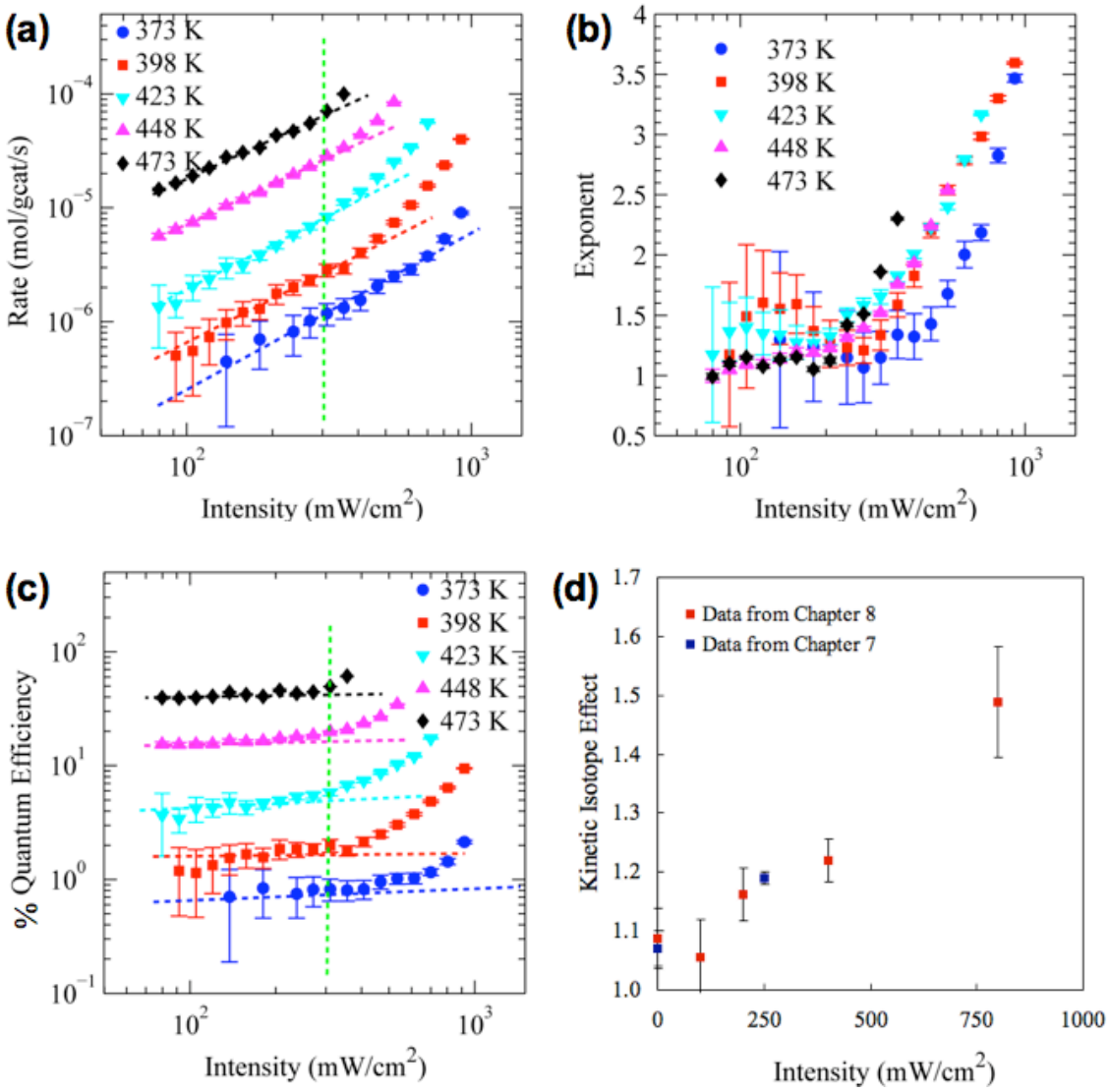

Figure 8.1 Regime transition from linear to superlinear photocatalytic process. (a) The figure shows the photocatalytic rate (total rate minus the rate of the thermal reaction at a given temperature) as a function of intensity for various temperatures. The vertical green line at 300 mW/cm^2 indicates the location of the regime transition. (b) The figure shows the measured exponent from the data in Figure 8.1(a) as a function of intensity. The exponent was calculated by averaging the slope of the log-log plot over 3 data points. (c) This figure shows the % quantum efficiency as a function of intensity for the data measured in Figure 8.1(a). (d) This figure shows the measured kinetic isotope effect (KIE) as a function of source intensity. The data in red are the measurements from this chapter and the data in blue are the measurements from the previous chapter.

to superlinear rate dependence on intensity has typically been explained by the transition from a single to a multi-electron driven catalytic process, this is discussed in more detail below. The massive difference in the intensity required to induce the regime transition (10^{11} vs. 10^{2} photons/site/s)[19], when comparing the single crystal metal surfaces and on the plasmonic nanostructures discussed in this chapter, shows the exceptional properties of excited surface plasmons for concentrating photonic stimuli to efficiently drive photocatalytic processes on metal surfaces.

8.4.2 The Effect of Temperature

In addition to the direct observation of a regime transition from a linear to a superlinear electron driven catalytic process, the data in Figure 8.1 also shows that the rate and QE is significantly enhanced with increasing temperature. In the linear regime the QE is enhanced 50 fold, from 0.75% to 40 %, as the temperature is increased from 373 to 473 K, Figure 8.1(c). To further understand the effect of temperature on the photocatalytic process, the Log of photocatalytic rate and QE are plotted as a function of temperature, at various source intensities, and shown in Figure 8.2(a) and (b). The linear relationships in Figure 8.2 shows that the QE and photocatalytic rate are exponentially dependent on temperature at all studied intensities. Furthermore, the data shows that the in the linear regime (100, 200 mW/cm^2) the QE is constant, whereas the QE is significantly enhanced in the superlinear regime (400, 800 mW/cm^2), as compared to the linear regime, at all temperatures. For example, at 398 K the QE in the linear regime (100 and 200 mW/cm^2) is 0.15 % compared to 2.2 % in the superlinear regime (800 mW/cm^2), demonstrating a ~15-fold enhancement in QE. We note that the temperature

dependent, QE data shown in Figure 8.2, was collected from the same catalyst as the data in Figure 8.1 after the catalyst was on stream for 3 weeks. The reported QE's in Figure 8.2(b) are lower than those reported in 1(c) by ~3-7 fold. We attribute this difference to some loss of the cubic nanoparticles shape and some catalyst sintering, which can both decrease the magnitude of the near field plasmon enhancement. Regardless of this minor discrepancy, the data in Figure 8.2 clearly shows an exponential dependence of QE and photocatalytic rate on operating temperature.

The observation of an exponential dependence of the photocatalytic rate (and QE) on operating temperature is a unique feature of photocatalysis on metal surfaces. On semiconductor photocatalysts, temperature only has a small effect on photocatalytic rate, showing a minimal increase in rate at low temperature followed by significantly reduced photocatalytic rates at higher temperatures (>150 C) due to enhanced rates of charge carrier recombination.[24] This unique feature of metallic photocatalysts, provides and

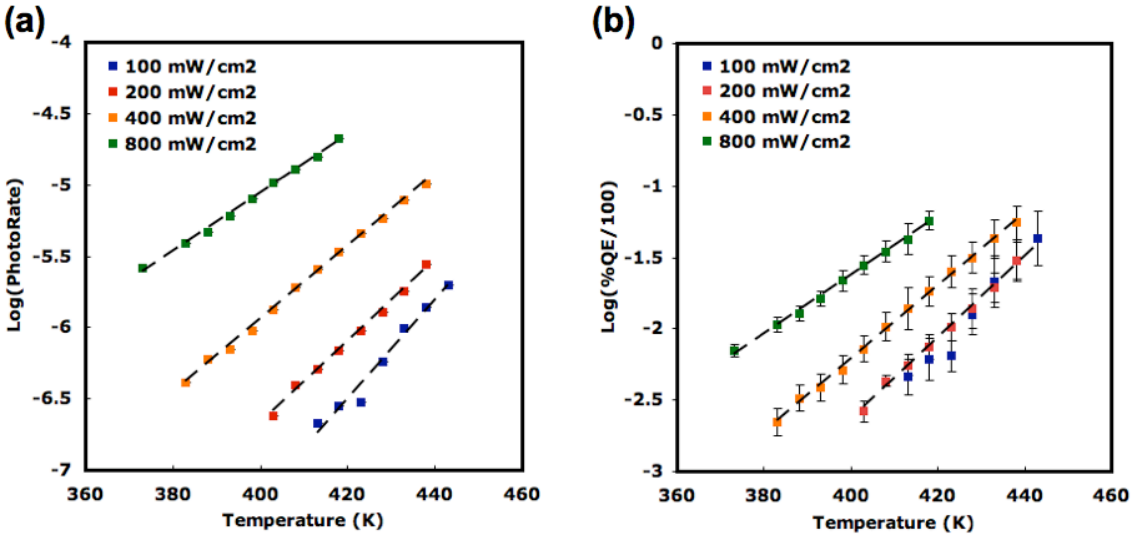

Figure 8.2 The effect of temperature on the photocatalytic rate and QE. (a) This figure shows the Log_{10} of the photocatalytic rate (mol/gcat/s) as a function of intensity. (b) The figure shows the Log_{10} of the quantum efficiency as a function of temperature. The linear dependence in these two plots shows that the photoctalytic rate is exponentially dependent on temperature.

excellent route towards significantly enhancing the photocatalytic efficiency with only small changes in the operating temperature and shows that metallic photocatalysts can couple thermal stimulus with photonic stimulus to drive a catalytic reaction. In the low intensity regime (<300 mW/cm^2) the photocatalytic rate displays a linear dependence of rate on intensity and an exponential dependence of photo-rate on temperature, showing that metallic particles are effectively able to couple thermal energy to assist in a photo-induced electron-driven process. In the higher intensity regime (>300 mW/cm^2) the photocatalytic rate exhibits a stronger dependence on intensity and a weaker dependence on temperature, indicating that the photo-induced multi-electron driven process either less effectively couples to thermal energy or, requires less thermal assistance to execute the catalytic reaction.

In general, Figures 8.1 and 8.2 show the unique ability of plasmonic nanoparticles to efficiently perform photocatalyitc reactions, with low intensity visible light, through a multi-electron driven process that effectively couples with an external thermal stimulus. There are three experimentally observed signatures that support the proposed mechanism, (i) a regime shift from a linear to a super linear dependence of rate (QE) on source intensity, (ii) a dependence of the measured O_2^{16}/O_2^{18} KIE on source intensity, and (iii) an exponential dependence of the photo-rate on the process operating temperature.

8.4.3 Kinetic Analysis

There have been numerous studies that examine multi-electron driven chemical processes on metallic single crystals induced by femtosecond laser excitations.[25,26] In general, the observations all revolve around the concept of a substrate mediated

electronic excitation of the adsorbate, which results in a vibrationally excited molecule upon decay of the excited electron back to the substrate. This is very similar to the mechanism proposed in Chapter 7 for electron driven O_2 dissociation, with one major distinction. In the linear process, the concentration of excited electrons at the Ag surface is fairly low, meaning that when an electron scatters off the O_2 molecule, if an insufficient amount of energy is transferred to the molecule to induce dissociation, the molecule will completely dissipate the gained vibrational energy to the substrate prior to another electron scattering event. In multi-electron driven processes, the concentration of excited electrons at the metal surface is sufficiently high, such that it becomes probable for multiple scattering events to occur in parallel, off the same adsorbed molecule, prior to dissipation of gained energy.

Multi-electron processes driven by femtosecond lasers were recently analyzed utilizing DFT calculations coupled with a well-studied model for the scattering of electrons off resonant adsorbate states to provide an understanding of the origin of the super linear power law phenomenon in photocatalytic processes on metal surfaces.[27] The fundamental concept is very simple; the order of the power law exponent can be related to the activation barrier for a particular elementary step and the energy associated with the vibrational mode that corresponds to the reaction coordinate through the expression, $n_r \approx \frac{E_a}{\hbar\omega}$. In this expression, n_r is the power law order, Ea is the activation barrier for a particular elementary step, and $\hbar\omega$ is the energy associated with the vibrational mode along the reaction coordinate. This relationship was derived theoretically in the paper, and 2 examples are used to compare (a) NO desorption from Pd(111) where n_r ~3.3, $\hbar\omega$ ~210 meV, Ea ~ 1.0 eV and (b) atomic O diffusion on Pt(111) where n_r ~15, $\hbar\omega$

~50 meV, Ea~.8 eV. In general this makes intuitive sense. If a particular vibration has a very steep well ($\hbar\omega$ is higher), the act of electronic excitation will deposit more energy into the vibrational mode. This means that if the ratio of Ea/$\hbar\omega$ is large, a larger number of excitations will be required to significantly affect the rate of this step. This general concept provides a nice framework to understand how electronic excitations can be converted to virbtational energy required to traverse an activation barrier.

Figure 8.3(a) and (b) show kinetic measurements performed for the pure thermal process as well as 4 increasing intensities (100, 200, 400 and 800 mW/cm^2). In these measurements the ethylene conversion was kept very low, <1%, to ensure the rate of the reverse reaction was negligible. This setup allows us to analyze the kinetics of the forward reaction for the conversion of ethylene. We showed convincingly in the previous chapter, based on kinetic isotope experiments, that for 75 nm Ag nanocube catalysts under identical experimental conditions, O_2 dissociation controls the rate of reaction.[13] Because O_2 dissociation significantly controls the rate under our conditions, we can use the results of the kinetic experiments shown in Figure 8.3 to quantify the effect that electron excitations have on the energetics of the O_2 dissociation process. Figure 8.3(b) shows that the pure thermal activation barrier is 81 kJ/mol and that as the source intensity is increased, the activation barrier significantly decreases. Although these experiments were carried out over a temperature regime of about 100 K (lower temperature was used for higher intensity) the magnitude of the thermal activation barrier is expected to stay fairly constant over this range. This indicates that changes in the E_a are a direct result of electronic excitations of O_2 molecules. This plot shows that the activation barrier is reduced by ~32 kJ/mol for the measurements at 800 mW/cm^2 source intensity.

These measurements are nicely in-line with the simple relationship $n_r \approx \frac{E_a}{\hbar\omega}$. The original analysis was developed for electron driven process at very low temperatures, where the electrons provide the entire driving force for executing reactions, ie. no thermal energy is provided to the system. We introduce a slightly modified version of this relationship for our combined photo-thermal process, $n_r \approx \frac{\Delta E_a}{\hbar\omega}$, where the decrease in activation barrier (the energy provided by electronic excitation) is related to the power law exponent. Typical reported vibrational energies for O_2 on Ag surfaces call in the range of 650 – 850 cm^{-1}. We will assume a vibrational energy of 800 cm^{-1} or 10 kJ/mol to simplify the analysis. Using the expression, $n_r \approx \frac{\Delta E_a}{\hbar\omega}$, with ΔE_a = 32 kJ/mol and hw = 10 kJ/mol, we would expect a power law exponent of n_r =3.2, at 800 mW/cm^2. This is in

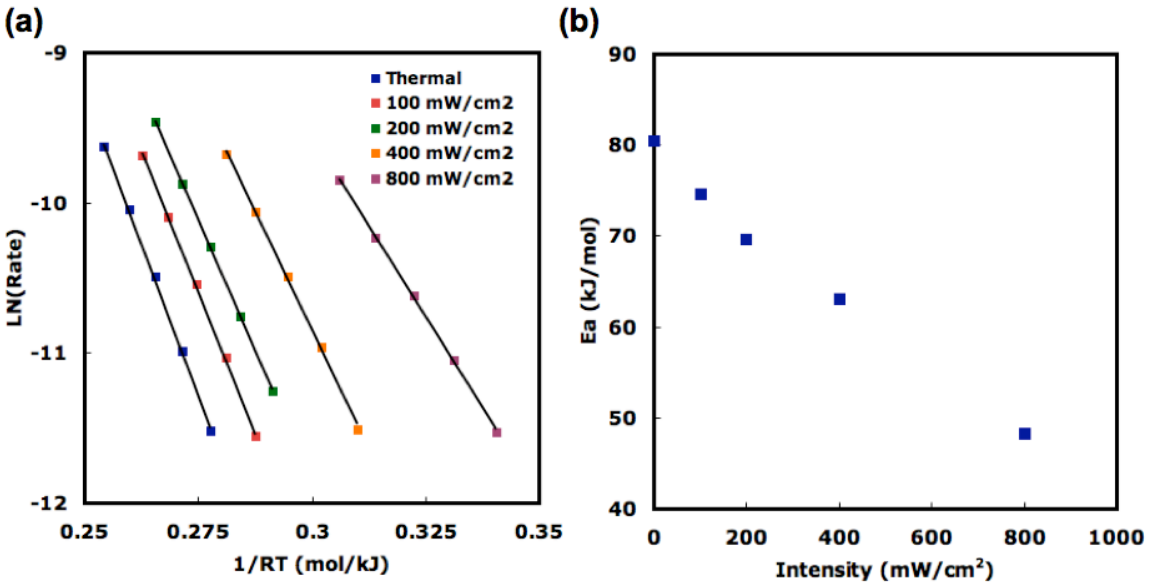

Figure 8.3 Photothermal reaction kinetics. (a) This figure shows an Arrhenius plot for ethylene epoxidation for the pure thermal process and the photothermal process (with various source intensities). Rate in mol/gcat/s. (b) The figure shows the slope of the Arrhenius plot, the activation barrier, as a function of source intensity.

excellent agreement with the measurements in Figure 8.1(b). At 800 mW/cm^2 and 398 K (almost identical to the temperature used in the kinetic experiments), the power law exponent is measured as, $n_r = 3.5$. This analysis shows that our data very nicely follows the recently developed relationship for multi-electron driven process on metal surfaces, and shows that the reduction in activation barrier is likely due to a multi-electron driven activation of O_2 resulting in a significant energy transfer from excited plasmons into the reaction coordinate for O_2 dissociation.

8.4.4 Non-linear Process Effect on Selectivity

In the previous sections, the effect of the regime shift on the rate, QE, KIE and E_a were discussed. We have also performed measurements analyzing the effect that the multi-electron process has on EO selectivity. In Chapter 7 it was shown that in the linear regime the selectivity in the photothermal process was identical to the pure thermal process as a function of the reaction rate. Figure 8.4(a) and (d) show the selectivity to EO for the pure thermal process and for the photothermal process at 4 source intensities (100, 200, 400 and 800 mW/cm^2). Figure 8.4(a) shows that in the linear regime, I=100, 200 mW/cm^2) the selectivity is identical to the measured selectivity in the thermal process as a function of rate; this is in agreement with the data shown in Chapter 7. As the process enters the multi-electron regime (I = 400, 800 mW/cm^2) the selectivity to EO decreases at a given rate. These results indicate that in the linear regime the presence of energetic electrons on the Ag surface has very little, or no, effect on the energetics of elementary steps involved in the selectivity controlling steps. However, the results in Figure 8.4 suggest that the high concentration of energetic electrons present in the super-

linear regime begin to affect the energetics of the elementary steps that control the process selectivity, ie. the isomerization of the oxametallacyle (OMC) to form ethylene oxide and acetaldehyde.[28]

The reduced selectivity indicates that energetic electrons are interacting with the OMC to change selectivity. Furthermore this effect becomes stronger in the nonlinear regime, indicating that multiple electronic excitations of the OMC are occurring. The change in the energetics associated required to induce changes in selectivity (<10 %) is much smaller than the change in the energetics associated with the activity, ie. a change in the energy associated with the branching ratio of the OMC to EO and acetaldehyde of only 0.01 eV has a significant affect on selectivity, where as in section 8.4.3 our analysis shows that the E_a of the rate controlling step is changing by 0.1-0.3 eV depending on intensity. From our previous work on Ag(100) (chapter 4), we have deduced that a decrease in selectivity could be associated

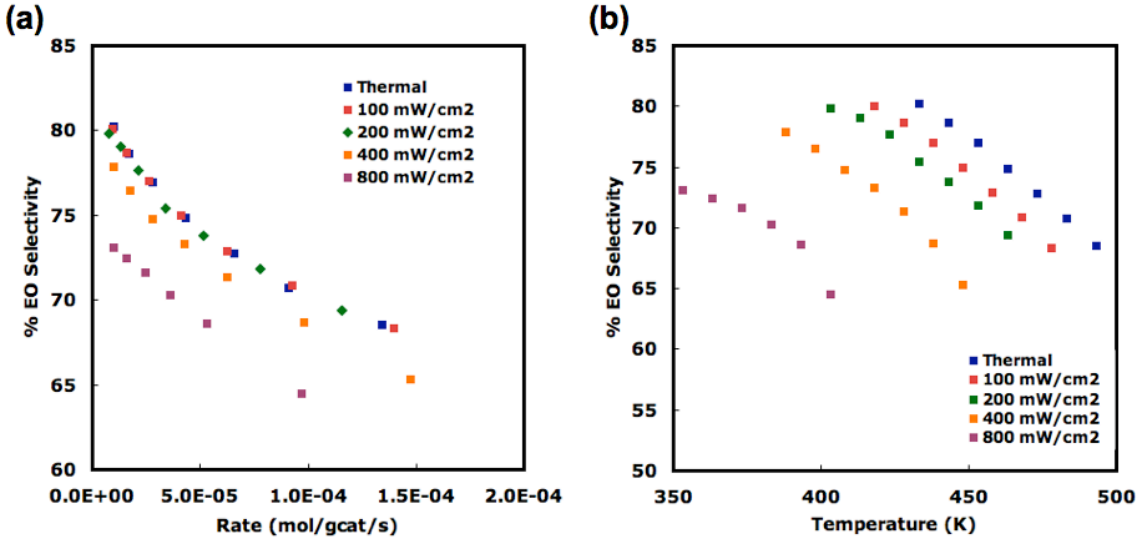

Figure 8.4 The effect of the multi-electron process on EO selectivity. (a) This figure shows the measured EO selectivity as a function of rate, for the pure thermal and photothermal processes. (b) The figure shows the EO selectivity plotted as a function of the operating temperature.

with a larger decrease in the O-Ag binding energy as compared to the C-Ag binding energy in the OMC. This suggests that there may be a larger amount of energy being deposited into the Ag-O bond as compared to the Ag-C bond in the OMC, thereby reducing the selectivity of the process.[17,29] We note that an additional effect could be occurring, whereby a new unselective reaction pathway not associated with the OMC is becoming energetically feasible due to the energetic electron mechanism, and that this is resulting in the reduced selectivity. In-depth analysis of these effects is proposed in the future research section in Chapter 9.

8.5 Theoretical Results

8.5.1 Model Details

To further explore the proposed mechanism of the electron driven photo-thermal-catalytic process on a molecular level, we have employed an electron scattering model that calculates the probability that an electron scattering off an adsorbate anti-bonding orbital will result in a reaction.[14,16] In the electron scattering model, the adsorbate/substrate system is described by a Newns-Anderson-type Hamiltonian with linear coupling of unoccupied resonant electronic state and the vibrational states of the adsorbate. The effect of operating temperature was included by using Bose-Einstein statistics to define the temperature dependent initial distribution of vibrational states $q_{vib}(T)$ in the adsorbate as shown in Equation 1.

$$q_{vib}^{n}(T) = \frac{1}{e^{\beta(n+\frac{1}{2})h\nu} - 1} \qquad (1)$$

When the resonant electronic state becomes transiently occupied, due to electron scattering, the adsorbate jumps from the neutral potential energy surface onto the excited state potential energy surface. DFT calculations were used to obtain neutral potential energy surfaces, and ΔSCF-DFT calculations were used to calculate the excited state potential energy surface.

The driving force for nuclear motion of an adsorbate, due to resonance electron scattering, is characterized by the coupling constant obtained from the slope of the excited state PES at the equilibrium position and the vibrational frequency along the reaction coordinate, which is obtained from the ground state PES. After the adsorbate spends a short time, τ, on the excited state surface, the molecule returns to the ground

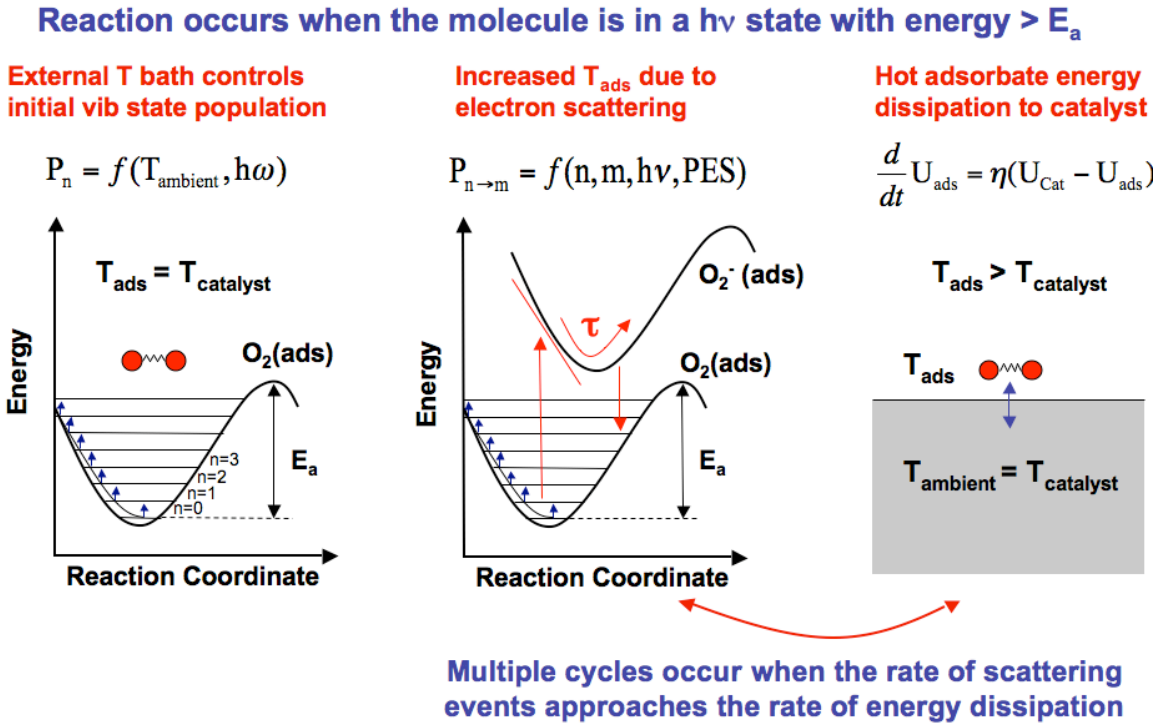

Figure 8.5 Schematic of the modeling approach. In the first step the initial temperature dependent distribution of populated vibrational states is calculated using the Bose-Einstein distribution. In the second step the energy gain from an electron excitation is calculated. The probability function is dependent upon the E_a, the vibrational energy of the bond and the slope of the excited state PES. In the last step, the vibrationally excited molecule either reacts, or dissipates energy to the substrate. The last two steps are repeated until the adsorbate temperature reaches equilibrium.

state PES. If the molecule has gained sufficient energy to overcome the activation barrier, the reaction occurs. If the molecule has not gained sufficient energy to react, the molecule begins to dissipate the gained energy into the substrate. A friction-based model as shown in Equation 2, was established to describe the energy dissipation from n^{th} vibrationally excited states (characterized by adsorbate temperature T_{ads}) to the substrate thermal bath T_{sub} , where η is the friction coefficient.

$$\frac{dT_{ads}^{n}}{dt} = \eta(T_{ads}^{n} - T_{sub}) \qquad (2)$$

The value of friction coefficient η^{-1} is estimated to 1~10 ps previously,[30] but we treat this as an unknown parameter and define a parameter, F, that is a functional of the friction coefficient and is inversely proportional to the time, Δt, between successive electron scattering events, Equation 3. A value of F=1 is approximately 10^{11} electrons/site/second.

$$\Delta t = \frac{1}{F[\eta]} \qquad (3)$$

In the electron scattering process, each incoming energetic electron will change the distribution of the adsorbate vibrational state until equilibrium is established between decay and excitation. These two processes give a sequence of excitation and deexcitation events of vibrational states, which deposits energy into the adsorbate internal degree of freedom, eventually activating the bond. The rate of the whole process is obtained by assuming that the molecule with higher energy than thermal activation barrier will react. Figure 8.5 shows a schematic of the simulations.

The parameters used to describe the adsorbate/substrate system in this model were all calculated from first principles. The activation barrier, E_a, for O_2 dissociation on Ag(100) was calculated through the nudged-elastic band formalism to be 1.17 eV. The

width of the $2\pi^*$ was estimated to be 1.3 eV, based on analysis of the density of states. The energy of excited electrons was calculated to be distribution of the plasmon intensity. This function was defined in chapter 7 as the overlap of the UV-vis spectra of the Ag nanoparticle catalyst, and the wavelength dependent source intensity. Resonance energy, the energy required to populate the $2\pi^*$ orbital, was calculated to be 2.4 eV, see Chapter 7. The vibrational frequency of O_2 on Ag(100) was calculated from the ground state potential energy surface and the harmonic oscillator approximation to be 0.102 eV. These values gave a coupling constant of, -0.047 eV. For model details see reference 16.

8.5.2 Model Results and Comparison to Experiment

We employed the model to study the effect of operating temperature and source intensity on the O_2 dissociation process on the Ag(100) surface. We focus on the O_2 dissociation process because this step controls the rate of ethylene epoxidation on Ag nanocube catalysts (see the discussion above and in the previous chapter). Figure 8.6(a) shows the calculated rate for the electron scattering process to induce O_2 dissociation as a function of flux (electron-adsorbate scattering events/site/ps). This plot is analogous to the experimental results shown in Figure 8.1(a). Figures 8.6(b) and (c) show the power law exponent, 8.6(b), and the reaction probability (which is analogous to experimentally measured quantum efficiency.), 8.6(c). These figures are simulated results of the experimental data in Figures 8.1(b) and (c). We have calibrated the flux used in the simulations to the experimentally used source intensity, by lining up the location of the beginning of the regime shift. Figure 8.6(b) shows that the experimentally measured and simulated dependence of the power law exponent on source intensity are very similar,

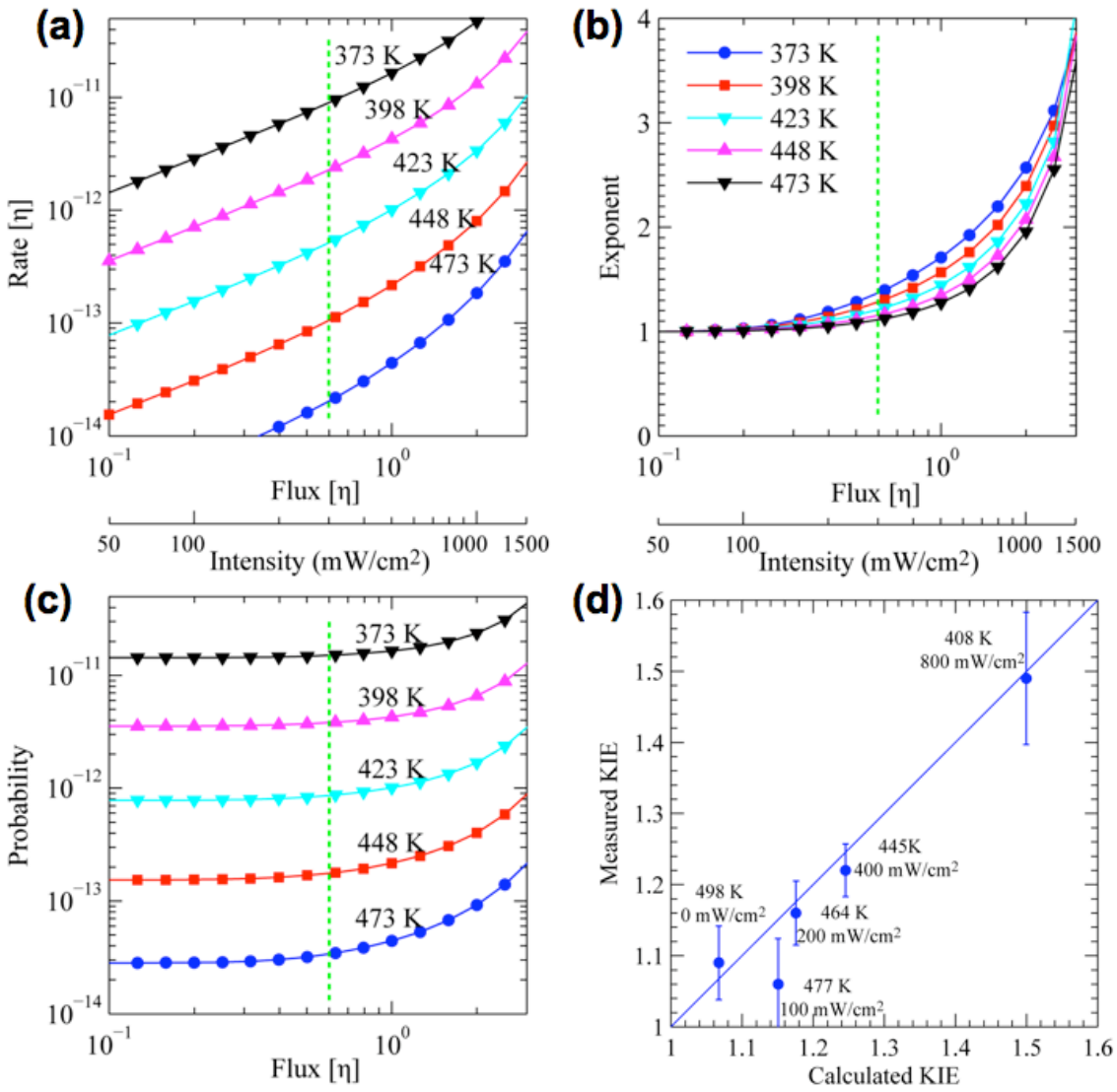

Figure 8.6 Simulated regime shift from single to multi-electron process. (a) This figure shows the simulated rate of O_2 dissociation as a function of the defined variable, Flux. The vertical green line indicates the onset of the regime transition. (b) The measured exponent from Figure 8.6(a) as a function of Flux. (c) The reaction probability, (rate divided by the flux) as a function of flux. (d) This figure shows a parity plot of the experimentally measured and simulated KIE.

both reaching about n=3.5 at the highest intensity used in the experiments. Figures 8.6(a) (c) show that the model is able to capture the transition from a linear to a super linear dependence of rate on flux.

In addition to the models ability to capture the regime transition, we have also examined the effect of isotopic labeling in the simulations. This was done by decreasing the energy of the vibrational mode of O_2, to match the vibrational frequency of the isotopically labeled molecule. This shift in vibrational modes is well-known to be proportional to the square root of the mass ratio. Figure 8.6(d) shows a parity plot of the experimentally measured and simulated KIE. The plot shows that there is an excellent agreement between the experimentally measured and the simulated KIE.

The ability of the model to capture the experimentally observed regime transition from a linear to superlinear process and the enhanced KIE, allows us to explore the underlying physics controlling the regime shift in the electron driven process. In the linear regime, if the electron scattering deposits enough energy into the potential energy surface the molecule will quickly dissociate. If the amount of energy deposited is insufficient to overcome the activation barrier, the adsorbate dissipates the excited vibrational energy into the catalyst surface, returning to the initial thermal vibrational distribution, prior to a subsequent scattering event. The transition to the superlinear regime occurs when the frequency between scattering events becomes sufficiently high, such that the probability for multiple scattering events off the same adsorbate, prior to dissipation of vibrationally excited adsorbates to the catalyst surface, becomes substantial. By allowing multiple scattering events from the same adsorbate and having energy from each event be retained in the molecule, the probability of gaining the

sufficient energy to overcome E_a increases.

In addition to the ability of the model to capture the regime transition and KIE, Figure 8.7(a) shows the simulations can also accurately capture the effect of temperature showed in the measured data in Figure 8.2. The intensities were calibrated matching the measured and simulated exponents. Figure 8.7(a) shows that the model predicts

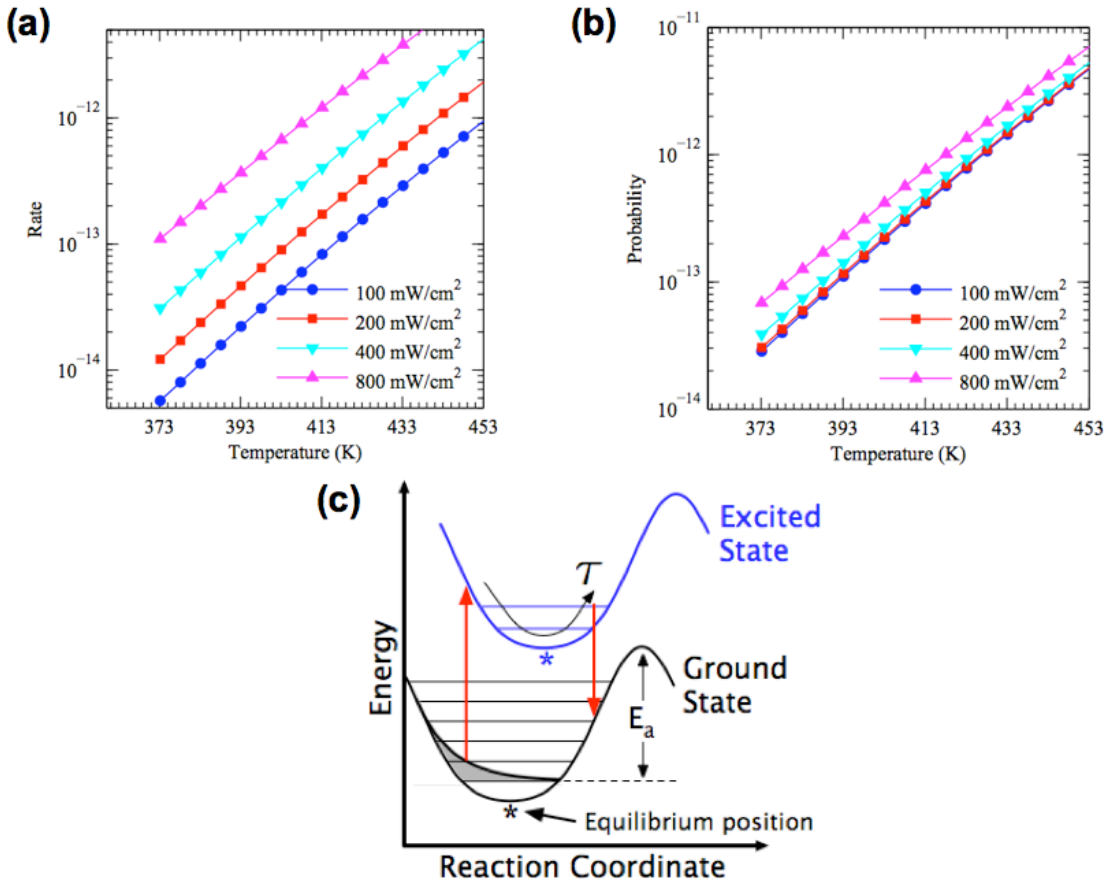

Figure 8.7 Simulated effect of temperature on photocatalyitc rate. (a) The figure shows the rate as a function of operating temperature for 4 different intensities. (b) The figure shows the reaction probability (QE) as a function of operating temperature. (c) The figure shows a schamatic of the effect of temperature. The shading represents the population of vibrational states. As the temperature increases the average vibrational energy of the molecule increases, resulting in a reduced energy input required to drive molecules over E_a, and an increased probability of excitation.

an exponential dependence of the photocatalytic rate on the operating temperature for all intensities. The figure shows that the model qualitatively captures the decreasing effect of temperature in the super linear regime and overall predicts enhancements that are similar to the experimentally measured results. The model predicts a rate enhancement of about 50 fold in the linear regime (I=100, 200 mW/cm^2) which is very close to the measured rate enhancement in Figure 8.1(a). The agreement between the simulated and experimental results show that the model can accurately capture the effect that temperature has on the photo-induced O_2 dissociation rate.

The underlying mechanisms governing the effect of the operating temperature on the photocatalytic rate are proposed to be[16]: (i) a decrease in the required energy gain (due to the electron scattering process) to overcome the activation barrier and (ii) an increased probability of significant energy gain when the adsorbate initially resides in a higher vibrational state, see Figure 8.7(c). Basically, at higher temperatures the relative population of vibrationally excited states exponentially increases, meaning that probability of electron scattering events from highly vibrationally excited states (vibrational states with energies similar to the dissociation activation barrier) also exponentially increases. In addition because most molecules start in high vibrational states, less energy gain is required to drive the molecule over the activation barrier. The result is, at higher temperature the average energy gain from the scattering process increases and the required energy gain to induce dissociation decreases, thus making the electron driven process significantly more efficient.

8.6 Discussion

There are a number of observations from the experimental and theoretical results in this chapter that exemplify how unique plasmonic nanostructures are for driving photocatalytic reactions. The first very unique feature of plasmonic metallic nanostructures that separates these from any other class of materials and allows them to achieve relatively high photo-catalytic reaction rates, is that they effectively couple the light-harvesting and catalytic function in one material. In contrast, due to the lack of electron density at the Fermi level,[31,32,33] materials that absorb UV-vis light, such as semiconductors, generally exhibit poor chemical and catalytic activity. The ability of plasmonic nanostructures to couple thermal and photonic stimuli to drive chemical reactions stems from the potential energy landscapes that are created when adsorbates interact with metal surfaces. Because metallic surfaces are inherently good catalysts the activation barriers associated with many surface reactions are fairly small, ~ 1 eV. This means that at fairly low temperatures (a few hundred degrees C) there is significant population of high-energy vibrational states that are on the order of E_a. As a result of this, the energy gain required from a photo-induced electron scattering event to induce a reaction is reduced as the thermal population of vibrational states increases. In contrast, semiconductor surfaces are fairly poor catalysts, with much higher activation barriers for catalytic reaction. This means that even as the temperature is raised, and the population of higher energy vibrational states of adsorbates occurs, the energy of these states is still negligible compared to the size of the activation barrier. As a result the photo-induced electron processes have to provide a majority of the energy to drive the reaction. It is this combination of strong interactions with UV and visible photons, coupled with excellent

thermocatalytic properties, that make plasmonic nanostructures unique and potentially very useful photo-catalytic materials.

Another important and unique feature that separates plasmonic nanosrtcutrues from other metallic structures is the large enhancement in near-field intensity that occurs due to plasmon excitation.[11] Typically on extended metal surfaces (including those of noble metals) light is not concentrated at the metal surface, and because of this these materials are very poor photocatalysts. On the other hand, as discussed in chapter 3, plasmon excitation acts to effectively store the energy of a photon-flux in very intense fields at the nanoparticle surface. Furthermore the intensity of this field enhancement is the strongest when there are interacting nanoparticles, as is present in the catalytic systems used in this chapter. It was shown in chapter 3, that at the intersection of two 80 nm nanocubes (very similar to the catalytic materials used in this chapter) the average field enhancement is 3-4 orders of magnitudes with areas of much higher field enhancements, ~6 orders of magnitude.[34] This extreme light concentration is crucial for allowing metallic surfaces to efficiently drive photocatalytic reactions. It was discussed above that the only previous observation of a regime shift from a single to multi-electron process on a metal surface, occurred at 9 orders of magnitude higher source intensity. This massive difference in intensity scales can be partially explained, due to the huge enhancements in near-field intensity. The simple comparison shows how crucial the near-field enhancements are in allowing efficient photocatalysis to occur on metal surfaces with low intensity sources. Basically the near-field enhancement acts to concentrate the energy of the photon flux at the surface of the nanoparticle, thereby creating extremely high concentrations of excited electrons that would only be present on

extended metal surfaces at much higher source intensity.

Lastly, it is important to discuss the nature of the electron transfer from plasmon states to the adsorbates. For photocatalytic process on extended metal surfaces, the metal initially absorbs photons. Then excited electrons begin scattering off each other in a time scale of about 5-10 fs. After a few hundred fs, the electrons have "thermalized" and the resulting energy distribution of the electrons is a high energy Fermi-dirac distribution above the Fermi-level.[9] In this picture, only those electrons with resonant energy to the adsorbate state can drive a photocatalytic process, see Figure 8.8(a). In this process a significant amount of the initial photon flux energy is non-elastically transformed into heat in the metal surface. On the other hand, it has been proposed that excited electrons

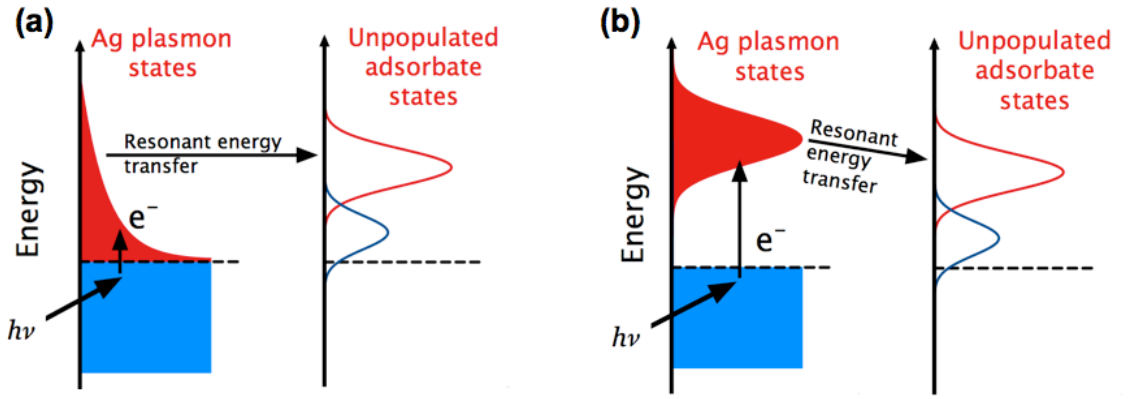

Figure 8.8 Resonant vs. thermalized electron transfer. (a) This figure depicts a schematic of the transfer of thermalized electrons from a Fermi-dirac distribution to the resonant adsorbate state. (b) This figure shows the energey transfer from resonant plasmon states to the resonant unpopulated adsorbate states.

involved in coherently oscillating plasmons, can directly interact with adsorbed molecules through a process termed chemical interface damping.[9] In this process the resonant plasmons directly interact with resonant adsorbate states, thereby providing a much more efficient channeling of the incoming photon flux into molecular bonds, Figure 8.8(b). The difference in efficiency of these two processes for photocatalytic O_2 dissociation on Ag is estimated to be 2-3 orders of magnitude, simply based on the concentration of electrons at energies resonant to the adsorbate state as a function of source intensity. This additional 2-3 orders of magnitude enhancement, coupled with the large field enhancements on plasmonic surfaces, can fully account for the difference in intensity require to induce a multi-electron process on a plasmonic nanoparticle, compared to an extended metal surface.

8.7 Conclusions and Outlook

In this chapter we have shown the first observation of a transition from a single electron, to multi-electron photocatalytic process driven on a metal surface with low intensity continuous wave photons. In addition we have shown that plasmonic nanoparticles can effectively couple thermal and photonic stimuli to driven photocatalytic reactions. As a result of these unique features we observed extremely high rates and quantum efficiencies associated with photocatalytic production of ethylene oxide over Ag nanostructures. A first principles based approach was used to model the process, and allowed us to develop a molecular level model for the photocatalyitc process. These results showed that plasmonic nanostructures are truly unique in their ability to combine

strong interaction with light and good thermocatalytic properties in a single material. The result is a highly efficient photocatalyst.

A major consequence of these findings is the possibilities associated with using metallic structures to efficiently produce important chemicals using solar energy. Currently almost all photocatalytic materials are semiconductors, which are inherently poor catalytic materials. Because of this, the phase-space of possible reactions that can be driven with solar energy is minimal. The findings in this chapter and the previous chapter show that plasmonic nanostructures represent a novel class of photocatyalytic materials for efficient conversion of solar to chemical energy.

8.8 References

[1] M.R. Hoffman, S.T. Martin, W. Choi, D.W. Bahnemann, *Chem. Rev.*, 95, 69-96, 1995.

[2] A.L. Linsebiger, G. Lu, J.T. Yates, *Chem. Rev.,* **95**, 735, 1995.

[3] R. Asahi, T. Morikawa, T.Ohwaki, K. Aoki, Y. Taga, Science, **293**, 269, 2001.

[4] G.K. Mor, *Sol. Energy Matrl. Sol. Cell,* **90**, 2011, 2006.

[5] A. Fujishima, X. Zhang, D.A. Tyrk, *Surf. Sci. Reports,* **63**, 515, 2008.

[6] P. Christopher, D. B. Ingram, S. Linic, *J. Phys. Chem. C*, **114**, 9173, 2010.

[7] H. Awazu, *et. al., J. Am. Chem. Soc.,***130**, 1676, 2008.

[8] D.B. Ingram, S. Linic, *J. Am. Chem. Soc.,* **133**, 5202, 2011.

[9] K. Watanabe, D. Menzel, N. Nilius, H.-J. Freund, *Chem. Rev.*, **106**, 4301, 2006.

[10] W. Ho, *J. Phys. Chem.,* **100**, 13050, 1996.

[11] L. Brus, *Acc. Chem. Res.,* **41**, 1742, 2008.

[12] P.K. Jain, X. Huang, I.H. El-Sayed, M.A. El-Sayed, *Acc. Chem. Res.***, 41**, 1578, 2008.

[13] P. Christopher, H. Xin, S. Linic, *Nature Chem.,* **3**, 467, 2011.

[14] J.J. Mortensen, L.B. Hansen, K.W. Jacobsen, *Phys. Rev. B,* **71**, 035109, 2005.

[15] J. Gavnholt, T. Olsen, M. Engelund, J. Shiøtz, *Phys. Rev. B*, **78**, 075441, 2008.

[16] T. Olsen, J. Gavnholt, J. Schiøtz, *Phys. Rev. B,* **79**, 035403, 2009.

[17] P. Christopher, S. Linic, *J. Am. Chem. Soc.,* **130**, 11264, 2008.

[18] P. Christopher, S. Linic, *ChemCatChem,* **2**, 78, 2010.

[19] D.G. Bausch, W. Ho, *Phys. Rev. Lett.,* **77**, 1338, 1996.

[20] S.R. Hatch, X.-Y. Zhu, J.M. White, A. Campion, *J. Phys. Chem.,* **95**, 1759, 1991.

[21] S.K. So, R. Franchy, W. Ho, *J. Chem. Phys.,* **95**, 1385, 1991.

[22] M. Bonn, *et al., Science*, **285**, 1042, 1999.

[23] D.N. Denzler, C. Frischkorn, C. Hess, M. Wolf, G. Ertl, *Phys. Rev. Lett.*, **91**, 226102, 2003.

[24] T.A. Westrich, K.A. Dahlberg, M. Kaviany, J.W. Schwank, J. W. *J. Phys. Chem. C*, DOI: 10.1021/jp204405h, 2011.

[25] S.A. Buntin, L.J. Richter, R.R. Cavanagh, D.S. King, *Phys. Rev. Lett.,* **61,** 1321, 1988.

[26] *Laser Spectroscopy and Photochemistry on Metal Surfaces;* Dai, H.-L., Ho, W., Eds.; World Scientific: Singapore, 1995.

[27] T. Olsen, J. Schiotz, *Phys. Rev. Lett.,* **130**, 238301, 2009.

[28] S. Linic, M. A. Barteau, *J. Am. Chem. Soc., **125***, 4034, 2003.

[29] A. Kokalj, P. Gava, S. Gironcoli, S. Baroni, *J. Catal.,* **254**, 304, 2008.

[30] S. Funk, *et. al., J. Chem. Phys.*, **112**, 9888, 2000.

[31] B. Hammer, J.K. Nørskov, *Nature*, **376**, 238, 1995.

[32] E. Nikolla, J. Schwank, S. Linic, *J. Am. Chem. Soc.* **131**, 2747, 2009.

[33] H. Xin, S. Linic, *J. Chem. Phys.* **132**, 221101, 2010.

[34] J.A. Schuller, *et. al., Nature. Mat.*, **9**, 193, 2010.

Chapter 9

Conclusions and Future Outlook

9.1 Summary

This dissertation combines theoretical and experimental techniques to design efficient catalytic and photocatalytic materials. Quantum chemical calculations were used to guide the synthesis of well-defined Ag nanoparticles with controlled shapes and sizes, used as highly selective catalysts in the ethylene epoxidation reaction. In addition, we showed that the unique optical properties of Ag nanoparticles could be exploited to design novel photocatalytic materials. It was demonstrated for the first time that metallic nanoparticles could act as highly efficient photocatalysts. In this chapter we summarize the main conclusions and ramifications of the research presented in this dissertation and outline future research directions.

9.2 General Conclusions

In this dissertation we have used a multi-faceted approach, combining quantum chemical calculations, well-controlled synthesis techniques and an arsenal of characterization techniques to design catalytic materials for important catalytic and photocatalytic oxidation reactions. Specific focus was placed on exploiting unique shape and size dependent properties of Ag nanoparticles to design new catalytic materials and entirely new catalytic reacting systems (combining both thermal and photonic stimuli) for the industrially relevant ethylene epoxidation reaction. We demonstrated novel routes for both enhancing the selectivity and activity of Ag based epoxidation catalysts. The major conclusions of this dissertation are:

- We utilized density functional theory (DFT) calculations to examine the effect of Ag surface structure on ethylene epoxidation selectivity. Based on these calculations, we identified the Ag(100) surface facet as being inherently more selective than the Ag(111) surface facet, which dominates most industrial Ag catalysts synthesized using classical approaches. We used synthesis approaches recently developed in the nanotechnology community to synthesize Ag nanowires dominated by the Ag(100) facet. The results of the DFT calculations were supported by reactor studies that showed Ag nanowires, dominated by the (100) surface facet, were significantly more selective for ethylene epoxidation compared to an Ag catalyst dominated by the (111) facet.
- Well-controlled synthesis of Ag nanoparticles of different shapes and sizes was used to show that ethylene epoxidation selectivity is highly dependent on

geometric structure of catalytic particles. We found that large Ag nanoparticles with high concentrations of Ag(100) surface facets and low concentrations of undercoordinated sites achieve the highest selectivity. These mechanistic insights were used to design a highly selective catalyst for the ethylene epoxidation reaction, that rivaled heavily promoted industrial catalytic materials developed through conventional "trail-and-error" approaches.

- We show that composite materials composed of plasmonic Ag nanostructures and TiO_2 photo-catalysts show enhanced photo-activity compared to the pure TiO_2 in the oxidative decomposition of dye molecules. The enhanced photo-catalytic activity is attributed to radiative transfer of energy, mediated by surface plasmons, from Ag particles to the semiconductor leading to higher concentrations of charge carriers (e-/h+ pairs) in the semiconductor and therefore to higher photo-catalytic activity. By rationally changing size and shape of Ag nanostructures it is possible to maximize photo-catalytic activity of a semiconductor at a given excitation wavelength.
- We demonstrate that plasmonic Ag nanostructures can directly act as photocatalysts for a number of important catalytic oxidation (ethylene epoxidation, CO oxidation and selective NH_3 oxidation) reactions, under low intensity visible light illumination. Based on source intensity dependent measurements, kinetic isotope experiments and DFT calculations, we postulate that excited plasmons on the Ag surface act to populate O_2 anti-bonding orbitals, forming a transient negative ion state, thereby facilitating the

rate-limiting O_2 dissociation reaction in a first order electron driven process. This photocatalytic activity allows a reduction in the operating temperature for ethylene epoxidation of up to 40 ^{0}C, when using a photon source with the intensity of 2-3 suns, while maintaining identical ethylene oxide production rate.

- We also show that the excitation of surface plasmons on Ag nanostructures under ethylene epoxidation conditions, by visible photon illumination with intensity > 300 mW/cm^2 (about 3 suns), results in a highly efficient multi-electron driven photocatalytic process. This shows the first observation of a regime shift from linear to non-linear dependence of photo-rate on intensity, driven by a low intensity continuous wave source. In addition, the excellent thermo-catalytic features of metallic nanoparticles allow for an effective coupling of thermal and photonic stimuli to produce a previously unreported exponential dependence of photocatalytic quantum efficiency on operating temperature. We provide a first-principles based model, which captures the effect of intensity and temperature on the process efficiency.

The work presented in this dissertation provides two unique platforms for controlling and engineering the catalytic function of metallic nanoparticles. The first example shows that the combination of DFT calculations and well-defined solution based synthesis approaches may provide a critical platform for the design of highly selective catalytic materials. In addition it was shown that by combining these two approaches, mechanistic insights could be garnered that allowed the development of molecular scale models describing the function of catalytic materials. In the second example, it was

discovered that plasmonic Ag nanostructures could effectively couple thermal and solar energy to efficiently drive reactions at significantly lower temperature than a pure thermal process. This discovery opens the door to the design of a new class of photocatalytic materials, based on metallic nanoparticles, for the selective production of important chemicals using solar energy.

9.3 Outlook on Future Research

The focus of this dissertation was to design new heteroegenous (photo)catalytic materials for important oxidation reactions. In addition to the design of materials, we attempted to develop new approaches for the manipulation of catalytic chemistry on metal surfaces. There are a number of nature extensions from this work. In Chapters 4 and 5 we outlined an approach towards the design of Ag nanoparticles with targeted geometric features. One major downfall of this approach is that the structures we synthesized are not the most thermodynamically stable structures of Ag, meaning that over time the shape and size may significantly change, thereby diminishing catalytic performance. It is crucial that approaches are developed to stabilize nanoparticles with targeted shape and size, against thermal degradation. Recently a few approaches have emerged, such as encapsulation of metal particles in SiO_2 shells, and selectively poisoning the particles with other metals or contaminants.[1,2,3] These approaches have only recently been developed and further optimization and testing is needed. In addition, the application of the general approach used in Chapters 4 and 5 (DFT calculations combined with advanced synthesis techniques) to the design of catalysts for other important reactions is another obvious extension. For example, the design of cheap, non-

platinum based catalysts for the electro-catalytic oxygen reduction reaction, maybe possible using the controlled synthesis of different shapes and sizes of Ag nanoparticles.

In addition to the design of thermocatalytic materials, in Chapter 6 we demonstrated that the addition of plasmonic Ag nanoparticles to a TiO_2 matrix can significantly enhanced the photocatalytic activity. These results have already been extended to design composite photocatalysts for visible light driven water splitting over composite plasmonic/semiconductor photocatalysts.[4] The natural extension to this work now becomes the design and synthesis of composite materials with engineered geometric structures to optimize the interaction between the building block materials. This will require in depth theoretical analysis and the development of scalable synthesis approaches for patterned 3-D composite structures.

In Chapters 7 and 8 we showed how plasmoinc nanoparticles could be directly used as efficient photocatalysts for a number of important oxidation reactions. We only showed this effect for Ag, which is a unique catalyst for direct epoxidation reactions, but is not used widely in industry for other reactions. An interesting extension of these findings would be the development of bimetallic catalytic materials that combine the plasmonic function of Ag, with the catalytic function of another important metal (Pt or Pd for example), to drive photocatalysis on other metal surfaces. In addition, we postulated in Chapter 8 that strong near field enhancement of an incoming photo flux is crucial for driving efficient photocatalysis on metals. A detailed analysis of this hypothesis is needed to prove the importance of this effect. One possible route to achieve this is by controlling the interparticle distance, thereby manipulating the field strength, on a series of plasmonic catalysts and measuring the relative rate enhancements. Lastly and perhaps

most interestingly, the mechanism we proposed for the plasmon driven photocatalysis on Ag suggests that it may be possible to selectively active targeted chemical pathways by manipulating the energy of excited plasmons to match that of targeted adsorbate resonance states. Further mechanistic studies and proof-of-concept experimental studies could be carried to show whether or not plasmonic metal particles can be rationally tuned to enhance the selectivity as well as the activity through the use of solar energy.

9.4 References

[1] S. H. Joo, J. Y. Park, C. K. Tsung, Y. Yamada, P. Yang, G. A. Somorjai, *Nat. Mater.*, **8**, 126, 2009.

[2] D. Aherne, D. E. Charles, M. E. Brennan-Fournet, J. M. Kelly, Y. K. Gun'ko, *Langmuir*, **25**, 10165, 2009.

[3] J. Zeng, J. Tao, D. Su, Y. Zhu, D. Qin, Y. Xia, *NanoLett.,* **11**, 3010, 2011.

[4] D.B. Ingram, S. Linic, *J. Am. Chem. Soc.,* **133**, 5202, 2011.